

# Topological interactions of two-dimensional non-Abelian quantum vortices in spinor Bose–Einstein condensates

Thomas G. Mawson  
BScAdv(Hon)

Academic Advisors:  
Assoc. Prof. Tapio Simula  
Dr. Timothy Petersen



A thesis submitted for the degree of  
**Doctor of Philosophy**  
at Monash University in 2019  
School of Physics and Astronomy

© Thomas G. Mawson, 2019

# Abstract

Non-Abelian topological excitations can be created under the breaking of certain discrete symmetries. These excitations are characterised by non-trivial topological interactions, which can be realised upon collision or braiding of any two such excitations. In this thesis we use numerical experiments, based on the Gross–Pitaevskii equation, to study these fundamental topological interactions for non-Abelian vortices in a two-dimensional spin-2 Bose–Einstein condensate, and demonstrate novel applications to topological quantum information processing and storage, as well as quantum turbulence.

To understand the fundamental properties of the topological interactions, we study the collision dynamics of vortex pairs of both Abelian and non-Abelian kind. In contrast to Abelian vortex pairs, which annihilate or pass through each other, we observe non-Abelian vortex pairs to undergo rungihilation, an event that converts the colliding vortices into a rung vortex.

We observe that the braiding and collision dynamics of non-Abelian vortices provide the essential characteristics of non-Abelian anyons. The non-Abelian vortex anyon models, based on the quantum double construction, are characterised by mapping the vortices to particle-like excitations called fluxons and introducing additional  $H$ -charges. To demonstrate the actions required to perform single- and two-qubit unitary operations, a toy model of a topological qubit is suitably constructed.

We then move to a study of two-dimensional quantum turbulence. We demonstrate a method based on three-source interference of condensate fragments to deterministically generate lattices of vortices with fractional mass and spin current circulation. By evolving these lattices states, we

show that three-source interference is experimentally viable for realising quantum turbulence in spinor condensates. Finally, we use vortex imprinting to study turbulent states of vortices of either Abelian or non-Abelian kind, and observe potential indicators of a new kind of two-dimensional non-Abelian quantum turbulence.

## Declaration

This thesis is an original work of my research and contains no material which has been accepted for the award of any other degree or diploma at any university or equivalent institution and that, to the best of my knowledge and belief, this thesis contains no material previously published or written by another person, except where due reference is made in the text of the thesis.

Signature:

Name: Thomas G. Mawson

Date: 21/10/19



## Acknowledgements

I am indebted to a number of people without whose advice, support and friendship this PhD would have been all the harder to complete. First and foremost, I'd like to thank my supervisors, Tapio and Tim, for their selfless dedication to being fantastic mentors. Thanks for always being available to discuss research or my career, and for being constant sources of optimism, enthusiasm and new ideas. Mum and Dad, thanks for putting up with my complaining when research was going poorly and my gloating when it was going well. You probably ingested more second hand physics than is strictly healthy. My brother Tim and his partner Liz, thanks for paving the way and passing on your hard won knowledge. Thanks to all my friends Andrew, Vaishali, Shaun, Adelle, Adam, Georgie, Keven and Gwen for being sources of support, both scientific and in life, and for being a healthy distraction from work and unhealthy procrastination. I'd also like to thank my collaborators, whose contributions greatly enhanced my research. Gary, who provided much of the code base which underpins the numerics in this thesis. Joost, for answering all those lingering and perplexing questions regarding the non-Abelian vortex anyons. Thanks also to my Milestone panel advisers; Russ, Peter and Kris, and to the whole BEC group, all of whom provided valuable discussions which helped shape this thesis. Thanks finally to Jean, for her tireless support and advocacy for the entire PhD cohort. This research was supported by an Australian Government Research Training Program (RTP) Scholarship.



# Contents

<b>1. Introduction</b>	<b>1</b>
1.1. List of publications . . . . .	8
<b>2. Theoretical framework</b>	<b>9</b>
2.1. Bose–Einstein condensation . . . . .	9
2.2. Mean field theory of spin-2 Bose–Einstein condensates . . . . .	13
2.3. Superfluid phases and order-parameter manifolds . . . . .	17
2.4. Topological excitations in Bose-Einstein condensates . . . . .	19
2.5. Non-Abelian vortices in the cyclic-tetrahedral phase . . . . .	25
2.6. Vortex collision dynamics . . . . .	29
2.7. Topological influence . . . . .	33
2.8. Non-Abelian anyons . . . . .	34
2.9. Topological quantum computing . . . . .	39
<b>3. Numerical implementation</b>	<b>43</b>
3.1. Gross–Pitaevskii equation for spin-2 Bose–Einstein condensate . . . . .	45
3.2. Preparation of initial states with non-Abelian vortices . . . . .	47
3.3. Detection and identification of vortices . . . . .	49
<b>4. Collision dynamics of two-dimensional non-Abelian vortices in spin-2 Bose–Einstein condensates</b>	<b>55</b>
4.1. Numerical experiments . . . . .	58
4.2. Annihilation and pass through of Abelian vortices . . . . .	58
4.3. Rungihilation of non-Abelian vortices . . . . .	60
4.4. Summary . . . . .	61
<b>5. Braiding and fusing of non-Abelian vortex anyons</b>	<b>63</b>
5.1. Numerical experiments . . . . .	66
5.2. Non-Abelian vortex anyons . . . . .	67
5.3. Non-Abelian vortex anyon models . . . . .	69

5.4. Topological qubit of non-Abelian vortices . . . . .	74
5.5. Implementing two qubit unitary operations . . . . .	77
5.6. Universality . . . . .	79
5.7. Realising quantum superpositions of fluxons . . . . .	80
5.8. Summary . . . . .	81
<b>6. Two-dimensional quantum turbulence in spinor condensates</b>	<b>85</b>
6.1. Quantum turbulence . . . . .	85
6.2. Initiating turbulence from multi-wave interference . . . . .	88
6.3. Collision of three scalar condensates . . . . .	89
6.4. Collision of three spinor condensates . . . . .	92
6.5. Numerical experiments . . . . .	94
6.6. Vortex lattices from three-source interference in a spin-2 Bose–Einstein condensate . . . . .	95
6.7. Towards two-dimensional non-Abelian quantum turbulence in a spin-2 condensate . . . . .	101
6.8. Summary . . . . .	107
<b>7. Conclusions</b>	<b>109</b>
<b>A. Spin-2 rotation matrix</b>	<b>113</b>
<b>B. Cyclic-tetrahedral non-Abelian vortices</b>	<b>115</b>
<b>C. Representation theory</b>	<b>119</b>
<b>D. Biaxial nematic non-Abelian vortex anyons</b>	<b>125</b>
<b>E. Fusion rules of the tau vortex anyon model</b>	<b>131</b>
<b>Bibliography</b>	<b>133</b>



# Chapter 1.

## Introduction

Topology has provided a rich perspective from which to characterise the physical properties of condensed matter systems. In the early 1970s, Berezinskii [1, 2], Kosterlitz, and Thouless [3, 4] applied topology to the study of phase transitions in two-dimensional condensed matter systems. Their work determined new phases of matter distinguished by phase transitions dictated by topology, with an absence of classical Landau type order parameters or even-long range order [5, 6]. Indeed, the Berezinskii–Kosterlitz–Thouless transition occurs via the unbinding of pairs of topological excitations. Nearly a decade later, Thouless and colleagues again applied the framework of topology to account for the robust quantised nature of the Hall conductance in the quantum Hall effect [7]. In recent years topological phases of matter have seen a resurgence of interest in condensed matter physics. The realisation of topological order has opened a new avenue for discovering new materials, such as topological insulators and superconductors [8], with unique properties dictated by topology. Further development of these materials promises future technological advancements potentially on par with the transistor revolution.

There is a wealth of interesting physics which occurs exclusively in two-dimensional systems. One exciting potential application of two-dimensional topological phases of matter is as a platform for quantum computing. The world’s ever growing hunger for computing is testing the limits of Moore’s law, the prediction that the number of transistors in an integrated circuit will double with each year. To keep up with demand, digital computing components must continue to shrink in size, approaching the limit at which quantum effects become non-negligible. Inevitably, quantum technologies will be required to maintain the growth in computational power. Rather than a looming cliff, this transition could be a fantastic opportunity. A quantum computer, based on unitary operations applied to quantum states called qubits, leverages inherently quantum effects—

like superposition and entanglement—to potentially solve certain problems faster than a classical (digital) computer [9]. Indeed, problems which are intractable on a classical computer—those that, with increasing complexity, scale exponentially in the required time or resources to solve—could be reformulated such that they are tractable using a quantum computer, scaling polynomially rather than exponentially. Such quantum algorithms could have significant implications for cryptography [10], the simulation of many-body problems in chemistry [11], and studies of knotted proteins in biology [12]. As an example, quantum algorithms have been developed for prime factorisation (Shor’s algorithm) [13], searches on unstructured databases (Grover search algorithm) [14], and for the calculation of knot invariants [15, 16]. Quantum computers entail an entirely new, probabilistic, way of doing computations. Moreover, there is strong evidence that there exists problems that may be solved on a quantum computer which cannot be solved on a digital computer [17].

Recent advances in quantum computing have come from intense research focus on qubits realised in a variety of systems, including trapped ions [18–20], spins in silicon atoms [21] and superconducting circuits [22]. However, such systems must contend with the accumulation of spontaneous errors due to the inherent interactions of the qubits with their environment, so called “decoherence” [23, 24]. Resilience against decoherence can be achieved by encoding quantum information into the topologically protected properties of certain two-dimensional topological phases of matter, a so called topological quantum computer [25]. In particular, the qubits in a topological quantum computer are constructed from the particle-like excitations—anyons—which have been predicted to emerge in these phases [26, 27]. Anyons are neither bosons nor fermions. When two anyons are exchanged the system’s wave function may accumulate an arbitrary geometric phase  $e^{i\theta}$ . For so called non-Abelian anyons the exchange phase may be expressed as a non-commutative matrix, specifically a unitary operator and how such anyons fuse (combine) when brought together depends on the history of their paths prior to the fusion. Encoding information in the non-local fusion properties of non-Abelian anyons forms a tantalising prospect for a realisation of a fault-tolerant quantum computer [28, 29]. Two promising non-Abelian anyon platforms are the Fibonacci and Ising anyon models [25, 30–33]. A number of experiments have explored the potential realisation of such anyons in condensed matter systems including Majorana zero modes [34–38, 38] and quasiparticles in certain fractional quantum Hall states [39–41]. Notwithstanding these experiments, the existence of a physical system of non-Abelian anyons capable of universal quantum computation remains an open question.

Topological excitations and their dynamics provide a myriad of interesting physics to study beyond their role in topologically ordered systems. Indeed, the study of these excitations has deep connections with symmetries and the theory of finite groups. For a detailed description of topological excitations see the review by Mermin in Ref. [42]. A topological excitation appears in an ordered medium as a spatial variation of the system's order parameter, one which cannot be removed by perturbations to the order parameter. Such excitations may arise in systems with either continuous or discrete broken symmetries and can be realised as point-like, line-like or planar-like objects, with names like vortices, monopoles, domain walls, skyrmions and so forth. Each topological excitation is characterised by a topological charge. Two topological excitations are of different type if their charges differ by more than an isomorphism. The topological charges are directly related to the broken symmetry of the order parameter. For systems where the broken symmetry corresponds to some non-Abelian group, i.e. a group containing elements that do not commute, it is possible to have so called non-Abelian topological excitations. The non-Abelian property of these excitations realises interesting topological interactions initiated upon fusion (collision) or under braiding of two excitations. It has been proposed that the topological interactions of vortex-like non-Abelian excitations ('fluxons'), along with additional charge-like particles, in two-dimensional high energy discrete gauge theories, provide the essential properties of a non-Abelian anyon model [43–45].

Topological excitations are ubiquitous in nature; notable examples are disclinations in liquid crystals [46, 47]; magnetic fluxes in superconductors [48]; vortices in superfluids [49, 50]; phase vortices in coherent optical [51] and electron [52] wavefields; and cosmic strings in high energy physics [53, 54]. Similarly, non-Abelian topological excitations are proposed to exist in models of cosmology [55], biaxial nematic liquid crystals [56, 57], neutron stars [58],  $d$ -wave Fermi condensates [59] and a number of discrete gauge theories in high energy physics [60, 61]. Topological excitations are also a burgeoning field of study in Bose–Einstein condensate (BEC) physics. Bose–Einstein condensates are an attractive system for studying topological excitations due to their high degree of controllability and the variety of realisable excitations. Furthermore, since topological phenomena are independent of the particular system characteristics, we can treat BECs as an emulator of many of the aforementioned systems.

Bose–Einstein condensates are a phase of matter characterised by the realisation of coherent long-range order in a gas of bosons, a manifestation of the quantum and statistical behaviour of bosons. By the early 1920s, Bose [62] and Einstein [63] had established the theoretical capacity of bosons to undergo condensation. However, it was

not until 1995 that a BEC was achieved experimentally in gases of bosonic rubidium [64] and sodium atoms [65] and later for lithium [66]. The experimental challenge was confronting the need for relatively high particle densities of  $10^{12}$ - $10^{15}$  atoms per  $\text{cm}^3$ , which are in fact dilute compared to air, and system temperatures on the order of nK. A particularly attractive feature of atomic condensates is the remarkable control that can be achieved over their properties. Feshbach resonances can be used to tune the particle interaction strengths [67], and arbitrary trapping potentials can be constructed to alter the dimensionality of the condensate [68]. Furthermore, there is an excellent correspondence between experimental results and the dominant mean-field theory treatment of BECs, allowing for accurate numerical simulation of BEC physics.

The prototypical topological excitation in a BEC is the quantum vortex. Spontaneous symmetry breaking during the phase transition of a single spin-component BEC results in a complex order parameter with phase symmetry. Onsager [69] and Feynman [70] determined that the vorticity in a single-component BEC is quantised and confined to topological excitations in the form of scalar quantum vortices characterised by  $2\pi$  phase dislocations in the condensate order parameter. In spinor Bose–Einstein condensates the atoms are trapped optically in all internal spin-components such that the spin degree of freedom results in a larger symmetry group of the pre-condensate state [71, 72]. Here, the BEC phase transition results in an array of different phases of matter with different broken symmetries. As a result, spinor condensates exhibit a great variety of topological excitations, where coreless vortices [73, 74], half-quantum vortices [75], baby skyrmions [74, 76, 77], monopoles [78–81], skyrmions [82] and knot solitons [83] have all been realised. Further phases of matter with potentially even more complicated symmetries could be found from mixtures of condensates of different spin states [84], and with the addition of spin-orbit coupling [85, 86].

Importantly, certain symmetry-broken phases of spinor BECs of atoms with spin  $F \geq 2$  can host non-Abelian topological excitations, in the form of non-Abelian vortices [87–89]. The simplest of these systems is the  $F = 2$  spinor condensate which supports two phases with non-Abelian vortices, the cyclic-tetrahedral and biaxial nematic superfluid phases [90]. Pioneering work by Kobayashi *et al.* [88] and more recently by Borgh and Ruostekoski [91] numerically demonstrated the collision dynamics of three-dimensional (3D) non-Abelian vortex lines in the cyclic-tetrahedral and biaxial nematic phases, respectively. Such collisions are topologically constrained to create a rung vortex bridging the two vortices. Comparatively, Abelian vortex lines—for example the scalar vortices—undergo reconnections in which the two colliding vortices separate after exchanging line sections

[92,93]. Similarly, rung formation collision dynamics have also been numerically observed for cosmic strings [55,94] and liquid crystal disclinations [56,57]. The dimensionality of the vortices has a marked effect on the vortex collision dynamics. In a two-dimensional (2D) condensate the reconnection event is replaced by vortex-antivortex annihilation [95–97]. Comparatively, the collision dynamics of two-dimensional non-Abelian vortices in spin-2 condensates remain unexplored.

Non-Abelian vortices in spinor condensates share many similarities with the fluxons in the discrete gauge theories, which were demonstrated to be non-Abelian anyons [43–45]. In the case of two-dimensional non-Abelian vortices, the collision dynamics map onto the anyon fusion rules. Furthermore, the non-trivial braiding dynamics is realised by a path dependent topological interaction, called the topological influence, which non-trivially permutes the topological charges of braided 2D non-Abelian vortices within their type [98]. Hence we may ask, are non-Abelian vortices in spinor condensates also non-Abelian anyons and could they be employed as a potential platform for topological quantum information storage and processing?

The chaotic fluid flow in a turbulent state is seeded by a disordered array of vortices. Turbulence remains one of the great unsolved problems in physics, with analytical approaches made intractable by the highly non-linear behaviour of the dynamics. However, characteristic properties of turbulent states can still be determined by looking statistically at certain revealing observables like the kinetic energy. In this respect, quantum turbulence, with its quantised vortices, is comparatively easier to visualise than classical turbulence where the vortex eddies are all of varying circulation. The dynamical evolution of the turbulent state is driven by the changing topology of the system due to collisions between vortices. The particular collision dynamics of the vortices play an important role in determining the properties of the turbulent state. For a 3D turbulent state of scalar vortices, a Richardson cascade [99] is realised wherein reconnection events transfer kinetic energy from large vortex loops to ever smaller vortex loops and eventually into sound waves [100]. The result is a self-similar direct energy cascade, spanning a broad range of length scales, characterised by the Kolmogorov  $-5/3$  power law scaling in spectra of the incompressible kinetic energy [101,102]. Comparatively, if we go to a 2D turbulent state of scalar vortices, vortex-antivortex annihilation is proposed to drive an inverse kinetic energy cascade, also with a  $-5/3$  power law scaling [103]. Physically, the inverse cascade proceeds via the clustering of vortices with like circulation into so called Onsager vortices [69,104,105], thereby transferring energy from the small length scales of individual vortices towards the large length scales of the Onsager vortices [103].

Altering the collision dynamics by changing the vortex algebra also results in turbulence with characteristically different properties. Kobayashi *et al.* [106] recently numerically demonstrated the potential existence of a novel topologically protected helicity cascade in a three-dimensional non-Abelian turbulent state. From the above results, one could infer that the novel collision dynamics of 2D non-Abelian vortices might also produce characteristically different types of 2D non-Abelian quantum turbulence.

This thesis presents a computational and theoretical study of the topological interactions of two-dimensional non-Abelian vortices in spin-2 Bose–Einstein condensates. The remainder of the thesis consists of five chapters, which are organised as follows.

Chapter 2 provides the essential theoretical framework that undergirds the results of this thesis. We provide an overview of spinor Bose–Einstein condensate theory, introducing the mean-field theory description of the spin-2 BEC and the spin-2 Gross–Pitaevskii equation, which forms the basis of the numerical simulations. The spin-2 BEC has a number of different symmetry-broken superfluid phases whose order parameter manifolds realise different types of quantised vortices. We detail the non-Abelian vortices in the cyclic-tetrahedral phase, characterising all the vortex types and their topological charges. The non-commuting algebra of the charges is realised in the non-trivial topological interactions of the vortices. We describe the topological interactions of these vortices by characterising the vortex collision dynamics and topological influence induced by the adiabatic exchange of vortices. To end the chapter, we discuss non-Abelian anyons and their applications in topological quantum computing

In Chapter 3 we provide the details of our numerical experiments. We detail the non-dimensionalised 2D spin-2 Gross–Pitaevskii equation and discuss the implementation of numerical algorithms to integrate it over a discrete field. We describe how initial states of non-Abelian vortices are prepared and also the numerical methods employed to locate and identify particular non-Abelian vortex types in our simulations.

Three results chapters are included, which characterise the topological interactions of two-dimensional non-Abelian vortices and their applications to interesting physical phenomena. While the investigations of each chapter are broadly self-contained, they are arranged to facilitate a logical flow from simple to more complex realisations of the topological interactions. Chapter 4 provides the foundational result used to motivate the applications in the following chapters. Here we present numerical experiments detailing the hitherto unexplored collision dynamics of vortices in the cyclic-tetrahedral phase of a two-dimensional spin-2 condensate. We describe the annihilation and pass through events

of Abelian spinor vortices and characterise a new collision event coined runghilation, which forms the 2D counterpart to rung formation of 3D non-Abelian vortices.

In Chapter 5 we show how our non-Abelian vortices may be non-Abelian anyons with potential for use in topological information processing and storage. We characterise the non-Abelian anyon models of these vortex ‘fluxons’, where the fusion and braiding rules map almost directly from the vortex collision dynamics in Chapter 4 and the topological influence in Sec. 2.7, respectively. Furthermore, we numerically demonstrate controlled braiding and fusing of the anyons to realise single and two-qubit unitary operations. We also present possible evidence of delocalised Cheshire charge in these systems.

Chapter 6 describes a method to controllably generate lattices of vortices with fractional mass and spin current circulation by employing the three source interference of spin-2 condensate fragments. Furthermore, we show that vortex lattices generated with this method can be used to seed a quantum turbulent state. Additionally, we artificially imprint many vortex initial states where the topological charges have either Abelian or non-Abelian algebra. By evolving these initial vortex configurations into a turbulent state, we reveal potential indicators of a new kind of 2D non-Abelian quantum turbulence.

Finally, we summarise all our results in Chapter 7 and map out potential future avenues of research.

## 1.1. List of publications

The results presented in this thesis stem from a number of published or submitted manuscripts. The publications are listed below.

- Chapter 4—Ref. [107]: T. Mawson, T. C. Petersen, and T. Simula, ‘*Collision dynamics of two-dimensional non-Abelian vortices*’, *Physical Review A* **96**, 033623 (2017).
- Chapter 5—Ref. [108]: T. Mawson, T. C. Petersen, J. K. Slingerland, and T. Simula, ‘*Braiding and fusion of non-Abelian vortex anyons*’, *Physical Review Letters* **123**, 140404 (2019).
- Chapter 6—Ref. [109]: T. Mawson, G. Ruben, and T. Simula, ‘*Route to non-Abelian quantum turbulence in spinor Bose–Einstein condensates*’, *Physical Review A* **91**, 063630 (2015).

# Chapter 2.

## Theoretical framework

In this chapter we outline the essential theoretical background of spinor Bose–Einstein condensates (BECs) and their vortex topological excitations. We begin by introducing the phenomenon of Bose–Einstein condensation and then provide the mean-field theory description for a spinor BEC of spin-2 atoms, the system of focus for this thesis. A description of the ground state phases of the spin-2 BEC and their broken symmetries is given with particular focus on the non-Abelian cyclic-tetrahedral phase. We thereby introduce a graphical representation of the spinor order parameter to elucidate transformations of the spinor order parameter. Different order parameter symmetries realise distinct types of topological excitations. Beginning from the simplest quantised vortices in scalar condensates we provide a characterisation of the vortex types in the cyclic-tetrahedral phase and their non-Abelian topological charges. Furthermore, we outline the impact the algebra of the topological charges has on the topological interactions which occur upon the collision or during the braiding of vortices. Finally, we provide an abridged description of non-Abelian anyons and topological quantum computing, using the Fibonacci anyon model as an example.

### 2.1. Bose–Einstein condensation

A wave function describing many indistinguishable particles accumulates a geometric phase under the exchange of two particles within the ensemble. The particular phase characterises the quantum statistics of the particles and specifies the elementary particle types. For a pair of identical particles in three spatial dimensions, adiabatically moving one particle on a full loop around the other is topologically equivalent to not moving the

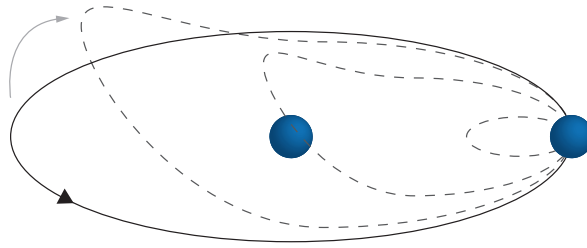


**Figure 2.1:** Two elementary particles (blue spheres) are adiabatically exchanged twice in three spatial dimensions. The exchange path may be smoothly deformed to a single point demonstrating the topologically trivial nature of exchanges in three dimensions.

particle at all, see Fig. 2.1. The accumulated geometric phase for such a path is  $e^{2\pi in}$ , where  $n$  is an integer. Consequently, after a single exchange the accumulated phase is either  $e^{2\pi in} = 1$ , corresponding to a wave function which is symmetric under exchange, or  $e^{(2n+1)\pi i} = -1$ , where the wave function is antisymmetric. These phases define two elementary particles<sup>1</sup>; bosons, with integer spin, and fermions, with half-integer spin, corresponding to the symmetric and anti-symmetric cases, respectively.

As a result of their different quantum statistics, bosons and fermions have distinct state occupancy rules. Due to their symmetry, an arbitrary number of identical bosons may simultaneously occupy the same state [62, 63]. However, fermions obey the Pauli exclusion principle [110] and two such particles can not simultaneously occupy the same state. Consequently, the respective many body states of bosons and fermions display different statistical behaviour. Bosons may undergo Bose–Einstein condensation, a quantum mechanical phase transition in which a macroscopic fraction of particles in a non-interacting Bose gas condense to occupy the same single particle state [63]. The condensate is a macroscopic quantum state identified by a complex order parameter imbued with long-range phase coherence and U(1) phase symmetry. The Bose–Einstein statistics impart a saturation value for the occupancy of the single particle excited states of a Bose gas, while also allowing the ground state to accommodate any remaining population. Saturation of the available excited energy states occurs at the BEC phase transition temperature,  $T_c$ , and further decreasing the temperature leads to an increasing fraction of the population occupying the single-particle ground state. For an ideal Bose gas, one without interactions, in a 3D box the condensate fraction  $N_0/N$  changes with

<sup>1</sup>Constraining the particles to two spatial dimensions leads to a situation of greater topological complexity resulting in additional quasiparticles called anyons. We will discuss anyons further in Sect. 2.8.

temperature as [111]

$$\frac{N_0}{N} = 1 - \left(\frac{T}{T_c}\right)^{3/2}, \quad (2.1)$$

where  $N$  and  $N_0$  are the particle number and condensate population, respectively, and the power  $3/2$  stems from the dimensionality of the system. As  $T \rightarrow 0$ , the condensate fraction  $N_0/N \rightarrow 1$ , with the non-condensate population existing in a thermal cloud which can be approximately described by classical Boltzmann statistics. An approximate value for the transition temperature can be calculated from the thermal de Broglie wavelength of the Bose gas, given by

$$\lambda = \frac{h}{\sqrt{2\pi M k_B T}}, \quad (2.2)$$

where  $M$  is the particle mass,  $k_B$  the Boltzmann constant and  $h$  is Planck's constant. The initiation of long-range coherence, heralding the formation of the condensate, occurs approximately when the thermal de Broglie wave length is of the order of the inter-particle spacing,  $n^{1/3}$ , where individual bosons are rendered indistinguishable by the overlap of their wave functions. According to this criterion the the transition temperature is

$$T_c \approx \frac{h^2}{2\pi M k_B n^{2/3}}. \quad (2.3)$$

In general, the particles interact and may be confined in different trapping potentials, both of which are accounted for by corrections to Eq. (2.2) and Eq. (2.3) [112].

This thesis focuses on condensates of atomic gases. The fundamental building blocks of atoms are fermions. For a neutral atom, with equal number of electrons and protons, an integer total spin  $F$  is guaranteed by an even number of neutrons. The hyperfine spin  $F = J + I$  corresponds to the sum of the spin angular momentum of the nucleus  $I$  with the total angular momentum of the electrons  $J = L + S$ , where  $L$  and  $S$  are the orbital and spin angular momentum, respectively. For zero magnetic fields the atoms can exist in any of  $2F + 1$  internal spin states, corresponding to the projections of the hyperfine spin. Experiments commonly consider gases of alkali atoms, typically sodium or isotopes of rubidium. Alkali atoms are characterised by an even number of neutrons, an odd number of protons, and a single electron in an unclosed shell with quantum numbers  $L = 0$  and  $S = 1/2$ . Hence, the total spin simplifies to  $F = I \pm 1/2$ , where  $I$  is a half-integer. More recently, experiments have considered higher spin atoms in the form of chromium [113], a transition metal, and the lanthanides, erbium [114], ytterbium [115, 116]

and dysprosium [117]. These are many-electron atoms whose partially filled shells lead to either large  $S$  or  $L$  quantum numbers and thus a high total spin.

Unlike ideal Bose gases, condensates of atomic gases involve interactions, the nature of which has interesting consequences for the magnetic order and topological properties of the system. For an overview of interactions between atoms, we refer to the standard text of Pethick and Smith in Ref. [111]. While atomic gases are many-body systems, at the comparatively low densities of BEC experiments, particle interactions predominately occur via binary collisions which can be understood through basic two-body quantum scattering theory. In quantum scattering, the initial and final states of the pair of atoms are described by internal quantum numbers which define a channel. The important quantum number is the total angular momentum of the pair  $\mathcal{F}_{\text{pair}} = \mathcal{L}_{\text{pair}} + F_{\text{pair}}$ , before ( $\mathcal{F}_{\text{pair,i}}$ ) and after ( $\mathcal{F}_{\text{pair,f}}$ ) scattering, where  $\mathcal{L}_{\text{pair}}$  is the orbital angular momentum of the pair, and  $F_{\text{pair}}$  is their spin angular momentum. However, at ultracold temperatures it will be found that, actually, only  $F_{\text{pair}}$  is relevant. To start with, we will focus on scattering within a single channel, corresponding to collisions in which the spin of the atoms does not change. For the alkali atoms commonly employed in BEC experiments, the dominant two-body interaction, relevant to scattering, is due to the van-der Waals interaction<sup>2</sup>—caused by the electric dipole-dipole interaction. The van der Waals interaction is rotationally symmetric<sup>3</sup> and thus conserves both orbital and spin angular momentum. However, it can change the internal spin state of the atoms. At ultracold temperatures, collisions occur with low energy and thus the scattering cross section is dominated by s-wave scattering ( $\mathcal{L}_{\text{pair}} = 0$ ), wherein it can be assumed that the scattering amplitude approaches a constant,  $a$ , the scattering length. Such interactions can be well described by an effective interaction, or pseudopotential,

$$v(\mathbf{r}, \mathbf{r}') = \frac{4\pi\hbar^2 a}{M} \delta(\mathbf{r}, \mathbf{r}'), \quad (2.4)$$

where the van der Waals interaction is simplified to a contact interaction in the form of a Dirac delta function with coupling constant  $g = 4\pi a\hbar^2/M$ . Depending on the sign of the scattering length the interactions can be either attractive,  $a < 0$  or repulsive,  $a > 0$ . In the former regime, the condensate may become unstable and can collapse [118]. Hence, we only consider positive scattering lengths.

---

<sup>2</sup>The atomic species chromium, erbium and dysprosium each have large magnetic dipole moments and hence Bose gases of these systems have an additional magnetic dipole-dipole interaction which cannot be ignored.

<sup>3</sup>The rotational symmetry holds in the absence of external magnetic fields or other external sources which may break the symmetry.

Early atomic BEC experiments employed magnetic fields to confine the atoms, resulting in the trapping of only the weak-field-seeking internal spin state. As such, the first atomic BECs were single component or scalar condensates, named with reference to the condensate order parameter which is a complex scalar field. The subsequent development of optical potentials allowed the trapping of atoms in all spin states and the realisation of spinor BECs with full internal spin degrees of freedom. As a result, interactions in a spinor condensate are a multi-channel process in which the spin of the colliding atoms may change. These spin exchanging collisions are incorporated into the Hamiltonian as additional spin interactions with the consequence that the Hamiltonian of a spinor BEC is characterised by a larger symmetry group. Under the assumption that the condensate particle density is spatially uniform<sup>4</sup> and that there exists no external magnetic fields, then the full symmetry group of a spinor condensate is  $U(1) \times SO(3)$  [119], corresponding to rotations of the phase and spin. As the spinor Bose gas condenses, spontaneous symmetry breaking permits an array of phases with different broken symmetries, each with distinct magnetic ordering and topological properties. The complexity and number of these phases increases with higher spin. In this thesis we focus on the topological properties of  $F = 2$  spinor BECs.

## 2.2. Mean field theory of spin-2 Bose–Einstein condensates

An exact description of a Bose–Einstein condensate of  $N$  interacting spin- $F$  atoms is given, in second quantization, by the bosonic field operators  $\hat{\psi}_m$  for particles in an eigenstate of  $\hat{F}_z$ , the  $z$ -component of the spin operator, indexed by the magnetic quantum number  $m = -F, \dots, F$ . Exactly solving many-body problems is intractable for even a modest number of particles. However, tractable and precise solutions to the many body problem can be obtained for dilute condensates with weak interactions in the zero temperature limit by considering the mean properties of bosons in a internal spin state  $m$  and condensed in the same single particle state. These are the mean-field and single mode approximations which replace the field operators with “classical” complex scalar fields  $\psi_m = \langle \hat{\psi}_m \rangle$  and which form the  $2F + 1$  components of a normalised spinor order

---

<sup>4</sup>For non-uniform condensates the magnitude of the spin is a further degree of freedom of the condensate alongside the orientation of the spin.

parameter,

$$\Psi(\mathbf{r}, t) = \frac{1}{\sqrt{n(\mathbf{r}, t)}} (\psi_F(\mathbf{r}, t), \dots, \psi_{-F}(\mathbf{r}, t))^T, \quad (2.5)$$

where  $n(\mathbf{r}, t) = \sum_{m=-F}^F |\psi_m(\mathbf{r}, t)|^2$  is the total particle density and  $T$  denotes the transpose. The order parameter  $\Psi$  is equivalently called the wave function of the condensate, with the choice of language depending on whether the physics of phase transitions or quantum mechanics are being invoked. In the context of BECs, the usual interpretation of  $|\psi_m(\mathbf{r}, t)|^2$  as the probability density is reinterpreted as the number density of the  $m^{\text{th}}$  internal spin state. As such the normalisation of the wave function is  $N = \int |\Psi(\mathbf{r}, t)|^2 d\mathbf{r}$ , for  $N$  particles.

A spin-2 Bose–Einstein condensate is described by a five component spinor order parameter. The Hamiltonian density of the system is

$$\mathcal{H} = H_0 + H_{\text{int}}, \quad (2.6)$$

where the single-particle part,

$$H_0 = \sum_{m=-2}^2 \psi_m^*(\mathbf{r}, t) [-\hbar^2 \nabla^2 / 2M + V(\mathbf{r}, t) - pm + qm^2] \psi_m(\mathbf{r}, t), \quad (2.7)$$

contains the kinetic energy; where  $\hbar = h/2\pi$ ,  $\nabla^2$  is the Laplacian operator and  $M$  is the mass of an atom; an external potential  $V(\mathbf{r}, t)$  and the linear,  $p$ , and quadratic,  $q$ , Zeeman energies associated with a non-zero external magnetic field. Throughout this thesis we consider the case of zero external magnetic fields ( $p = q = 0$ ), unless otherwise stated, which is sufficient to explore interesting non-commutative physics in the cyclic-tetrahedral superfluid phase. The remaining term in the Hamiltonian density describes the interactions. As discussed in Sec. 2.1, the interactions occur via s-wave ( $\mathcal{L}_{\text{pair}, i} = 0$ ) scattering of two atoms in the channel  $\mathcal{F}$ , which is simply characterised by the scattering length  $a_{\mathcal{F}}$ . Applying restrictions due to the bosonic quantum statistics enforces  $\mathcal{L}_{\text{pair}} + F_{\text{pair}}$  to be even. Furthermore, neglecting spin-orbit coupling implies  $\mathcal{L}_{\text{pair}}$  and  $F_{\text{pair}}$  are separately conserved during scattering. As such  $\mathcal{L}_{\text{pair}, i} = \mathcal{L}_{\text{pair}, f} = 0$  and thus  $\mathcal{F} = F_{\text{pair}}$ . Hence, the channels correspond to collisions of atoms with even total spin angular momentum, which for atoms with hyperfine spin  $F = 2$ , corresponds to  $\mathcal{F} = 0, 2, 4$ . Similar to Eq. 2.4, we can approximate the interactions with a Dirac

delta pseudopotential [71, 72, 120],

$$v(\mathbf{r}, \mathbf{r}') = \delta(\mathbf{r}, \mathbf{r}') \sum_{\mathcal{F}=0}^4 \frac{4\pi\hbar^2 a_{\mathcal{F}}}{M} \hat{P}_{\mathcal{F}}, \quad (2.8)$$

where the operator  $\hat{P}_{\mathcal{F}}$  projects a pair of atoms onto the state with even total spin  $F_{\text{pair}}$ . Following Ref. [120], we can use the identity operator for two spin-2 particles,

$$\hat{I}_1 \otimes \hat{I}_2 = \sum_{\mathcal{F}=0}^4 \hat{P}_{\mathcal{F}}, \quad (2.9)$$

$$= \hat{P}_0 + \hat{P}_2 + \hat{P}_4, \quad (2.10)$$

where  $\otimes$  is the tensor product, and the spin composition law,

$$\hat{F}_1 \cdot \hat{F}_2 = \sum_{\mathcal{F}=0}^4 \left[ \frac{1}{2} \mathcal{F}(\mathcal{F}+1) - F(F+1) \right] \hat{P}_{\mathcal{F}}, \quad (2.11)$$

$$= -6\hat{P}_0 - 3\hat{P}_2 + 4\hat{P}_4, \quad (2.12)$$

to re-express Eq. 2.8 as,

$$H_{\text{int}} = \frac{c_0}{2} \hat{I}_1 \otimes \hat{I}_2 + \frac{c_1}{2} \hat{F}_1 \cdot \hat{F}_2 + \frac{c_2}{2} \hat{P}_0. \quad (2.13)$$

The interaction strengths are specified by the effective coupling constants,  $c_0 = 4\pi\hbar^2(4a_2 + 3a_4)/7M$ ,  $c_1 = 4\pi\hbar^2(a_4 - a_2)/7M$  and  $c_2 = 4\pi\hbar^2(7a_0 - 10a_2 + 3a_4)/7M$  [119, 120]. Converting the operators into second quantization form and then making the mean-field approximation, the interaction term becomes,

$$H_{\text{int}} = \frac{c_0}{2} n(\mathbf{r}, t)^2 + \frac{c_1}{2} |\mathbf{F}(\mathbf{r}, t)|^2 + \frac{c_2}{2} |A(\mathbf{r}, t)|^2. \quad (2.14)$$

The interactions can be either spin-independent, depending on the total particle density  $n(\mathbf{r})$ , or spin-dependent, coupling the internal spin states via spin mixing collisions, which change the  $m$  quantum numbers of the colliding particles while conserving their total spin. There are two spin-dependent interactions. The first depends on the spin density vector  $\mathbf{F}(\mathbf{r}) = (F_x, F_y, F_z)$ , where  $F_\nu = \sum_{i,j=-2}^2 \psi_i^*(f_\nu)_{ij} \psi_j$  and  $f_\nu$  are the spin-2 Pauli

matrices,

$$f_x = \begin{pmatrix} 0 & 1 & 0 & 0 & 0 \\ 1 & 0 & \sqrt{\frac{3}{2}} & 0 & 0 \\ 0 & \sqrt{\frac{3}{2}} & 0 & \sqrt{\frac{3}{2}} & 0 \\ 0 & 0 & \sqrt{\frac{3}{2}} & 0 & 1 \\ 0 & 0 & 0 & 1 & 0 \end{pmatrix}, f_y = \begin{pmatrix} 0 & -i & 0 & 0 & 0 \\ i & 0 & -i\sqrt{\frac{3}{2}} & 0 & 0 \\ 0 & i\sqrt{\frac{3}{2}} & 0 & -i\sqrt{\frac{3}{2}} & 0 \\ 0 & 0 & i\sqrt{\frac{3}{2}} & 0 & -i \\ 0 & 0 & 0 & i & 0 \end{pmatrix}, f_z = \begin{pmatrix} 2 & 0 & 0 & 0 & 0 \\ 0 & 1 & 0 & 0 & 0 \\ 0 & 0 & 0 & 0 & 0 \\ 0 & 0 & 0 & -1 & 0 \\ 0 & 0 & 0 & 0 & -2 \end{pmatrix}. \quad (2.15)$$

The second depends on the spin-singlet pair amplitude  $A(\mathbf{r}) = (2\psi_2\psi_{-2} - 2\psi_1\psi_{-1} + \psi_0^2)/\sqrt{5}$ . The interactions mediated by  $c_1$  and  $c_2$  couple states separated by  $\Delta m = \pm 1$  and  $\Delta m = \pm 2, \pm 4$ , respectively, with their relative strengths determining the dominant channels.

Using a variational approach, the dynamics of the condensate at  $T = 0$  are described by

$$i\hbar \frac{\partial \psi_m}{\partial t} = \frac{\delta E}{\delta \psi_m^*}, \quad (2.16)$$

where  $E = \int \mathcal{H} d^3\mathbf{r}$  is the energy functional. Inserting the Hamiltonian density of Eq. (2.6) into Eq. (2.16) produces five coupled time-dependent Gross-Pitaevskii equations (GPE),

$$\begin{aligned} i\hbar \frac{\partial \psi_{\pm 2}}{\partial t} &= \left( -\frac{\hbar^2 \nabla^2}{2M} + V_{\text{ext}} \mp 2p + 4q + c_0 n \pm 2c_1 F_z - \mu \right) \psi_{\pm 2} \\ &\quad + c_1 F_{\pm} \psi_{\pm 1} + \frac{c_2}{\sqrt{5}} A \psi_{\mp 2}^*, \\ i\hbar \frac{\partial \psi_{\pm 1}}{\partial t} &= \left( -\frac{\hbar^2 \nabla^2}{2M} + V_{\text{ext}} \mp p + q + c_0 n \pm c_1 F_z - \mu \right) \psi_{\pm 1} \\ &\quad + c_1 \left( \frac{\sqrt{6}}{2} F_{\mp} \psi_0 + F_{\pm} \psi_{\pm 2} \right) - \frac{c_2}{\sqrt{5}} A \psi_{\mp 1}^*, \\ i\hbar \frac{\partial \psi_0}{\partial t} &= \left( -\frac{\hbar^2 \nabla^2}{2M} + V_{\text{ext}} + c_0 n - \mu \right) \psi_0 \\ &\quad + c_1 \frac{\sqrt{6}}{2} (F_+ \psi_1 + F_- \psi_{-1}) + \frac{c_2}{\sqrt{5}} A \psi_0^*, \end{aligned} \quad (2.17)$$

where  $\mu$  is the chemical potential, and  $F_{\pm}$  and  $F_z$  are the total angular momentum ladder operators and magnetisation, respectively, given by

$$F_+ = F_-^* = 2(\psi_2^* \psi_1 + \psi_{-1}^* \psi_{-2}) + \sqrt{6}(\psi_1^* \psi_0 + \psi_0^* \psi_{-1}), \quad (2.18)$$

$$F_z = 2(|\psi_2|^2 - |\psi_{-2}|^2) + |\psi_1|^2 - |\psi_{-1}|^2. \quad (2.19)$$

These non-linear Schrödinger type equations can be solved numerically to provide a remarkably accurate representation of the condensate dynamics. In Chapter 3 we provide details of our procedure to numerically solve the GPE for a two-dimensional condensate.

## 2.3. Superfluid phases and order-parameter manifolds

The symmetries of a BEC are given by a group of transformations operating on the space of order parameters which leave the energy functional invariant. The full symmetry group of a spinor BEC, assuming a spatially uniform system and the absence of external magnetic fields, is  $G = \text{U}(1) \times \text{SO}(3)$ , an element of which can be written as  $g \equiv R = e^{i\phi} e^{-if_z \alpha} e^{-if_y \beta} e^{-if_z \gamma}$ , where  $\phi$  is a phase angle and  $\alpha, \beta, \gamma$  are Euler angles describing the spin rotation. The condensate phase transition to a ground state phase with particular order parameter  $\Psi$  is characterised by a spontaneous symmetry-breaking of  $G$  to a subgroup  $H$ , the so called isotropy group of transformations that leave  $\Psi$  invariant. Each phase is in fact described by a set of degenerate order parameters, called an orbit, generated by acting with the elements of  $G$  on  $\Psi$ . The isotropy group of each point  $\Psi' = g\Psi$  in the orbit is the group  $H' = gHg^{-1}$  formed from the conjugation of  $H$ . The corresponding orbit of the isotropy group is given by the left cosets of  $H$  defined as  $G/H = \{gH \mid g \in G\}$  and is used to define the order-parameter manifold  $\mathcal{M} = G/H$  of the corresponding state. The addition of external magnetic fields introduces further symmetry breaking which may lift the degeneracy of order parameters sharing an orbit, further splitting the ground state phase diagram [121].

The spin-2 condensate ground state phase diagram can be determined by minimising the spin-dependent part of the spin-2 energy functional over the regime of  $c_1$  and  $c_2$  spin interaction strengths. The magnetic ordering of each phase is characterised by the values of  $|\mathbf{F}(\mathbf{r})|$  and  $|A(\mathbf{r})|$ . For zero external magnetic fields ( $p = q = 0$ ), the phase diagram, shown in Fig. 2.2(a), consists of three phases: ferromagnetic, nematic and

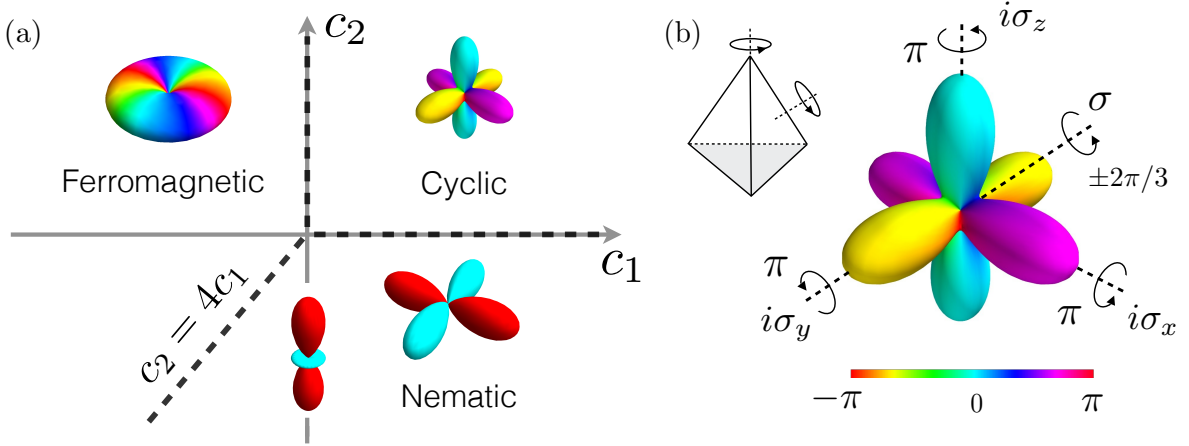


**Figure 2.2:** Ground state phases of the spin-2 BEC for zero magnetic field. (a) Phase diagram of the spin-2 condensate. A representative order parameter is shown for each phase using the spherical harmonic representation. (b) Tetrahedral symmetry of the cyclic-tetrahedral ground state phase wave function. Each symmetry axis is labelled by a spin-1/2 Pauli matrix and phase angle, corresponding to the appropriate spin and phase rotation, for a choice of basis.

cyclic-tetrahedral [90, 122–124]. Furthermore, we illustrate the order parameter of each phase in Fig. 2.2(a) using the spherical harmonic representation [119] by decomposing the order parameter in terms of a weighted sum of spherical harmonics,

$$\Psi(\theta, \phi) = \sum_{m=-F}^F \psi_m Y_F^m(\theta, \phi), \quad (2.20)$$

where  $Y_F^m$  is a spherical harmonic function, and in this context  $\theta$  is the polar angle and  $\phi$  the azimuthal angle of the spherical coordinate system. Explicitly, the shape of the 3D spherical harmonic objects in Fig. 2.2 corresponds to an isosurface of  $|\Psi(\theta, \phi)|^2$ , while the colour is given by the phase of  $\Psi(\theta, \phi)$ . We will make repeated use of this representation throughout this thesis to explore the symmetries of order parameters and their topological excitations.

The ferromagnetic phase, occurring for  $c_1 < 0$  and  $c_2 > 4c_1$ , is characterised by non-zero  $|\mathbf{F}(\mathbf{r})|$  and  $|A(\mathbf{r})| = 0$ . A ferromagnetic phase order parameter is given by  $\Psi_{\text{ferro}} = R(1, 0, 0, 0, 0)^T$ , where the explicit spin-2 phase and spin rotation matrix,  $R$ , is given in Appendix A. The isotropy group is  $H = \text{SO}(2)_{2\phi, f_z}$  [125, 126], which corresponds to simultaneous continuous rotations of the phase and spin (about the axis  $f_z$ ) where the phase rotation angle is twice that of the spin. Consequently, the order-parameter manifold is  $\mathcal{M} = \text{SO}(3)_{2\phi, f_z}$ .

The nematic phase, occurring for  $c_1 > 0$  and  $c_2 < 4c_1$ , is characterised by  $|\mathbf{F}(\mathbf{r})| = 0$  and non-zero  $|A(\mathbf{r})|$ . The nematic phase order parameter is given by  $\Psi_{\text{nematic}} = (\sin(\epsilon)/\sqrt{2}, 0, \cos(\epsilon), 0, \sin(\epsilon)/\sqrt{2})^\top$ , which depends on the parameter  $\epsilon$ . At the mean field level, there are three degenerate nematic phases with distinct order parameter symmetries; uniaxial, for  $\epsilon = 0$ ; biaxial, for  $\epsilon = \pi/6$ ; and dihedral-2 [121], for all other values. The degeneracy is lifted by quantum and thermal fluctuations, initiating a phase transition between the uniaxial and biaxial phases which depends on the scattering lengths [127, 128]. The isotropy group for the uniaxial phase is the  $H = D_\infty \cong \text{SO}(2) \rtimes \mathbb{Z}_2$  and the order-parameter manifold is  $\mathcal{M} = [\text{U}(1) \times \text{S}^2] / \mathbb{Z}_2$  [127, 129], where  $\cong$  denotes an isomorphism and  $\rtimes$  is a semidirect product. The biaxial phase is symmetric under  $H = D_4$ , the dihedral group of order 8, with elements corresponding to joint  $\text{U}(1)$  and  $\text{SO}(3)$  rotations. Hence, the order-parameter manifold is  $\mathcal{M} = [\text{U}(1) \times \text{SO}(3)] / D_4$  [127].

The cyclic-tetrahedral phase, occurring for  $c_1 > 0$  and  $c_2 > 0$ , is characterised by  $|\mathbf{F}(\mathbf{r})| = 0$ ,  $|A(\mathbf{r})| = 0$  and broken time-reversal symmetry. An example order parameter is  $\Psi_{\text{cyclic}} = R(i, 0, \sqrt{2}, 0, i)^\top / 2$  which has tetrahedral symmetry  $H = T$ , see Fig. 2.2(b), as per the name<sup>5</sup>. The tetrahedral symmetry group  $T$  in this context is the subgroup of  $\text{U}(1) \times \text{SO}(3)$ , not just  $\text{SO}(3)$ , with both rotations of the phase and spin. The corresponding order-parameter manifold is  $\mathcal{M} = [\text{U}(1) \times \text{SO}(3)] / T$  [87, 125]. The tetrahedral symmetry group is non-Abelian, i.e. contains elements that do not commute under the group operation. Thus, the cyclic-tetrahedral phase is denoted a non-Abelian phase. Similarly,  $D_4$  is also a non-Abelian group and thus the biaxial nematic phase is another non-Abelian phase. Such phases may host interesting topological excitations called non-Abelian vortices, see Section 2.5.

## 2.4. Topological excitations in Bose-Einstein condensates

Bose–Einstein condensates feature a number of excitations, among the richest of which are the topological excitations. The possible types of topological excitations and their characteristics depend on the symmetries of the superfluid phases. In this section, we

<sup>5</sup>The literature also commonly refers to the cyclic-tetrahedral phase as simply the cyclic phase, a name inherited from the phases of the d-wave superconductor which have order parameters in one-to-one correspondence with those of the spin-2 condensate [90].

will detail some of the interesting varieties of topological excitations in scalar and spinor condensates.

The archetypal topological excitation of a BEC is the quantum vortex in a scalar condensate. In the hydrodynamic formulation the scalar order parameter may be written in terms of the density  $n(\mathbf{r}, t)$  and a phase  $\theta(\mathbf{r}, t)$  using the Madelung transformation [130],

$$\Psi(\mathbf{r}, t) = \sqrt{n(\mathbf{r}, t)} e^{i\theta(\mathbf{r}, t)}. \quad (2.21)$$

The mass current density is calculated as

$$\mathbf{j} = \frac{\hbar}{2Mi} [\psi^*(\mathbf{r}, t) \nabla \psi(\mathbf{r}, t) - \psi(\mathbf{r}, t) \nabla \psi^*(\mathbf{r}, t)] = \frac{\hbar}{M} n(\mathbf{r}, t) \nabla \theta(\mathbf{r}, t), \quad (2.22)$$

where the final expression is obtained after substitution of Eq. (2.21). The superfluid velocity  $\mathbf{v}$  is related to the mass current density by  $\mathbf{j} = n\mathbf{v}$  and thus to the condensate phase as  $\mathbf{v} = \hbar/M\nabla\theta$ . By implication, the condensate is irrotational since the vorticity  $\boldsymbol{\omega} = \nabla \times \mathbf{v} = 0$ . This result holds when the velocity field is continuous but is no longer valid when there is a discontinuity in the phase due to the presence of a vortex. The characteristic mass current circulation of a vortex arises from the change in the phase along a closed path  $\Gamma(s)$ , for a curve parameter  $s$ , enclosing the vortex core; see the schematic in Fig. 2.3(a). Due to the single-valuedness of the order parameter the phase must rotate by an integer multiple of  $2\pi$  along  $\Gamma(s)$ . As such, the circulation,

$$\oint_{\Gamma} d\mathbf{l} \cdot \mathbf{v} = \omega \kappa, \quad (2.23)$$

is quantised in integer multiples of the quanta of circulation  $\kappa = \hbar/M$ , where the integer  $\omega$  is the winding number or topological charge of the vortex. By convention, positive and negative winding numbers refer to vortices and anti-vortices, respectively. The discontinuity in the phase, where the vortex velocity  $\kappa\omega\phi/r$  diverges and its vorticity  $\nabla \times \mathbf{v} = \kappa\omega\delta(r - r')\mathbf{z}$  is localized, is dealt with by a zero in the order parameter due to the vortex core. Here,  $\delta(r - r')$  is a Dirac delta function. A condensate containing vortices is therefore topologically a multiply connected state.

A representative vortex solution of the GPE is the straight line vortex, aligned along the z-axis, represented in cylindrical co-ordinates by

$$\Psi = f(r) e^{i\phi}, \quad (2.24)$$

where  $f(r)$  describes the density profile and  $\phi$  the phase. In a uniform condensate  $f(r)$  can be reasonably approximated as [111, 131]

$$f(r) = \frac{r}{\sqrt{r^2 + 2\xi^2}}, \quad (2.25)$$

where  $\xi = \hbar/\sqrt{2M|c_0|n}$  is the healing length, defined as the distance over which the condensate “heals” back to the bulk value after some large perturbation. Within the vortex core, when  $r < \xi$ ,  $f(r)$  goes linearly to zero, while far from the vortex core  $f(r) \rightarrow 1$ , the bulk value of the condensate. A more accurate approximation of the core profile has been made by Bradley and Anderson in Ref. [132].

In general, quantum vortices are characterised by how their order parameter changes along a closed path enclosing the vortex core. Consequently, the types of vortices that can be excited in a BEC ground state phase are determined by the symmetries of the system’s order parameter and are classified according to homotopy theory, see Mermin [42] for a detailed review. For line excitations, the classification occurs by mapping each point on the real path  $\Gamma(s)$  in the condensate to a path  $\Psi(\Gamma)$  in the corresponding order-parameter manifold. Two paths in the order-parameter manifold are homotopic if they share a base point  $x_0 \in \mathcal{M}$  and can be smoothly deformed into each other. The homotopic paths form equivalency classes, which are the elements of the fundamental group  $\pi_1(\mathcal{M}, x_0)$ , where

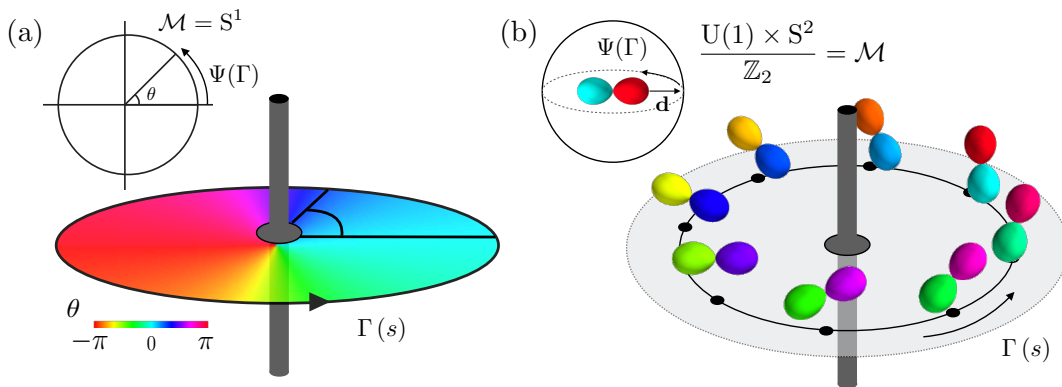


**Figure 2.3:** Schematic illustrations of quantum vortices in a BEC. (a) A scalar vortex. The vortex phase structure is given for a two-dimensional plane intersecting the vortex core denoted by the grey cylinder. (b) A half quantum vortex in the polar phase of the spin-1 condensate. The polar phase order parameter is represented using the spherical harmonic decomposition. The half quantum vortex is then characterised by the rotation of the spherical harmonics across the discrete points on the two-dimensional plane represented by the light grey disc. The real space paths  $\Gamma(s)$ , encircling the vortex cores, map to paths  $\Psi(\Gamma)$  in the respective order parameter manifolds inset in each sub-figure.

the subscript identifies that the map is from a one-dimensional loop in real space to the order parameter manifold. Each element of  $\pi_1(\mathcal{M}, x_0)$  corresponds to a topological charge characterising a particular vortex. In the context of Chap. 5, the charges will be referred to as fluxes. If  $\mathcal{M} = G/H$  is simply connected, and  $H$  is a discrete group, then  $\pi_1(\mathcal{M}, x_0) \cong H$ . In this case, the topological charge can be equivalently defined as the transformation in  $H$  that describes the change in the order parameter along a path enclosing the vortex core. Revisiting the scalar vortex, the order parameter changes by  $2\pi\omega$  along a closed path about the vortex core and thus the order parameter manifold is  $U(1) \cong S^1$ , where  $S^1$  is the 1-sphere, or unit circle. As shown in Fig. 2.3(a), the closed path  $\Gamma(s)$  in real space maps to a path  $\Psi(\Gamma)$  in the order parameter manifold equivalent to a winding about the 1-sphere. The number of times the path covers the 1-sphere is given by  $\pi_1(S^1) = \mathbb{Z}$ , corresponding to  $\omega$ , the integer winding numbers.

In spinor condensates, the additional spin degree of freedom, and thus the multitude of different order-parameter manifolds, permits topological excitations that can not be realised in the scalar condensate. In particular, condensates with order parameters with discrete symmetry may permit vortices with fractional quanta of circulation [125, 126]. Such fractional-charge vortices are characterised by a change in the order parameter by a simultaneous phase and spin rotation. An illustrative example is the half quantum vortex<sup>6</sup> in the polar phase of the spin-1 condensate [75, 135]. The 3-component polar superfluid phase order parameter may be represented as  $\Psi_{\text{polar}}^{(1)} = (0, 1, 0)^T$  [119]. A general element of the corresponding orbit is characterised by a phase  $\theta$  and vector  $\mathbf{d} = (\cos \alpha \sin \beta, \sin \alpha \sin \beta, \cos \beta)$  with manifolds  $U(1)$  and  $S^2$ , respectively. The polar phase has a continuous  $SO(2)$  symmetry, consisting of rotations about  $\mathbf{d}$ , and a discrete  $\mathbb{Z}_2$  symmetry [136], corresponding to operations which “invert” the order parameter via composite rotations of the form  $(\phi, \mathbf{d}) \rightarrow (\phi + \pi, -\mathbf{d})$ . It follows that the order parameter manifold is  $\mathcal{M} = U(1) \times S^2/\mathbb{Z}_2$ . The half quantum vortex, a schematic representation of which is shown in Fig. 2.3(b), arises from the discrete  $\mathbb{Z}_2$  symmetry as a continuous  $\pi$  spin rotation, inverting the  $\mathbf{d}$  vector, and a concurrent  $\pi$  phase rotation to preserve the single-valuedness. A representative half quantum vortex order parameter is

$$\Psi = \sqrt{n} e^{i\frac{\theta}{2}} e^{-i\frac{\theta}{2}f_z} e^{-i\frac{\pi}{2}f_y} \Psi_{\text{polar}}^{(1)} = \sqrt{\frac{n}{2}} \begin{pmatrix} -1 \\ 0 \\ e^{i\omega\theta} \end{pmatrix}. \quad (2.26)$$

<sup>6</sup>Sometimes also referred to as Alice vortices [133], a convention inherited from high energy physics [134].

The topological charges are given by  $\pi_1(\text{U}(1) \times \text{S}^2/\mathbb{Z}_2) = \mathbb{Z}$ , corresponding to integer winding numbers, same as the scalar vortices. However, unlike the scalar vortices, the discrete symmetries of the half quantum vortex result in a mass current circulation  $\oint_{\Gamma} d\mathbf{l} \cdot \mathbf{v}^{\text{HQ}} = \frac{\hbar}{2M}\omega$ , quantised in integer units of half the quanta of circulation. Furthermore, the rotation of the  $\mathbf{d}$  vector about the core characterises a spin texture with quantised spin current circulation  $\oint_{\Gamma} d\mathbf{l} \cdot (\mathbf{v}_s^{\text{HQ}})_z = -\frac{\hbar}{2M}\omega$ , where  $(\mathbf{v}_s^{\text{HQ}})_z$  is the z-component of the spin velocity

$$(\mathbf{v}_s)_\nu = \frac{\hbar}{2Mni} \sum_{m,m'=-2}^2 (f_\nu)_{m,m'} [\Psi_m^* (\nabla \Psi_{m'}) - (\nabla \Psi_m^*) \Psi_{m'}]. \quad (2.27)$$

Although the half quantum vortex displays a singularity in superfluid velocity, the vortex core is not empty. For the particular half quantum vortex in Eq. (2.26), the phase discontinuity, and the associated zero in the order parameter, is present in the  $m = -1$  component. As such, the vortex core is filled with atoms in the  $m = 1$  component and thus belongs to the ferromagnetic phase [137–139], an entirely different superfluid phase to the condensate bulk. The size of the core is, thus, of the order of the spin healing length  $\xi_i = \hbar/\sqrt{2M|c_i|n}$  [138].

The other possible superfluid phase of a spin-1 condensate, in the absence of external magnetic fields, is the ferromagnetic phase. A representative 3-component spin-1 ferromagnetic superfluid phase order parameter is  $\Psi_{\text{ferro}}^{(1)} = (1, 0, 0)^{\text{T}}$  characterised by a continuous symmetry  $H = \text{SO}(2)_{\phi, f_z}$ , where the subscripts denote the coupled nature of the phase and spin rotations [119]. The corresponding order parameter manifold is  $\mathcal{M} = \text{SO}(3)_{\phi, f_z}$ . The first homotopy group  $\pi_1(\text{SO}(3))$  is, in general, trivial except for loops which map to paths in the order parameter manifold connecting antipodal points [140]. As a result,  $\pi_1(\text{SO}(3)) = \mathbb{Z}_2$  and the corresponding integer charge vortices are the  $\text{SO}(3)$  or polar core vortices [141], so named due to the  $m = 0$  atomic population residing in the vortex core. For a schematic representation of the polar core vortex we refer to Fig. 24(a) in Ref. [119]. The spontaneous formation of polar core vortices was observed by Sadler et al. [142].

The second homotopy group,  $\pi_2$ , defined by a mapping from a closed surface in real space to the order parameter manifold, classifies point type excitations, such as monopoles. Homotopy groups beyond  $\pi_1$  are trivial for the scalar condensate, hence it only hosts line type excitations. However, the spin-1 polar superfluid phase, where  $\pi_2(\text{S}^2) = \mathbb{Z}$ , can host topologically stable 't Hooft-Polyakov monopoles [143, 144] characterised by a radial

or hedgehog texture  $\mathbf{d}(\mathbf{r}) = \mathbf{r}/r$  [145]. The 't Hooft-Polyakov monopole is energetically unstable to decaying into an Alice ring, a half quantum vortex ring with both  $\pi_1$  and  $\pi_2$  charges [137]. The 't Hooft-Polyakov monopole has been experimentally realised by Ray et al. [80], using a quadrupole magnetic field to adiabatically generate the  $\mathbf{d}$  vector texture, equivalent to applying a spatially non-uniform spin rotation. The second homotopy group is trivial for the spin-1 ferromagnetic superfluid phase and hence the phase does not support topologically stable point type monopole excitations. However, Savage and Ruostekoski [146] demonstrated that Dirac monopoles [147] can be realised in this phase. Here, a hedgehog spin texture is generated at the terminating end of a doubly quantized vortex line, analogous to the Dirac string, with the corresponding superfluid velocity profile of the spin texture taking the characteristic form of the vector potential of a Dirac monopole. As both monopoles and doubly quantised vortices are trivial topological objects in the spin-1 ferromagnetic phase, the Dirac string prefers to untwine into two singly charged vortices resulting in the Dirac monopole continuously transforming into a non-singular spin texture [146]. Dirac monopoles have been experimentally realised using synthetic gauge fields [78]. Furthermore, it has been experimentally demonstrated that the 't Hooft-Polyakov monopole can transform into a Dirac monopole during a transition between the polar and ferromagnetic phases [79].

The second homotopy group also describes topologically stable non-singular soliton excitations—excitations without a phase singularity. The spin-1 polar superfluid phase hosts baby (2D) skyrmions, characterised by a fountain-like texture in the  $\mathbf{d}$  vector, where the  $\mathbf{d}$  vector points upward in the centre of the condensate and downwards at the boundary. We refer to Fig. 34(c) in Ref. [119] for a schematic representation of this texture. A similar spin texture can be realised in the spin-1 ferromagnetic phase, where the phase-spin rotation coupling means non-singular mass current flows can be realised from spin textures [71, 148–151]. Such non-singular coreless vortices are characterised by a spin texture where the order parameter transforms from  $(1, 0, 0)^T$ , at the ‘core’, to the doubly quantized vortex texture  $(0, 0, e^{2i\theta})^T$ , at the condensate boundary. For a schematic representation of the ferromagnetic coreless vortex we refer to Fig. 24(c) in Ref. [119]. The coreless vortex is similar to the Anderson-Toulouse and Mermin-Ho vortices in superfluid  $^3\text{He}$  [152, 153]. The coreless vortex is not topologically stable and is homotopic to the vortex free  $\Psi_{\text{ferro}}^{(1)}$  order parameter [154]. Both baby skyrmions and coreless vortices have been experimentally realised [74, 76] using the same techniques as Ref. [80] to imprint the characteristic nematic or spin texture via a spatially non-uniform adiabatic rotation of the spins.

The third homotopy group  $\pi_3$  describes 3D skyrmion and knot solitons. For both the spin-1 polar and ferromagnetic phases,  $\pi_3(\mathcal{M}) = \mathbb{Z}$ , with topologically stable knots [83] and 3D Shankar skyrmions [82] experimentally realised in these phases, respectively.

The superfluid phases apparent in spin-2 condensates similarly permit a number of interesting topological excitations, with coreless vortices [119], fractional circulation vortices [125] and Shankar skyrmions [155], all predicted by theory but yet to be pursued in experiment. Furthermore, the spin-2 interaction parameters introduce condensates with order parameter manifolds characterised by non-Abelian symmetry groups. The first homotopy group of a non-Abelian symmetry group realises non-commutative topological charges, with interesting consequences for the topological interactions of such non-Abelian vortices. In section 2.5, we will describe in detail the fractional vortices of the non-Abelian cyclic-tetrahedral phase [87, 89, 125, 126] which form the basis of the studies in this thesis.

## 2.5. Non-Abelian vortices in the cyclic-tetrahedral phase

The vortices explicitly described in the previous section are examples of Abelian vortices. When the fundamental group is non-Abelian, i.e. contains some elements that do not commute under the group operation, the corresponding topological excitations are called non-Abelian vortices<sup>7</sup>. Since  $\text{SO}(3)$  is not simply connected, the topological charges of spinor vortices are typically characterised in the simply connected covering group  $\text{SU}(2)$ . Of the possible subgroups of  $\text{SU}(2)$ , the binary dihedral  $D_n^*$ , binary tetrahedral  $T^*$ , binary octahedral  $O^*$ , and binary icosahedral  $Y^*$  groups are non-Abelian and correspond to phases with non-Abelian vortices. Such phases occur for spin- $F$  BECs, for  $F \geq 2$  [156–161]. Hence, non-Abelian phases are relatively common in spinor condensates.

The spin-2 condensate has two non-Abelian phases, the biaxial nematic and cyclic-tetrahedral, which can host non-Abelian vortices. In this thesis we focus on non-Abelian vortices in the cyclic-tetrahedral phase, since for zero external magnetic fields the biaxial phase and the Abelian uniaxial nematic phase are degenerate. Though, for the sake of completeness, a description of the vortices in the biaxial nematic phase is given in Appendix D. A representative cyclic-tetrahedral phase order parameter is given by  $\Psi_{\text{cyclic}} = (i, 0, \sqrt{2}, 0, i)^T/2$ . The order-parameter manifold of the cyclic-

<sup>7</sup>Elsewhere in the literature non-Abelian vortices are defined to occur when; (1) the full symmetry group  $G$  is non-Abelian, or (2) the isotropy group  $H$  is non-Abelian.

tetrahedral phase is  $\mathcal{M}^{\text{cyc}} = \text{U}(1) \times \text{SU}(2)/T^*$ . Hence, the cyclic-tetrahedral phase order parameter is invariant under the action of the 24 elements of the isotropy group  $H = T^*$ , which consists of discrete composite  $\text{U}(1)$  gauge and  $\text{SU}(2)$  spin rotations. As  $\mathcal{M}^{\text{cyc}}$  is simply connected and  $H$  is a discrete group,  $\pi_1(\mathcal{M}^{\text{cyc}}) \cong T^*$  and each element of  $T^*$  corresponds to a topological charge of a distinct vortex. Furthermore, each vortex is categorised into a vortex type according to its equivalency class—the set of charges  $\text{Cl}(\gamma) = \{\gamma' \in H \mid \exists g \in H \text{ with } \gamma = g\gamma'g^{-1}\}$ . The transformation  $g\gamma g^{-1}$  here is the equivalency relation or conjugation. There is no unique way to assign each topological charge in an equivalency class to each vortex in the corresponding vortex type. Each such assignment is related by an isomorphism corresponding to the rotation of the entire equivalency class by the equivalency relation for a group element  $g \in T^*$ . As a result, vortices with different charges in the same equivalency class are indistinguishable and individual vortices are classified by the equivalency class alone.

For each winding number of the  $\text{U}(1)$  phase rotation, the cyclic-tetrahedral phase vortices are categorised in seven equivalency classes I-VII [87, 88, 125, 126]. The vortex types are: (I) the vacuum state; (II) the integer spin vortex; (III) the half quantum spin vortex; (IV) and (V) the  $1/3$  fractional vortices and (VI) and (VII) the  $2/3$  fractional vortices. The charges of each class are [87]

$$\begin{aligned}
\text{(I)} & \{(\eta, \mathbb{I})\} \\
\text{(II)} & \{(\eta, -\mathbb{I})\} \\
\text{(III)} & \{(\eta, i\sigma_\nu), (\eta, -i\sigma_\nu)\} \\
\text{(IV)} & \{(\eta + 1/3, \tilde{\sigma}), (\eta + 1/3, -i\sigma_\nu\tilde{\sigma})\} \\
\text{(V)} & \{(\eta + 1/3, -\tilde{\sigma}), (\eta + 1/3, i\sigma_\nu\tilde{\sigma})\} \\
\text{(VI)} & \{(\eta + 2/3, -\tilde{\sigma}^2), (\eta + 2/3, -i\sigma_\nu\tilde{\sigma}^2)\} \\
\text{(VII)} & \{(\eta + 2/3, \tilde{\sigma}^2), (\eta + 2/3, i\sigma_\nu\tilde{\sigma}^2)\}, \tag{2.28}
\end{aligned}$$

where the  $\text{U}(1)$  component is represented by a winding number  $\eta \in \mathbb{Z}$  plus a class specific constant, and the  $\text{SU}(2)$  part by the spin-1/2 Pauli matrices  $\sigma_\nu$ , for  $\nu = x, y, z$ , and  $\tilde{\sigma} \equiv (\mathbb{I} + i\sigma_x + i\sigma_y + i\sigma_z)/2$ .

We represent each topological charge with a shorthand notation  $\pm X_\eta^\nu \equiv (\eta + a_X, g_X^\nu)$ . The  $X$  is a Roman numeral corresponding to the class number. The subscript  $\eta$  is the winding number of the  $\text{U}(1)$  rotation, which appears in the topological charge along with

**Table 2.1:** Explicit order parameters for a representative set of cyclic-tetrahedral phase vortices. For each vortex, labelled  $\pm X_\eta^\nu$ , we provide the corresponding rotation  $R(\theta; \pm X_\eta^\nu)$ , in terms of an angle  $\theta$ , which acts on  $\Psi_{\text{cyclic}}$  to generate the order parameter  $\Psi(\mathbf{r}; \pm X_\eta^\nu)$ . In some cases we apply an additional rotation  $S = \exp(i \cos^{-1}(1/\sqrt{3})f_y) \exp(i\pi f_z/4)$  to obtain a simpler order parameter structure.

$\pm X_\eta^\nu$	$R(\theta; \pm X_\eta^\nu)$	$\Psi(\mathbf{r}; \pm X_\eta^\nu)$
$I_0$	$\mathbb{I}$	$(\frac{i}{2}, 0, \frac{\sqrt{2}}{2}, 0, \frac{i}{2})^\top$
$-\text{II}_0$	$e^{-i\theta f_z}$	$(\frac{i}{2}e^{-2i\theta}, 0, \frac{\sqrt{2}}{2}, 0, \frac{i}{2}e^{2i\theta})^\top$
$\text{III}_0^z$	$e^{-i\frac{\theta}{2}f_z}$	$(\frac{i}{2}e^{-i\theta}, 0, \frac{\sqrt{2}}{2}, 0, \frac{i}{2}e^{i\theta})^\top$
$\text{IV}_0$	$S e^{i\frac{\theta}{3}} e^{-i\frac{\theta}{3} \frac{(f_x+f_y+f_z)}{\sqrt{3}}}$	$(0, \sqrt{\frac{2}{3}}, 0, 0, \frac{1}{\sqrt{3}}e^{i\theta})^\top$
$-\text{V}_0$	$S e^{i\frac{\theta}{3}} e^{-i\frac{2\theta}{3} \frac{(-f_x-f_y-f_z)}{\sqrt{3}}}$	$(0, \sqrt{\frac{2}{3}}e^{i\theta}, 0, 0, \frac{1}{\sqrt{3}}e^{-i\theta})^\top$
$-\text{VI}_0$	$S e^{-i\frac{\theta}{3}} e^{-i\frac{\theta}{3} \frac{(-f_x-f_y-f_z)}{\sqrt{3}}}$	$(0, \sqrt{\frac{2}{3}}, 0, 0, \frac{1}{\sqrt{3}}e^{-i\theta})^\top$
$\text{VII}_0$	$S e^{-i\frac{\theta}{3}} e^{-i\frac{\theta}{3} \frac{(-f_x-f_y-f_z)}{\sqrt{3}}}$	$(0, \sqrt{\frac{2}{3}}e^{-i\theta}, 0, 0, \frac{1}{\sqrt{3}}e^{i\theta})^\top$

a class specific constant  $a_X$ . The superscript  $\nu$  defines the axis of the  $\sigma_\nu$  Pauli matrix generator of the class specific SU(2) rotation  $g_X^\nu$ , while the sign in  $g_X^\nu$  is determined explicitly by the sign of the label. Example labels for the cyclic-tetrahedral phase vortices are  $\text{III}_0^x = (0, i\sigma_x)$ ,  $\text{IV}_0 = (1/3, \tilde{\sigma})$  and  $-\text{VI}_0^x = (-1/3, -i\sigma_x \tilde{\sigma}^2)$ . By the decomposition of the spin rotation  $g_\nu^X = \mathbf{1} \cos(\Theta_X/2) + i(\boldsymbol{\omega} \cdot \boldsymbol{\sigma}) \sin(\Theta_X/2)$ , the charges can be mapped onto the R transformations, written in the form  $R = e^{i\phi} e^{-i\Theta\boldsymbol{\omega} \cdot \mathbf{F}}$ , where  $\Theta$  is a spin rotation angle about an axis  $\boldsymbol{\omega}$  and  $\mathbf{F}$  is the spin density vector, as  $R(\pm X_\eta^\nu) = e^{i2\pi(\eta+a_X)} e^{-i\mathbf{f} \cdot \boldsymbol{\omega} \Theta_X}$ .

The 24 lowest energy vortices, as fixed by the U(1) winding number, are represented in Fig. 2.4 using the spherical harmonic decomposition of the order parameter to display their characteristic rotations. In Table. 2.1, we provide explicit order parameters for a representative set of these 24 vortices. For these order parameters we can characterise the vortex core structures which are either  $|A| \neq 0$ , classes (II)-(III), or  $|F_z| \neq 0$ , classes (IV)-(VII). Although, in general, the core structure will depend on the values of the spin interaction parameters.

$I_0$		$I_0$
$-II_0$		$-II_0$
$III_0^x$		$-III_0^x$
$III_0^y$		$-III_0^y$
$III_0^z$		$-III_0^z$
$IV_0$		$-VI_{-1}$
$-IV_0^x$		$-VI_{-1}^y$
$-IV_0^y$		$-VI_{-1}^z$
$-IV_0^z$		$-VI_{-1}^x$
$-V_0$		$VII_{-1}$
$V_0^x$		$VII_{-1}^y$
$V_0^y$		$VII_{-1}^z$
$V_0^z$		$VII_{-1}^x$

**Figure 2.4:** Order parameter transformations of the lowest energy cyclic-tetrahedral phase vortices. For each vortex, the cyclic-tetrahedral phase order parameter is discretely sampled at multiple points along a path enclosing the vortex core and represented using the spherical harmonic decomposition. Order parameter traverses left (right) to right (left) for labels on the left (right). The background colour of the vortex labels denotes the equivalency classes. See Appendix B for a view of the rotations down the axis of the sequence.

The interest in non-Abelian vortices stems from their non-commuting topological charges. The composition of two charges is given by the group operation  $(\pm X_\eta^\alpha)(\pm Y_\nu^\beta) = (\eta + a_X + \nu + a_Y, g_X^\alpha g_Y^\beta)$ , which homotopically is equivalent to successively traversing the paths  $\Psi_X(\Gamma_X)$  and  $\Psi_Y(\Gamma_Y)$  enclosing each vortex. We can see the non-commutativity for example with  $(-IV_0^x)(-VI_0^z) = (III_0^z)$  which when reversed gives  $(-VI_0^z)(-IV_0^x) = (-III_0^x)$ . Physically, the non-Abelian algebra results in novel non-trivial topological interactions when vortices collide or are braided around each other. These interactions have fascinating implications for new types of quantum turbulence and topological quantum information processing and storage, concepts which we will explore further in the following sections and chapters.

## 2.6. Vortex collision dynamics

Vortices in an infinite uniform superfluid move with the local superfluid velocity<sup>8</sup>. Thus, the motion of the vortices is driven by the interactions between their mutual velocity fields. In the vortex filament model, the dynamics of  $N_v$  infinitely thin vortex lines are determined from the superfluid velocity field calculated from the Biot–Savart expression

$$\mathbf{v}(\mathbf{r}) = \frac{\omega}{4\pi} \sum_i^{N_v} \int_{\mathcal{L}_i} \frac{(\mathbf{r} - \mathbf{r}') \times d\mathbf{r}'}{|\mathbf{r} - \mathbf{r}'|^3}, \quad (2.29)$$

which consists of an integral over the points  $\mathbf{r}'$  on each vortex line  $\mathcal{L}_i$  in the system. As the vortex line is free to contort away from the axially aligned orientation, the velocity field also accounts for the complicated self-interactions of the vortex lines. Such self-interactions may excite Kelvin waves [163], helical waves which propagate along the vortex line with a frequency given by the dispersion relation [164]

$$\omega(k) \approx \frac{\hbar k^2}{2M} \log \left( \frac{1}{|k\xi|} \right), \quad (2.30)$$

where  $k = 2\pi/\lambda$  is the wavenumber for a wavelength  $\lambda$ . During their motion, two vortices may collide and interact in a manner which can alter the local topology of the system. Compared with the GPE, topology is not modelled in the vortex filament model and vortex collisions must be inserted by hand into the dynamics encompassed by Eq. (2.29).

---

<sup>8</sup>In non-uniform or finite systems the motion of the vortices is additionally affected by any boundaries or density gradients in the system. [162]

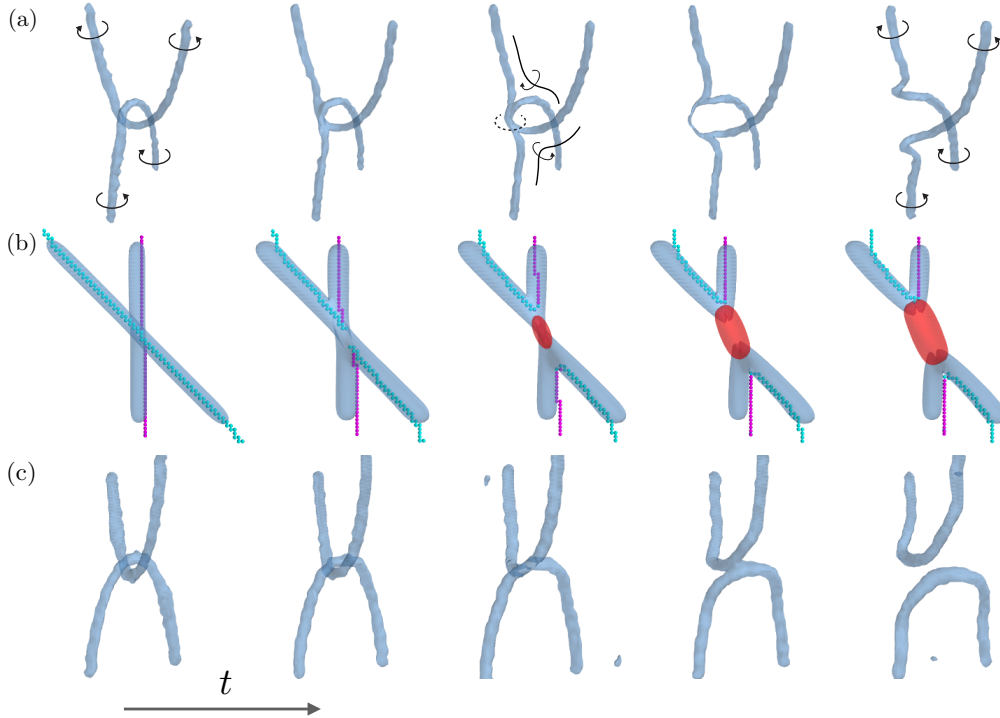


**Figure 2.5:** Results of numerical GPE experiments detailing the different collision dynamics of cyclic-tetrahedral phase spinor vortex lines. (a) Reconnection event. The direction of the circulation of each vortex is given by the arrows. The dotted circle denotes a local cancellation of the circulation. (b) Rung formation event. The cyan and magenta dots mark the locations of the two non-Abelian vortices. The red structure is the rung vortex. (c) Pass through event. Data is presented as isosurfaces of  $|F_z|^2$  (blue surface) and  $|A|^2$  (red surface) which trace the vortex cores.

A collision may result in one of three outcomes; a reconnection; the formation of a rung vortex; or a pass through, depending on the topology and kinematics of the vortex lines. In Fig. 2.5 we show the results of numerical GPE simulations detailing each of these collision events for fractional-charge vortex lines in the cyclic-tetrahedral superfluid phase of a uniform spin-2 condensate.

For scalar vortices, the dominant collision event is a reconnection [92, 93], an example of which is shown in Fig. 2.5(a). During a reconnection two segments of vortex line, with opposing circulations, approach and connect at a cusp which annihilates by exchanging the tails of each vortex. The energy released during the collision excites Kelvin waves and the emission of sound in the form of density waves [100]. Vortex reconnections and Kelvin waves have been directly observed experimentally in superfluid Helium [49, 50] and more recently in a trapped BEC [165, 166].

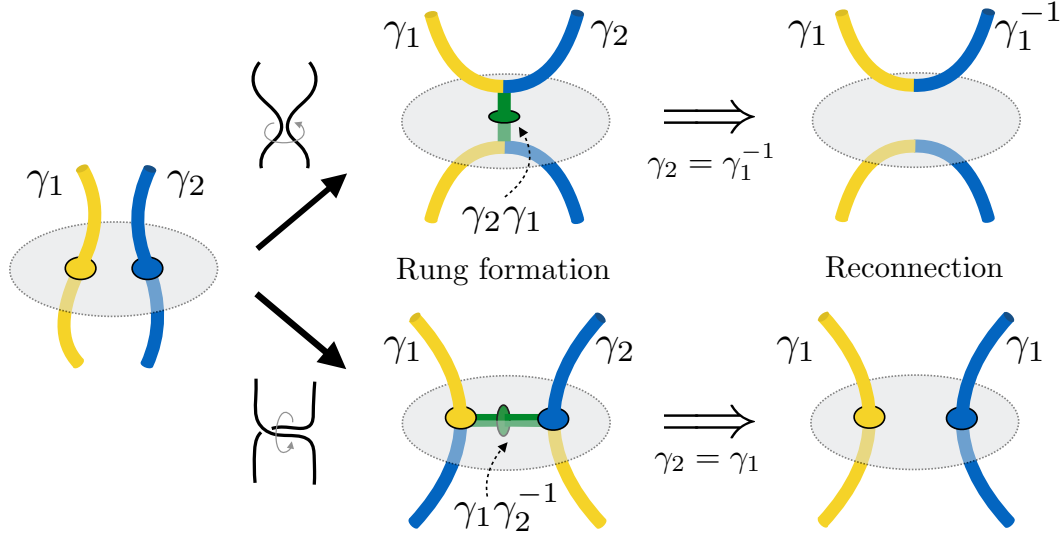


**Figure 2.6:** Schematic of collision dynamics of three-dimensional vortex lines. Left: Initial state of vortex lines, with charges  $\gamma_1$  and  $\gamma_2$ , intersecting a two-dimensional condensate plane, grey-shaded disk, which intersects the collision cusp. Top and bottom rows correspond to the two vortex collision geometries. Middle top: Vortices collide to form a rung vortex  $\gamma_2\gamma_1$ . Right top: When  $\gamma_2 = \gamma_1^{-1}$  the rung annihilates and a reconnection occurs. Middle bottom: The  $\gamma_2$  vortex line bends such that the collision forms the rung  $\gamma_1\gamma_2^{-1}$ . Right bottom: When  $\gamma_2 = \gamma_1$  the rung annihilates and a reconnection occurs.

In general the collision outcome is constrained to preserve the total topological charge of the two vortices at the collision cusp, equivalent to the group operation of their individual charges. Hence, the collision outcomes are highly dependent on the algebra of the vortex charges. However, certain topologically permitted interactions may be energetically suppressed by the kinematics of the vortices. For the scalar vortices with  $\pi_1(S^1) = \mathbb{Z}$ , the topological charges are integers and the group operation is addition. As the charges commute under addition the scalar vortices are Abelian. A scalar vortex pair, axially aligned with the  $z$  axis, collides such that the topological charge of the cusp is  $\gamma_2\gamma_1$ , see top row of schematic in Fig. 2.6. In the reconnection described above, the vortices have opposite circulation and the charge of the cusp is trivial  $\gamma_2\gamma_1 = \gamma_1\gamma_1^{-1} = 1 + -1 = 0$ . In comparison, for a vortex-vortex pair the charges add,  $\gamma_2\gamma_1 = \gamma_1\gamma_1 = 1 + 1 = 2$ . As a result, the vortices would coalesce into a multiply charged rung vortex, which is drawn out as a bridge between the colliding vortices [55, 167]. However, while rung formation is topologically permitted for scalar vortices, the Coulomb-like repulsive interaction between the mutual velocity field of the vortices induces an energetic barrier which inhibits a collision. Instead, at low collision velocities, the vortices prefer to locally re-orientate so that their initially parallel circulations become anti-aligned, see bottom row in Fig. 2.6.

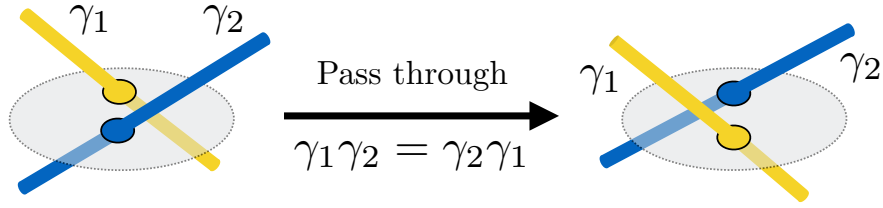


**Figure 2.7:** Schematic of pass through of Abelian vortex lines.

As such, the charge at the collision cusp becomes  $\gamma_1\gamma_2^{-1} = \gamma_1\gamma_1^{-1} = 1 + -1$ , and a reconnection occurs instead.

For the cyclic-tetrahedral phase, and other non-Abelian phases, we may have vortex pairs with either commuting or non-commuting topological charges. The algebra of the charges has a marked effect on the possible collision dynamics. Abelian vortex pairs have similar collision dynamics to the scalar vortices. A collision of a vortex with its antivortex results in a reconnection. Similarly, for vortices with same charge, a reconnection will preferentially occur following a local reorientation of the vortex lines. Unlike the scalar vortices, it is also energetically possible for Abelian spinor vortices to pass directly through each other without any apparent interaction. Pass through is only possible for Abelian vortices as the topology, in terms of the total topological charge, does not change throughout the collision, see Fig. 2.7. Under unusual energetic circumstances, a rung might form during a collision of Abelian vortices. Comparatively, non-Abelian vortex pairs are topologically constrained to only undergo rung formation [88, 91], as the algebra of the vortex charges cannot be altered by rotations of the constituent vortex lines. The rung formed from the collision may have charge  $\gamma_2\gamma_1$  or  $\gamma_1\gamma_2^{-1}$ , depending on the geometry of the collision, see top and bottom rows of Fig. 2.6, respectively.

In this thesis we focus on the topological interactions of 2D vortices. Two-dimensional condensates may be achieved experimentally by tightly confining the condensate along one axis. As a result the dynamics of the vortex line are constrained and vortices behave effectively as point-like objects [168], with their collision dynamics changing accordingly. In Chapter 4 we will thoroughly explore the collision dynamics of vortices in two-dimensional condensates and present our results for the collisions of two-dimensional fractional-charge vortices in the cyclic-tetrahedral phase of a spin-2 BEC.

In the following Chapters we will tease out the important role vortex collisions play in quantum turbulence and how they act as a signifying property of non-Abelian vortex anyons.

## 2.7. Topological influence

There exists a long range topological interaction between non-Abelian vortices in the form of a topological influence, the effect of which is a change in the topological charges of adiabatically exchanged (braided) vortices [42, 98]. The topological influence depends only on topology and has been previously explored for topological excitations in a variety of condensed matter systems [169] including liquid crystals [170], cosmic strings [134] and discrete gauge theories [44, 45].

Consider two vortices with topological charges  $\gamma_1$  and  $\gamma_2$ , defined according to the loops in the top row of Fig. 2.8(a). By convention we will choose to measure the topological charges by traversing the paths counter-clockwise (traversing clockwise would correspond to the inverse charge). The total topological charge, obtained from the path enclosing both vortices, is initially  $\gamma_{\text{tot}} = \gamma_2 \gamma_1$ . Smoothly exchanging (braiding)  $\gamma_1$

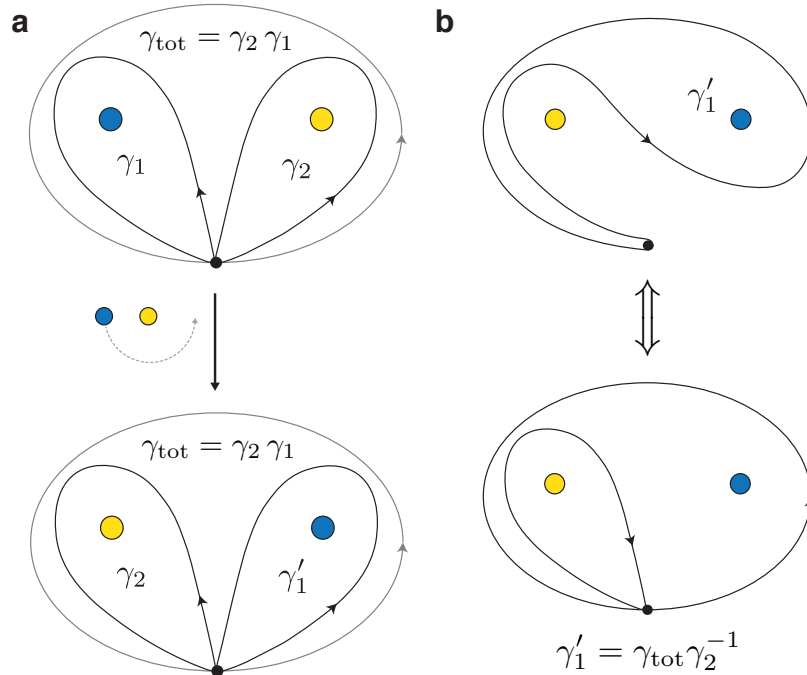


**Figure 2.8:** Topological influence of non-Abelian vortices. **a**, Counter-clockwise exchange of two vortices, denoted by the blue and yellow circles, respectively. Each loop defines a charge. All such loops begin at a base point, denoted by the black circular marker, and encircle either a vortex or vortices in a counter-clockwise sense. Prior to the exchange the blue and yellow vortices have charges  $\gamma_1$  and  $\gamma_2$ , respectively. The loop around both vortices defines the total charge  $\gamma_{\text{tot}} = \gamma_2 \gamma_1$ . After the exchange the blue vortex has a new charge  $\gamma'_1$ . **b**, The path corresponding to the flux  $\gamma'_1$ , top row, can be decomposed into the combined paths  $\gamma'_1 = \gamma_{\text{tot}} \gamma_2^{-1}$ , in the bottom row.

anticlockwise about  $\gamma_2$ , resulting in the configuration in the bottom row of Fig. 2.8(a), enacts a topological influence which changes the charge  $\gamma_1$  to  $\gamma'_1$  while preserving  $\gamma_2$ . In a BEC the total topological charge is conserved, implying  $\gamma_{\text{tot}} = \gamma_2\gamma_1 = \gamma'_1\gamma_2$ . Hence,  $\gamma_1$  transforms to  $\gamma'_1 = \gamma_{\text{tot}}\gamma_2^{-1} = \gamma_2\gamma_1\gamma_2^{-1}$  corresponding to the path in Fig. 2.8(b). This transformation is called a conjugation of  $\gamma_1$  by  $\gamma_2$ . In total, the mutual topological influence during a counter-clockwise elementary braid (exchange of a pair) of vortices  $(\gamma_1, \gamma_2)$  converts the charges to  $(\gamma_2, \gamma_2\gamma_1\gamma_2^{-1})$ . If  $\gamma_1$  and  $\gamma_2$  do not commute, this mapping permutes the charge of the second vortex within its associated equivalency class according to the equivalency relation. The topological influence also depends on the direction in which the vortices are exchanged. Hence, the clockwise exchange realises the map  $(\gamma_1, \gamma_2) \rightarrow (\gamma_1^{-1}\gamma_2\gamma_1, \gamma_2)$ . The topological influence really occurs as soon as the spatial order of the vortices is reversed. This corresponds to the point in the braid when each vortex crosses over an imaginary line extending vertically from its counterpart.

In Chapter 5, we perform numerical experiments to braid non-Abelian vortices and demonstrate the non-trivial topological influence. We will see that the topological influence and collision dynamics of non-Abelian vortices provide the essential characteristics of non-Abelian anyons.

## 2.8. Non-Abelian anyons

All elementary particles are classified by their quantum statistics as either bosons or fermions. However, the quantum statistics of particles in a system constrained to two spatial dimensions are notably different. Consider twice braiding two such particles, corresponding to winding one particle about another and returning the particle to its starting point. In 3D, this path can be lifted over the other particle and contracted to a point, see Fig. 2.1. Comparatively, As shown in Fig. 2.9, in 2D this path can not be smoothly deformed to a point without passing through the other particle. Hence, after the exchange, the two-particle system does not necessarily return to the same state, as occurs in 3D. In the simplest case, the system's wave function is multiplied by an arbitrary geometric phase factor,  $e^{i\theta}$ , which is not restricted to the specific values corresponding to bosons ( $\theta = 0$ ) or fermions ( $\theta = \pi$ ). These particle-like excitations are called anyons and are neither bosons or fermions. Anyons were first predicted to emerge in certain two-dimensional materials by Leinaas and Myrheim [26] and Wilczek [27].

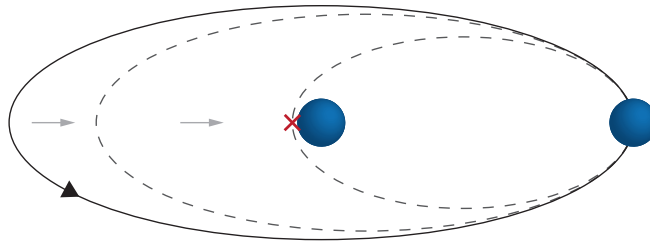


**Figure 2.9:** Two elementary particles (blue spheres) are adiabatically exchanged twice in two spatial dimensions. The exchange path can not be smoothly deformed to a single point demonstrating the topologically non-trivial nature of exchanges in two dimensions.

The interesting physics of anyons are realised by braiding and subsequently fusing  $N$  particles [25,31,33,171,172]. We shall imagine the particles arranged on a line. Exchanging anyons can be pictured as a braid of their (2+1) dimensional space-time/world lines. Group theoretically, such braids correspond to the elements of the braid group  $B_N$  acting on  $N$  lines. In general, the elementary counter-clockwise exchange of the  $i$ th and  $(i+1)$ th line is denoted by the group element  $\sigma_i$ , while its inverse  $\sigma_i^{-1}$  corresponds to a clockwise exchange. In the case of  $B_3$ , acting on three lines, the elementary braids are shown in the braid diagrams in Fig. 2.10(a). A product of elementary braids is given by the concatenation of the corresponding braid diagrams with the first element in the product at the bottom and subsequent terms added on top, see Fig. 2.10(b). For the simplest anyons each braid contributes a phase to the many-particle wave function. As the phases commute, these are denoted Abelian anyons and the order of the braiding operations is unimportant. There are also non-Abelian anyons characterised by non-Abelian braiding statistics where the exchange phase may be expressed as a non-commutative matrix, specifically a unitary operator, see Fig. 2.10(b). A particular state of  $N$  non-Abelian anyons is just one element of a Hilbert space of degenerate ground states. The unitary operator realised by the braiding may transform between these degenerate states. In fact, at low energies the states are topologically protected such that braiding is the only means to transform between different elements of the Hilbert space.

An anyon model has three essential aspects; (1) a list of particle types; (2) a set of fusion rules that determine the types of particles formed after bringing together two such particles; and (3) braiding rules that describe the effect of exchanging the positions of two particles. As a way of example, let us consider the Fibonacci anyon model [31, 171–173], one of the simplest and richest non-Abelian anyon models. The Fibonacci anyon model contains two particles; the vacuum  $\mathbf{1}$  and a particle  $\tau$ . When two particles in a model are brought together they may form a composite particle corresponding to another anyon

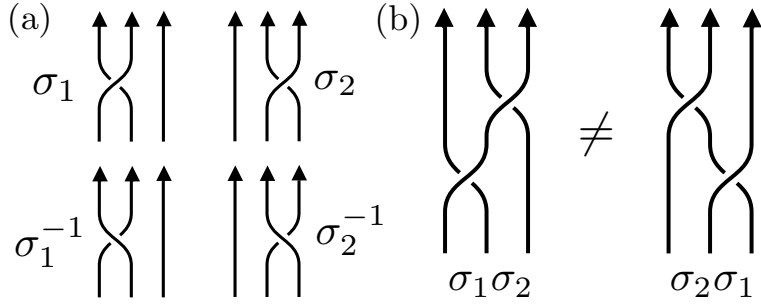


**Figure 2.10:** Braid diagram representation of the group  $B_3$ . (a) The elementary braids  $\sigma_1$ ,  $\sigma_2$  and their inverses acting on the space-time world lines of three anyons. The arrowheads denote the direction of time. (b) Concatenation of elementary braids to form a longer braid diagram. For non-Abelian anyons the result of the braid is order dependent.

type in the model. The result of fusing two anyons, with labels  $a$  and  $b$ , is given by a fusion rule,

$$a \otimes b = \sum_c N_{ab}^c c, \quad (2.31)$$

where the sum is over the anyon labels of all possible fusion outcomes. Here, the symbol  $\otimes$  simply refers to a composition of anyons rather than a direct product of vector spaces. Similarly, the sum can be expanded using  $\oplus$  symbols to give the explicit label set of the anyons formed from the fusion. The fusion rules are symmetric. i.e.  $a \otimes b = b \otimes a$ . The multiplicity,  $N_{ab}^c$ , states how many distinguishable ways a particular  $c$  anyon can be formed from the fusion of  $a$  and  $b$  anyons. For Abelian anyons, the fusion may result in a single outcome with multiplicity  $N_{ab}^c = 1$ . Comparatively, non-Abelian anyons have multiple fusion channels. A fusion may result in either multiple different  $c$  particles, each with multiplicities  $N_{ab}^c \neq 0$ , or in a single particle formed  $N_{ab}^c \geq 2$  different ways. For the Fibonacci model, the vacuum is Abelian with fusion rules  $\mathbf{1} \otimes \mathbf{1} = \mathbf{1}$  and  $\mathbf{1} \otimes \tau = \tau$ . The non-Abelian anyon is  $\tau$ , with fusion rule  $\tau \otimes \tau = \mathbf{1} \oplus \tau$ . Hence,  $\tau$  is its own antiparticle. The  $N_{ab}^c$  distinguishable ways that an anyon  $c$  can be formed from the fusion of anyons  $a$  and  $b$  can be considered as orthonormal basis states of a Hilbert space  $V_{ab}^c$ . The Hilbert space is alternatively called the fusion space and we shall denote the basis states as fusion paths.

The multiple fusion outcomes of a pair of non-Abelian anyons accounts for the different degenerate ground states of  $N$  such particles. Consider the  $N$  anyons with labels  $a_1, a_2, a_3, \dots, a_n$  arranged in a line. The anyons are successively fused from left to right, where  $a_3$  fuses with the outcome of fusing  $a_1$  and  $a_2$ , and so on down the line. As each

fusion has multiple different outcomes, the result is a branching tree of multiple different fusion paths. The associated fusion space is

$$V_{a_1 a_2 a_3 \dots a_n}^c = \bigoplus_{b_1, b_2, b_3, \dots, b_{n-2}} V_{a_1 a_2}^{b_1} \otimes V_{b_1 a_3}^{b_2} \otimes V_{b_2 a_4}^{b_3} \otimes \dots \otimes V_{b_{n-2} a_n}^c, \quad (2.32)$$

where  $\bigoplus$  is a sum over all the different fusion outcomes. The dimension of the fusion space,

$$\text{Dim}(V_{a_1 a_2 a_3 \dots a_n}^c) = \sum_{b_1, b_2, b_3, \dots, b_{n-2}} N_{a_1 a_2}^{b_1} N_{b_1 a_3}^{b_2} N_{b_2 a_4}^{b_3} \dots N_{b_{n-2} a_n}^c \propto d_a^N, \quad (2.33)$$

grows exponentially with  $N$ , the number of anyons. The growth in the dimension of the fusion space as new anyons are added to the system is determined by the quantum dimension  $d_a$  of the  $a$  anyon. The quantum dimension can be shown to satisfy the relation

$$d_a d_b = \sum_c N_{ab}^c d_c, \quad (2.34)$$

derived from the fusion rule in Eq. (2.31). Similarly, the quantum dimension is closely linked with the probability of the different fusion outcomes. The probability of anyons  $a$  and  $b$  fusing to  $c$  is given by

$$\text{Pr}(ab \rightarrow c) = \frac{N_{ab}^c d_c}{d_a d_b}. \quad (2.35)$$

In Fig. 2.11 we provide the fusion tree diagram for the fusion of  $N$   $\tau$  Fibonacci anyons. The 1st anyon on the left is fused with its neighbour, leading to two possible outcomes - annihilation to the vacuum or another  $\tau$  anyon, with respective probabilities of  $\approx 0.38$  and  $\approx 0.62$ . The process then continues, with the next leftmost  $\tau$  anyon, fusing with either the 1 or  $\tau$  anyons, and so on. The number of paths from the fusion of  $N$   $\tau$  anyons,  $N_n = \text{Dim}(V_{\tau^n}^c)$ , follows the Fibonacci series, as per the name, with the recursion relation  $N_n = N_{n-1} + N_{n-2}$ . Thus the dimension of the Hilbert space grows as  $N_n \propto \varphi^N$ , where the quantum dimension  $d_\tau = \varphi$  is the golden ratio  $\varphi = (1 + \sqrt{5})/2$ . This can also be calculated directly from the relation  $d_\tau^2 = d_1 + d_\tau$ , derived from Eq. (2.34). Braiding anyons in the configuration enacts a unitary operator on the Hilbert space, transforming between the different fusion paths. The braiding rules are determined from the  $F$  and  $R$ -matrices. These matrices define sets of transformations which describe isomorphisms between fusion spaces. The  $F$ , or fusion, matrix relates fusion spaces  $V_{a_1 a_2 a_3}^c \cong \bigoplus_b V_{a_1 a_2}^b V_{b a_3}^c \cong \bigoplus_e V_{a_2 a_3}^e V_{e a_1}^c$ , where the order in which the anyons are fused

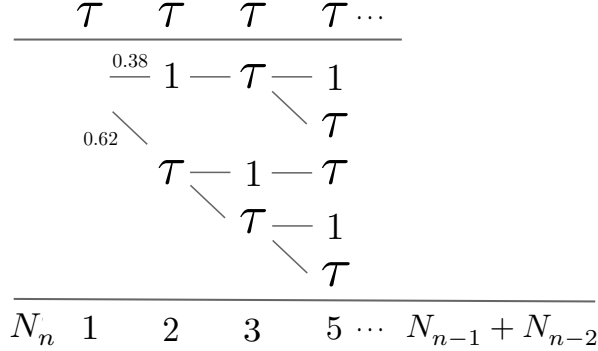


**Figure 2.11:** Fusion tree diagram of the Fibonacci anyon model. Top: The sequence of  $\tau$  anyons to be fused. Middle: The tree of fusion paths up to the 4th  $\tau$  anyon. We also provide the probabilities for the outcomes of the  $\tau \otimes \tau$  and  $\mathbf{1} \otimes \tau$  fusion rules. Bottom: Number of fusion paths  $N_n$  after the fusion of the  $n$ th anyon. The numbers follow the Fibonacci recursion relation.

is changed, introducing different intermediate fusion outcomes. Similarly, the  $R$ , or braid, matrix allows us to transform between fusion spaces related by the exchange operator  $B : V_{ab}^c \rightarrow V_{ba}^c$ . The  $R$  and  $F$ -matrices are fixed by consistency relations called the pentagon and hexagon equations. The details of how to solve the relations for the Fibonacci anyon models can be found in Refs. [31, 171, 173]. The  $R$ -matrix describing the exchange of two  $\tau$  anyons is,

$$R_{\tau\tau} = \begin{pmatrix} e^{4\pi i/5} & 0 \\ 0 & -e^{2\pi i/5} \end{pmatrix}, \quad (2.36)$$

where the terms  $R_{\tau\tau}^{\mathbf{1}} = e^{4\pi i/5}$  and  $R_{\tau\tau}^{\tau} = -e^{2\pi i/5}$  are the phase accumulate after the exchange of two  $\tau$  anyons fusing to  $\mathbf{1}$  and  $\tau$ , respectively. The  $F$ -matrix,  $F_{\tau\tau\tau}^{\tau}$ , given by

$$F_{\tau\tau\tau}^{\tau} = \begin{pmatrix} \varphi^{-1} & \varphi^{-1/2} \\ \varphi^{-1/2} & -\varphi^{-1} \end{pmatrix}, \quad (2.37)$$

transforms between the two fusion spaces corresponding to the two different ways three  $\tau$  anyons can be fused to  $\tau$ .

How anyons fuse when brought together depends on the history of their paths prior to the fusion. Encoding information in the non-local fusion properties of non-Abelian anyons forms a tantalising prospect for realisation of a fault-tolerant universal quantum computer [28, 29].

## 2.9. Topological quantum computing

The path to topological quantum computing advances concurrently with research on non-Abelian anyons. The procedure for quantum computing involves three steps [9]; (1) initialise the computer in a known state  $|\Psi_i\rangle$  of the systems Hilbert space; (2) evolve the system according to some unitary operator which obtains the desired final state  $|\Psi_f\rangle = U(t)|\Psi_i\rangle$ ; (3) read the output of the computer by making a measurement of the final state. Repeating this procedure a great many times builds a statistical solution to the problem. The typical elementary building blocks of a quantum computer are qubits based on ‘two-level’ systems, i.e. systems described by a two dimensional Hilbert space. While classical bits in a digital computer are either 0’s or 1’s, a qubit can be in the state zero  $|0\rangle$  or  $|1\rangle$ , or one of infinitely many superposition states  $\alpha|0\rangle + \beta|1\rangle$ , where  $\alpha, \beta \in \mathbb{C}$ . A system of  $N$  qubits is described by a Hilbert space with  $2^N$  basis vectors, each which is a possible computational state of the computer. Through unitary evolution these computational states can superposed or entangled, equivalent to a quantum state which can not be expressed as a product of the qubit states. Entangled qubits must be considered apart of an inseparable whole, such that measuring the state of one qubit determines the state of all others. The capacity to realise superposition and entangled states in a quantum computer is the resource that promises the potential for computational power beyond the reach of digital computers.

Qubits have been realised in a variety of systems, including trapped ions [18–20], spins in silicon atoms [21] and superconducting circuits [22]. While progress has been made towards realising quantum supremacy<sup>9</sup> in these systems [175–179], they remain sensitive to the accumulation of errors. For example, errors can occur in the information storage of a quantum computer through decoherence, which causes entanglement between the state of the computer and its environment. Since the state of the environment cannot be measured accurately, information of the system is lost. While error correction can be performed [173, 180, 181], it becomes computationally costly.

An intrinsically fault-tolerant quantum computer could be built from topological qubits based on configurations of non-Abelian anyons in a spatially 2D system [25, 29, 33, 182]. In these topological quantum computers, information is encoded non-locally in the topological properties of the system, namely the fusion outcomes of the anyons. The associated Hilbert space grows exponentially with increasing number of anyons, see

---

<sup>9</sup>Quantum supremacy refers to a demonstrated speed up of some quantum algorithm relative to a digital computer [174].

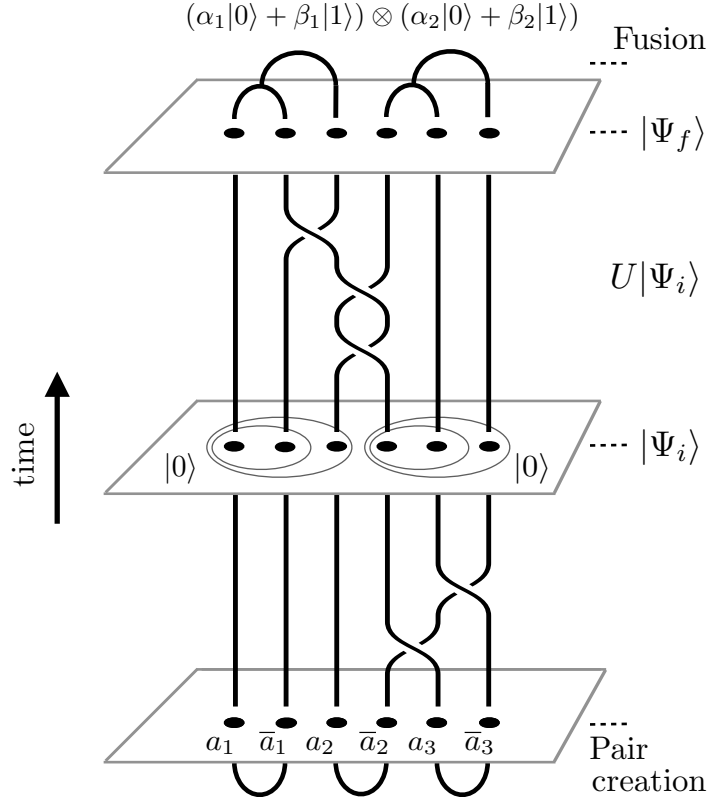


**Figure 2.12:** A schematic of a topological quantum computation. Time flows up the page. The computer is initialised by pair creating anyons (black dots) from the vacuum, represented as the cusps in the anyon worldlines. The anyons are labelled  $a_i$ , where  $a$  denotes the type,  $i$  the pair number counting from left to right, and  $\bar{a}$  is an antiparticle. The anyon  $a_2$  is trivially braided with the pair  $a_3, \bar{a}_3$  to form the initial state  $|\Psi_i\rangle$  configured as two  $|0\rangle$  qubits of three anyons each. A unitary operation  $U$  is applied to the initial state as a braid in the anyon worldlines, producing the final state  $|\Psi_f\rangle = U|\Psi_i\rangle$ . The knot tied in the worldlines physically ‘entangles’ the two qubits. The final state is measured by fusing the anyons giving the superposition  $(\alpha_1|0\rangle + \beta_1|1\rangle) \otimes (\alpha_2|0\rangle + \beta_2|1\rangle)$ .

Eq. (2.33), permitting a great number of computational states which can be entangled. To unitarily evolve between states in the Hilbert space requires a non-local transformation to the system realised by braiding the anyons. Therefore, the state of a topological quantum computer is topologically protected from the types of local perturbations to the system that result in decoherence in non-topological quantum computers.

The procedure for performing topological quantum computations is shown in the schematic Fig. 2.12. The configuration of particles  $\{a_1, \bar{a}_1, a_2, \bar{a}_2, a_3, \bar{a}_3\}$ , where  $\bar{a}$  is the antiparticle of the anyon type  $a$ , is initialised via pair creation and arranged into  $|0\rangle$  qubits, forming the initial state  $|\Psi_i\rangle$ . A unitary operation  $U$ , which realises the final state  $|\Psi_f\rangle = U|\Psi_i\rangle$ , is performed by dragging the anyons around each other to braid a

topologically non-trivial knot in their worldlines. Since the unitary operation depends only on the topology of the knot, which is contained entirely in the crossings, the outcome of the braid is insensitive to any small wiggles in the paths. Strictly speaking, the braid is an approximation to the desired unitary operation with the accuracy typically increasing for variants containing more elementary braids [183, 184]. Finally, a measurement of the state is made by dragging the anyons together and fusing them.

Errors may still arise in a topological quantum computer in the form of processes which alter the topology of the knot representing the unitary operation [25]. For example, if two of the initialised anyons stray too close they may fuse, effectively cutting the knot. Furthermore, thermal fluctuations may result in the pair creation of spurious anyons, so called quasiparticle poisoning [32]. If one of the spurious anyons braids with an initialised anyon and then re-fuses with its pair, the effect is to entwine the unitary knot with the knot formed from the worldlines of the spurious anyons, thereby creating a topologically non-trivial link<sup>10</sup>.

Not all anyon models are suitable for topological quantum computing. A universal topological quantum computer is realised for anyon models where the braiding statistics are such that any unitary operation can be approximated with arbitrary accuracy with braiding alone [25, 185–187]. This implies a minimum set of unitary operations from which any other may be generated, for example the set might be, collectively, the single qubit braids and a two-qubit braid like the controlled-NOT (CNOT) operation. A sequence of braids that approximates the CNOT operation has been demonstrated for the Fibonacci anyon model [183, 188, 189], and thus the Fibonacci anyons are capable of universal topological quantum computing.

As a concrete example let us consider topological quantum computing with Fibonacci anyons. The fusion space,  $V_{\tau\tau\tau}^\tau$ , has dimension  $\text{Dim}(V_{\tau\tau\tau}^\tau) = 2$  corresponding to the two fusion paths ending in  $\tau$  after fusing three  $\tau$  anyons in Fig. 2.11. Hence, a qubit can be constructed from three  $\tau$  anyons, where the two states are  $|0\rangle = |((\bullet, \bullet)_1, \bullet)_\tau\rangle$  and  $|1\rangle = |((\bullet, \bullet)_\tau, \bullet)_\tau\rangle$ . The notation represents the fusion path of the  $\tau$  anyons, labelled by the circular markers, with the outcome of fusing the anyons that are enclosed by the parentheses denoted by the adjacent subscript. The remaining fusion path  $|N\rangle = |((\bullet, \bullet)_\tau, \bullet)_1\rangle$ , is a non-computational state which is unreachable from any of the computational states by only braiding the three anyons. Braids on a single qubit are

<sup>10</sup>A link is formed from entwined but non-intersecting knots, for example the Olympic rings.

given by the elements of the braid group  $B_3$

$$\begin{aligned}\rho(\sigma_1) &= R_{\tau\tau}^\tau = \begin{pmatrix} e^{4\pi i/5} & 0 \\ 0 & -e^{2\pi i/5} \end{pmatrix}, \\ \rho(\sigma_2) &= (F_{\tau\tau\tau}^\tau)^{-1} R_{\tau\tau}^\tau F_{\tau\tau\tau}^\tau = \begin{pmatrix} -e^{-\pi i/5} & -\frac{e^{-\pi i/10}}{\sqrt{\varphi}} \\ -\frac{e^{-\pi i/10}}{\sqrt{\varphi}} & -\frac{1}{\varphi} \end{pmatrix},\end{aligned}\tag{2.38}$$

where we have used Eq. (2.36)-(2.37) and omitted the action of the braid on the state  $|N\rangle$  to obtain the  $2 \times 2$  matrices. Braiding on two qubits introduces a further error in the form of ‘leakage’ into the non-computational states, i.e. a braid can result in a superposition  $\alpha|0\rangle + \beta|1\rangle + \gamma|N\rangle$ . However, it is possible to design braids such that the leakage is minimised.

The inherent topological protection offered by non-Abelian anyons makes topological quantum computers a very appealing platform for topological information storage and processing. As such non-Abelian anyons are in great demand and are being intensively searched for. In Chapter 5, we present results indicating the potential existence of non-Abelian anyons in the form of non-Abelian vortex types in spinor Bose–Einstein condensates. Furthermore, we outline a possible qubit for the non-Abelian anyons and numerically perform controlled unitary operations on one- and two-qubit states.

## Chapter 3.

# Numerical implementation

In the previous chapter, we provided the theory framework for understanding non-Abelian vortices in spin-2 Bose–Einstein condensates. Here we discuss the computational practicalities for numerically simulating a two-dimensional spin-2 BEC in the cyclic-tetrahedral superfluid phase. Where practical, our simulations are informed by experiment. Spin-2 BECs have thus far been experimentally realised using  $^{87}\text{Rb}$  atoms, as such our numerical condensate parameters are based on the  $^{87}\text{Rb}$  atom. The scattering lengths of  $^{87}\text{Rb}$  have been measured as  $a_0 = 87.4 \pm 1.0a_{\text{B}}$ ,  $a_2 = 92.4 \pm 1.0a_{\text{B}}$  and  $a_4 = 100.5 \pm 1.0a_{\text{B}}$  [190–192], in units of the Bohr radius  $a_{\text{B}}$ . These values suggest that the condensate lies in the nematic phase, though sufficiently close to the phase boundary that uncertainties do not preclude the experimental realisation of the cyclic-tetrahedral phase but likely only in the presence of vanishing external magnetic fields. Another possible  $F = 2$  atomic species is  $^{23}\text{Na}$  with  $a_0 = 34.9 \pm 1.0a_{\text{B}}$ ,  $a_2 = 45.8 \pm 1.1a_{\text{B}}$  and  $a_4 = 64.5 \pm 1.3a_{\text{B}}$ , which also naturally supports the nematic phase [193]. While Feshbach resonances can be used to alter the value of the spin-independent coupling constant  $c_0$ , similar techniques to tune  $c_1$  and  $c_2$  have not yet been experimentally demonstrated. Thus, present experiments with spinor condensates are limited to superfluid phases accessible in the presence of background magnetic field noise and with the natural scattering lengths of available atomic species. However, it would be pessimistic to assume that techniques to tune  $c_1$  and  $c_2$  could not be realised in the future. Indeed, Spielman *et al.* [194] recently numerically demonstrated the dynamic alteration of the effective interaction strengths of a two-component condensate via weak measurements and their feedback. The measurements do not alter the raw scattering lengths of the condensate but can stabilise spin textures in the system relative to an effective tuned  $c_1$  coupling constant. In this work our focus is on studying the new physics around non-Abelian vortices in spinor condensates. As such, we do not aim to model contemporary experiments. Thus, in our

numerical simulations we are free to choose larger  $c_1$  and  $c_2$  coupling constants which reveal the non-trivial topological properties of non-Abelian superfluid phases, values which may well accord with the parameters available to future experiments. These coupling constants are a theoretically justified choice to ensure that the condensate is deep in the cyclic-tetrahedral phase, hence isolating topological effects of the vortex dynamics from their energetics. Furthermore, the small spin healing lengths associated with this choice of coupling constants allows us to simulate smaller systems with higher resolution. The biaxial nematic phase also hosts non-Abelian vortices and is perhaps a better prospect experimentally, since it may be realised in the presence of an external magnetic field and could potentially be achieved with naturally occurring scattering lengths [91]. However, as the non-Abelian physics is equivalent in both the cyclic-tetrahedral and biaxial nematic phases, we choose to simulate the former phase which does not require increasing the parameter space to account for different external magnetic field strengths.

Using optical potentials it is possible to experimentally realise arbitrary trap geometries [68, 195]. Two dimensional BEC systems are typically achieved in experiments by trapping a three-dimensional gas in a harmonic potential which is tightly confined along one axis, realising a quasi-two-dimensional condensate geometry. However, numerically simulating all three spatial dimensions of a quasi-two-dimensional condensate is computationally burdensome. As we are not aiming for exact quantitative correspondence between our simulations and experiments, we can completely ignore the third spatial dimension and instead simulate a true two-dimensional condensate.

Depending on the algebra of the vortices there are multiple techniques that can be employed to generate fractional-charge vortices in the cyclic-tetrahedral superfluid phase. Huhtamäki *et al.* [196] have shown numerically that a number of the techniques employed for generating vortices in scalar and two-component condensates, can be extended to spin-2 condensates to generate single  $1/3$  fractional vortices or corresponding lattices where all the topological charges commute. These techniques include rotating the trap [197–200], imprinting the vortex phase using Laguerre-Gauss beams [201] and using pulsed microwave and laser fields to transform the population between the spin components [202]. Further to these techniques, in Chapter 6 we demonstrate the controllable generation of lattices of Abelian cyclic-tetrahedral phase vortices via the three-source interference of spin-2 BECs. Imprinting vortices with non-commuting topological charges is more complicated. Borgh *et al.* [91] describe a two-step procedure for imprinting vortex pairs with non-commuting charges. The first vortex is prepared by phase imprinting, then a magnetic field is applied changing the spinor to align with the axis of rotation of the second, which is then

subsequently imprinted. In Sec. 3.2, we describe the numerical procedures employed to create initial states of vortex configurations with either commuting or non-commuting topological charges. These procedures are similar in principle to vortex phase imprinting using Laguerre-Gauss beams.

### 3.1. Gross–Pitaevskii equation for spin-2 Bose–Einstein condensate

The numerical experiments are performed by solving the Gross–Pitaevskii equations, in Eq. (2.17), in non-dimensional form. Simple harmonic oscillator units are used for the numerical calculations

$$t \rightarrow \frac{\tau}{\omega}, \quad r \rightarrow \rho l, \quad E \rightarrow \epsilon \hbar \omega,$$

where  $\tau$  and  $\rho$  are the dimensionless time and space co-ordinates, respectively, and  $\epsilon$  is the dimensionless energy. The angular frequency is given by  $\omega$  and  $l = \sqrt{\hbar/2M\omega}$ . The dimensionless operators for a two-dimensional system are thus

$$\begin{aligned} \psi_m &\rightarrow \frac{\phi_m}{l}, \\ \nabla^2(r) &\rightarrow \frac{\nabla^2(\rho)}{l^2}, \\ \frac{\partial}{\partial t} &\rightarrow \omega \frac{\partial}{\partial \tau}. \end{aligned}$$

The focus of this thesis is two-dimensional condensates. In particular we shall consider pure 2D systems, rather than strictly 3D condensates which have been tightly confined in one dimension. To model a 2D condensate we have to replace the 3D scattering lengths with effective 2D equivalents, the procedure for doing so is described in detail in Ref. [203]. The scattering lengths are reduced in dimension by assuming a condensate in a tight 3D harmonic trap, such that the order parameter is separable as  $\psi(x, y, z) = \psi_{\perp}(x, y)\psi_z(z)$ . The  $z$ -component is then treated independently and described by a wave function with a Gaussian profile and characteristic length scale  $l_z = \sqrt{\hbar/2M\omega_z}$ , where  $\omega_z$  is the angular frequency of the harmonic trap in the  $z$ -direction. Integrating over the  $z$ -direction yields the dimensionless effective 2D scattering lengths  $a_F \rightarrow \frac{\alpha_F l}{l_z}$ . Substituting all the dimensionless quantities into the GPE in Eq. (2.17) we obtain two-dimensional spin-2

Gross–Pitaevskii equations

$$\begin{aligned}
i\frac{\partial\phi_{\pm 2}}{\partial\tau} &= \left(-\nabla^2(\rho) + V_{\text{ext}}(\rho, \tau) + c'_0 n' \pm 2c'_1 F'_z\right) \phi_{\pm 2} \\
&\quad + c'_1 F'_{\pm} \phi_{\pm 1} + \frac{c'_2}{\sqrt{5}} A' \phi_{\mp 2}^*, \\
i\frac{\partial\phi_{\pm 1}}{\partial\tau} &= \left(-\nabla^2(\rho) + V_{\text{ext}}(\rho, \tau) + c'_0 n' \pm c'_1 F'_z\right) \phi_{\pm 1} \\
&\quad + c'_1 \left(\frac{\sqrt{6}}{2} F'_{\mp} \phi_0 + F'_{\pm} \phi_{\pm 2}\right) - \frac{c'_2}{\sqrt{5}} A' \phi_{\mp 1}^*, \\
i\frac{\partial\phi_0}{\partial\tau} &= \left(-\nabla^2(\rho) + V_{\text{ext}}(\rho, \tau) + c'_0 n'\right) \phi_0 \\
&\quad + c'_1 \frac{\sqrt{6}}{2} (F'_+ \phi_1 + F'_- \phi_{-1}) + \frac{c'_2}{\sqrt{5}} A' \phi_0^*,
\end{aligned} \tag{3.1}$$

where we have used the prime notation to denote dimensionless constants and observables. The dimensionless effective coupling constants are  $c'_0 = 8\pi N \sqrt{\omega_z/\omega} (4\alpha_2 + 3\alpha_4)/7$ ,  $c'_1 = 8\pi N \sqrt{\omega_z/\omega} (\alpha_4 - \alpha_2)/7$  and  $c'_2 = 8\pi N \sqrt{\omega_z/\omega} (7\alpha_0 - 10\alpha_2 + 3\alpha_4)/7$ , where we have combined  $N$ , the effective particle number, into the interaction strengths. As discussed in the introduction to this chapter, we simulate a condensate of  $^{87}\text{Rb}$  atoms. However, following Kobayashi *et al.* [88], we choose  $c_1 = c_2 = 0.5 c_0$  in comparison to the typical  $^{87}\text{Rb}$  values of  $c_1 \simeq 0.0103 c_0$  and  $c_2 \simeq -0.0055 c_0$  [192]. The natural spin interaction strengths of  $^{87}\text{Rb}$  place the ground state within the antiferromagnetic superfluid phase, though close to the border with the cyclic-tetrahedral superfluid phase. By choosing the amplified spin interaction strengths we assure that the condensate is unambiguously within the cyclic-tetrahedral phase and correspondingly that the non-Abelian topology is protected from energetic perturbations. All results presented in this thesis employ these coupling constants.

There are many numerical schemes which can be implemented to model the evolution of the GPE. Here we employ the XMDS2 [204] software package, which implements a number of these schemes with high speed, mature code. Additionally, XMDS2 supports easy parallelisation, allowing us to execute the code on a computer cluster. From the many available options, we implement the fourth order adaptive Runge–Kutta algorithm in the interaction picture. Being adaptive this algorithm provides improved resolution in highly dynamic periods, which is important when studying vortex dynamics. Meanwhile, the Laplacian operator in the GPE can be evaluated using a Fourier-operator method. Hence, to enable the most efficient operation of the fast Fourier transform, we use numerical grids with  $2^n \times 2^n$  grid points, where  $n$  is a positive integer.

In general, the simulations begin from an initial state that we generate using the methods discussed in Sec. 3.2. To anneal towards the ground state, with trapping potential applied, we evolve the system in imaginary time by applying a Wick rotation,  $\tau \rightarrow -i\tau$ , to the GPE in Eq. (3.1) [205]. The wick rotation transforms the unitary operator as  $\exp(-i\hat{H}t/h) \rightarrow \exp(-\hat{H}t/h)$ . The action of the resultant operator is to cause an exponential decay of the energy of the system, with the high energy modes decaying faster than the low energy counterparts. As a result, evolving in imaginary time drives the system towards the local energy minimum. However, in the process the norm decays and thus the order parameter needs to be re-normalised at each time-step.

## 3.2. Preparation of initial states with non-Abelian vortices

A two-dimensional scalar vortex order parameter is represented, after a Madelung transformation, as

$$\Psi(x, y) = \sqrt{n(x, y)}e^{i\theta(x, y)}, \quad (3.2)$$

where  $x$  and  $y$  are Cartesian co-ordinates,  $n(x, y)$  the density profile and  $\theta(x, y)$  the phase. Ignoring the density profile, the characteristic phase winding of a scalar vortex is encapsulated in the representation  $\phi(x, y) = (x + iy)/\sqrt{x^2 + y^2} = e^{i\theta(x, y)}$ , where  $\theta(x, y) = \arctan(y/x)$  is the polar angle. Numerically,  $N$  scalar vortex phase windings, with winding number  $\omega_j$  and position  $(x_j, y_j)$ , can be imprinted into a wave function  $\Phi(x, y)$  by taking a product of  $\phi(x, y)$  representations,

$$\Phi(x, y) = \prod_{j=1}^N \exp[i\omega_j\theta_j(x, y)], \quad (3.3)$$

where  $\theta_j(x, y) = \arctan[(y - y_j)/(x - x_j)]$ . Evolving the state for a short period of wick-rotated time deforms the non-physical constant density profile in the region of the phase singularities, generating the vortex cores. If the system is evolved for too long in imaginary time the vortices will be removed entirely, in an effort to further lower the energy of the system, either by driving them out of the condensate or through vortex annihilation.

For the fractional-charge vortices in spinor condensates, both the intra- and inter-component relative phases of the order parameter are vital for characterising the different vortex types. Similar to the scalar vortices, we can imprint  $N$  vortices with commuting topological charges into a ground state spinor order parameter  $\Phi_{\text{GS}}$  via a product,

$$\Phi_{\text{S}}(x, y) = \left[ \prod_{j=1}^N R(\theta_j(x, y); \pm X(j)_\eta^\nu) \right] \Phi_{\text{GS}}(x, y), \quad (3.4)$$

where  $R(\theta_j(x, y); \pm X(j)_\eta^\nu)$  is the rotation corresponding to the topological charge  $X(j)_\eta^\nu$  of the  $j$ th vortex located at  $(x_j, y_j)$  and  $\Phi_{\text{GS}}(x, y)$  is in our context the cyclic-tetrahedral order parameter. Examples of  $R(\theta_j; \pm X_\eta^\nu)$  rotations for cyclic-tetrahedral phase vortices are presented in Table. 2.1. The scalar product state of Eq. (3.3) can be obtained from Eq. (3.4) by choosing  $R(\theta_j(x, y); \omega_j) = e^{i\theta_j(x, y)}$  and  $\Psi_{\text{GS}}(x, y) = e^{i\phi}$ , where  $\phi$  is arbitrary phase.

When the topological charges of the vortices do not commute the product state in Eq. (3.4) cannot be employed as it does not preserve the local inter-component relative phases of the vortices<sup>1</sup>. Instead, to prepare initial states containing non-Abelian vortices we use a phase matching procedure. As an illustrative example we shall describe the procedure for only two vortices, although it can be extended to systems of  $N$  vortices. For two vortices the procedure operates by first creating two copies of the order parameter. One of the vortices is imprinted in the first copy at  $(x_1, y_1)$ , while the other vortex is imprinted in the second copy at  $(x_2, y_2)$ . These become the order parameters  $\Phi_1$  and  $\Phi_2$ , respectively. A new order parameter,  $\Phi_{\text{S}}$ , is created by mapping the region containing the vortex in  $\Phi_1$  to the equivalent region in  $\Phi_2$ , overwriting the previous details of  $\Phi_2$ . In Fig. 3.1, we show the phase structure of an example  $\Phi_{\text{S}}$ , created by joining the two non-Abelian vortex order parameters  $\Phi_1(x, y) = \Psi((x, y); \text{IV}_0)$  and  $\Phi_2(x, y) = \Psi((x, y); -\text{VI}_{-1}^y)$ . Along the boundary between  $\Phi_1$  and  $\Phi_2$ , which in Fig. 3.1 corresponds to the vertical dotted line,  $\Psi_{\text{S}}$  is set as  $\psi_{\text{cyclic}}$ . Evolving  $\Phi_{\text{S}}$  in imaginary time transforms the  $\psi_{\text{cyclic}}$  boundary wall in a manner which attempts to smoothly join  $\Phi_1$  and  $\Phi_2$ . To aid the imaginary time smoothing, we can apply a global phase rotation to one or both of  $\Phi_1$  and  $\Phi_2$  to provide a better match between the phases across the boundary. However, in many cases phase domain walls, like those in Fig. 3.1(b) and (d), are unavoidable and cannot be removed by imaginary time evolution. Indeed, in some instances the smoothing process may transform the phase such that an additional

<sup>1</sup>Small numbers of non-Abelian vortices can be imprinted using a variant of Eq. (3.4) where the rotations are applied in a spatially non-uniform manner, i.e. the rotations take the form  $R = e^{i\phi} e^{-i\Theta\omega(x, y)\cdot\mathbf{F}}$  [91].

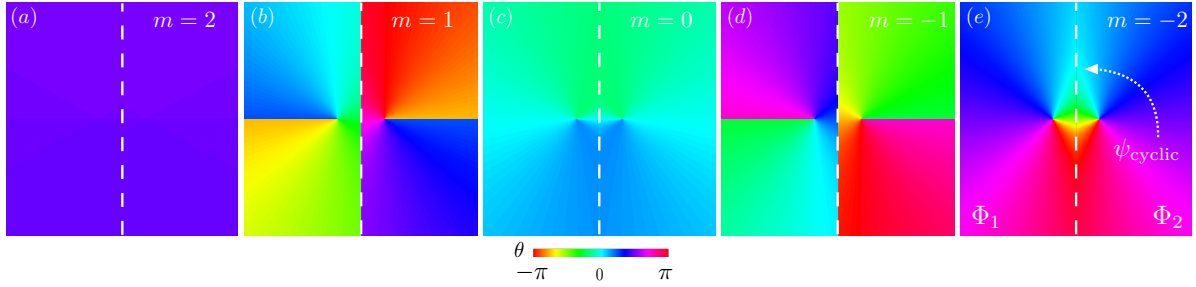


**Figure 3.1:** Phase matching procedure for non-Abelian vortices. (a)-(e) The phase  $\theta$  of each spin component  $m = -2, \dots, 2$  for an initial state  $\Psi_S(x, y)$ , prior to imaginary time evolution. The initial state is constructed by juxtaposing the cyclic-tetrahedral non-Abelian vortex order parameters  $\Phi_1(x, y) = \Psi((x, y); IV_0)$  and  $\Phi_2(x, y) = \Psi((x, y); -VI_{-1}^y)$ , which are defined in the regions left and right of the white dotted line, respectively. Along the white dotted line the order parameter is set as  $\psi_{\text{cyclic}}$ . A similar initial state is used for the numerical simulation of non-Abelian vortex collision dynamics in Fig. 4.3.

vortex is generated at a point on the boundary. Additional magnetic or spin-singlet pair amplitude domain walls may also form due to the order parameter superfluid phase boundary. Such domain walls typically decay during real time evolution.

### 3.3. Detection and identification of vortices

A central part of analysing our numerical results involves locating and identifying the vortices. Mathematically, the topological charge of a vortex can be deduced by considering a closed path  $\Gamma(s)$  with curve parameter  $s$  around the vortex core in real space, which is mapped to a closed path  $\Psi(\Gamma)$  in the order parameter space [42].

Numerically it is possible to algorithmically detect vortices from their associated phase disclinations. This process is simple enough for scalar vortices, though becomes more involved for the fractional-charge vortices in the spin-2 condensate. Detecting scalar vortices is a matter of identifying regions in the numerical grid where the phase winds by  $2\pi\omega$ . The detection algorithm considers the phase winding across all  $2 \times 2$  squares in the grid. Following an anticlockwise path through the four points in each square, the phase differences  $|\Delta\theta_s|$  are calculated and summed  $\sum_s |\Delta\theta_s|$ , see Fig. 3.2. If  $|\Delta\theta_s| > \pi$ , then the phases at each of the points are unwrapped, such that the phase difference avoids any branch cuts. The charge  $\omega$  of the vortex is then found such that  $2\pi\omega - \sum |\Delta\theta| \rightarrow \Delta\lambda$ , where  $\Delta\lambda \in (-\pi, \pi]$ . Strictly, the phase winds about the intersection point of the 4 grid points, rather than about any particular point in the 2 grid.

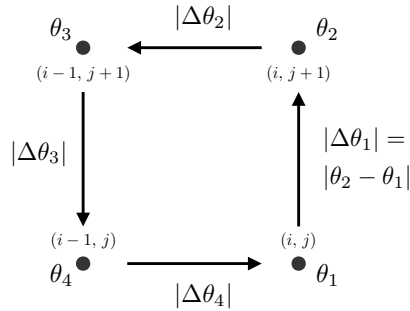


**Figure 3.2:** Scalar vortex identification, considering the phase winding along the anti-clockwise path, given by the arrows, through the  $(i, j)$  points of a  $2 \times 2$  square in the numerical grid. The  $\theta_i$  denote the phases at each of the points.

The minimal method to detect spinor vortices is via their core structures. We can visually trace the vortex dynamics by plotting the spin-component densities  $|\psi_m(\mathbf{r})|^2$  total density  $n(\mathbf{r})$ , the amplitude of the spin density vector  $|\mathbf{F}(\mathbf{r})|^2$ , the magnetization density  $F_z(\mathbf{r})$  and the spin-singlet pair amplitude density  $|A(\mathbf{r})|^2$ . Each of these quantities are defined in Sec. 2.2. Additionally, it is possible to distinguish between certain vortex types based on the core structure. However, the core structure of each class is not fixed and depends on the spin interaction parameters [91].

By treating the spin-components of a spinor order parameter as if they were independent scalar wave functions, we can apply the scalar vortex detection algorithm to also locate the phase windings, across all spin-components, associated with any fractional-charge vortices in a spinor condensate. However, the phase winding alone is insufficient to identify the topological charge of most fractional-charge vortices. A proper identification also requires a determination of the spin rotation of the unknown vortex. Furthermore, there are vortex order parameters, in some bases, that lack any phase factors and thus can neither be located or identified by the scalar vortex detection algorithm.

In Figure. 3.3 we describe an identification method for fractional-charge vortices in a spinor condensate. The method operates as follows. In Figure 3.3(a), a vortex with unknown charge is located somewhere in the numerical grid, either visually by its core structure or using the scalar vortex detection algorithm. Once located, we discretely sample the order parameter along a closed circular path centred on the core. The path begins at an arbitrarily chosen base point and is traversed anti-clockwise. The order parameter at each visited grid point is then stored as the measured series  $\Psi(\Gamma)$  and can be represented in terms of the spherical harmonic decomposition, see Eq. (2.20). The result is the series of geometric objects in Fig. 3.3(a), that reveals the identity of the

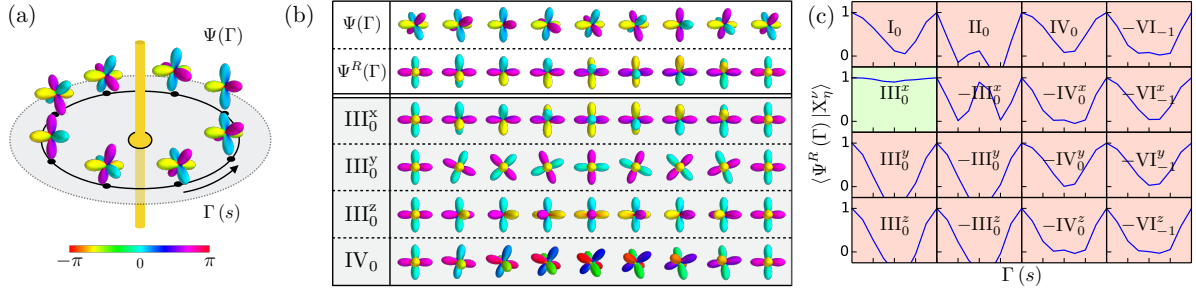


**Figure 3.3:** A method to identify the topological invariant of a vortex. (a) The measured spherical harmonics representation  $\Psi(\Gamma)$  of the vortex to be identified. (b)  $\Psi(\Gamma)$  and its rotated form  $\Psi^R(\Gamma) = e^{i\phi} e^{-i\alpha f_z} e^{-i\beta f_y} e^{-i\gamma f_z} \Psi(\Gamma)$  for phase angle  $\phi = 9\pi/7$  and spin angles  $\alpha = \pi/2$ ,  $\beta = 3\pi/10$  and  $\gamma = 9\pi/7$ . The  $\text{IV}_0$ , and  $\text{III}_0^{x,y,z}$  vortices of the standard basis are shown for comparison. (c) Overlap integral  $\langle \Psi^R(\Gamma) | X_\eta^\nu \rangle$  for vortices  $X_\eta^\nu$  of the standard basis. The correctly identified invariant is shaded green.

vortex and may be used for visualising the characteristic gauge and spin rotations of the vortex. In Figure. 3.3(b) we find a non-unique rotation  $R$ , using a non-linear least squares fitting, which transforms the order parameter at the base point to the cyclic-tetrahedral phase order parameter  $\Psi_{\text{cyclic}}$ , defined in Sec. 2.3. The measured series  $\Psi(\Gamma)$  is then transformed by  $R$  to the series  $\Psi^R(\Gamma)$ , which should be approximately similar to a series corresponding to one of the vortices  $X_\eta^\nu$  in a standard basis. An example standard basis is given in Fig. 2.4 and B.1-B.2. The vortex is measured by comparing the transformed series  $\Psi^R(\Gamma)$  with each of the series  $X_\eta^\nu$  in the standard basis. The comparison takes the form of an overlap integral  $\langle \Psi^R(\Gamma) | X_\eta^\nu \rangle$  performed at each point  $\Gamma(s)$  on the path, see Fig. 3.3(c). Here, the ket  $|X_\eta^\nu\rangle$  refers to a wave function  $\Psi(\mathbf{r}; \pm X_\eta^\nu)$  containing a vortex of type  $X_\eta^\nu$ , see for example Table. 2.1, with the vortex core aligned with the core of the vortex in  $\Psi^R(\mathbf{r})$ . In the idealised situation the overlap equals 1 at each point for the correct vortex and less than 1 for all other vortices. We select the correctly identified vortex, the one shaded green in Fig. 3.3, as the vortex where the sum of the overlap at each point is greater than 0.8, after normalising to the number of points.

There is an important yet subtle point regarding our measurement of the topological charges of vortices. In general, there is no unique way to assign a topological charge to a vortex [42]. For scalar vortices, we arbitrarily fix a convention which states that a counter-clockwise phase winding corresponds to a vortex, and the reverse to an anti-vortex. Similarly, individual spinor vortices can only be determined up to their equivalency class, as we are always free to apply a global equivalency transformation which cycles through the charges in the class. This ambiguity appears in our identification method through the non-unique  $R$  transformation, which can be chosen such that  $\Psi^R(\Gamma)$  approximates

any series  $X_\eta^\nu$ , with fixed  $X$  but unfixed  $\nu$ . Thus, when measuring single vortices we are free to situate the base point anywhere within the condensate. Typically, for our circular paths we will place the base point at  $s = 0$ , where the curve parameter  $s$  is the polar angle. In condensates with multiple vortices, we could measure all the topological charges individually using independent base points, so called freely homotopic paths [42], but then we could only make a statement about the relative classes of the vortices. However, if we use paths originating from a shared base point, then the actual charges can be measured in a relative sense, i.e vortices that are measured to have distinct charges remain distinct after a global equivalency rotation. In effect, we can measure the classes and algebra of the topological charges of the vortices, even if we still can not make a definite measurement of the charges from the rotations alone. Other consistency checks like the total topological charge and vortex core structure may help to provide a more definitive measurement of the topological charges of a pair of vortices. For the vortex dipole systems in Chapter 4, the charges are measured with two circular paths sharing a base point equidistant between the two vortices. The base point in such cases is located at the curve parameters  $s_1 = 0$  and  $s_2 = \pi$  for the path about the vortex on the left and right of the base point, respectively.

The overlap protocol is a comparison measurement and is thus not an explicit measurement of the topology. A topological measurement of the charge was considered, using a non-linear least squares fit to measure the total rotation across all the spherical harmonic objects in the rotated series  $\Psi^R(\Gamma)$ . This method did not progress as the fit failed to converge on a single overall rotation for the series. However, by sufficiently increasing the spatial sampling, that is having sufficiently many grid points that the order parameter barely changes between the points, the least squares method could potentially function well. Computational algorithms are typically quite poor at tracking the rotations of 3D objects. Comparatively, the human mind has evolved to do such complex tasks innately. Hence, in those instances where the overlap procedure fails it is possible to identify a vortex by visually inspecting its series  $\Psi(\Gamma)$  and comparing with the standard basis. An example of a particular situation where the overlap measurement might fail, is when trying to measure the total charge of multiple vortices which are not sufficiently centred within the path. While the overall rotation of the corresponding measured series does contain the correct topology, there will be local segments of the series with distinctly different rotations, corresponding to sectors of the path that pass closer to one particular vortex in the configuration. One solution is to use a circular path with radius much larger than the intervortex spacing. However, this is difficult to achieve,

for example, when studying turbulence in a trapped spinor BEC where the vortices are roughly uniformly distributed throughout the finite domain of the condensate.

Unlike the scalar vortex detection method, which algorithmically *locates* and identifies all vortices in the condensate, the method described above can only be used to identify already located vortices. Ideally, the identification process would include an additional initial step which exhaustively locates all spinor vortex types in the data, including those without phase factors. However, it remains unclear how to solve the vortex detection problem of fractional vortices for sparsely sampled order parameters.



## Chapter 4.

# Collision dynamics of two-dimensional non-Abelian vortices in spin-2 Bose–Einstein condensates

In Chapter 2, we noted that the algebra of the topological charges of a pair of vortices enacts different collision dynamics. Similarly, constraining the condensate to two-dimensions results in point-like vortex excitations whose collision events differ from those of vortex lines. In this chapter we study the hitherto unexplored collision dynamics of fractional-charge vortices in the cyclic-tetrahedral phase of a 2D spin-2 BEC. A detailed understanding of vortex collision dynamics is fundamental to characterising the behaviour of multi-vortex configurations as occur in quantum turbulence.

Reconnections of scalar vortices were directly imaged in a series of superfluid Helium experiments [49, 50] and more recently in trapped BECs [165, 166]. Similarly, the collision dynamics of scalar vortex dipoles have been experimentally observed by the Anderson group [95] for a 2D BEC formed in a highly oblate harmonic trap. In their experiment, a vortex dipole is generated by translating the harmonic trap to push the condensate past a repulsive barrier, in the form of a blue-detuned Gaussian laser beam, faster than the superfluid flow critical velocity. In the condensate frame of reference this is equivalent to dragging the laser through BEC. Simultaneously, the height of the barrier is linearly ramped down to zero such that, after the sweep of the condensate, only the vortex dipole remains. The mutual induction between the vortex velocity fields imbues the dipole with linear momentum, propagating the vortices along mirrored periodic orbits through the

condensate, see the schematic in Fig. 4.1(d). When the orbits approach one another a collision event may occur. In 2D, vortex reconnection becomes annihilation. The annihilation is described topologically by the group operation of the two vortex charges, giving the total charge  $\gamma_2\gamma_1 = \mathbb{I}$ . However, in the experiment the vortices do not fully annihilate, rather they coalesce into a topologically trivial rarefaction pulse, variously named as a vortexonium [206], or as a Jones-Roberts soliton [207]. The formation of the soliton has been confirmed theoretically in Ref. [96, 97]. As the soliton propagates its momentum causes it to bend producing a characteristic bow structure. The soliton may reform into a vortex-antivortex pair upon entering a region with lower particle density due to the inhomogeneity of the harmonic trap. For a finite temperature condensate, full annihilation of the vortices may be realised if the soliton has sufficient momentum to leave the condensate [208]. Comparatively, at "zero" temperature annihilation is a many-body process in which the soliton scatters off a third vortex dispersing its energy into sound waves [206, 209, 210].

Similar collision experiments have been performed by the Shin group [135] for Abelian half-quantum vortex dipoles in the polar phase of a spin-1 condensate. An external magnetic field with quadratic Zeeman shift  $q > 0$  is employed to initially place the condensate in the the easy-axis polar phase with all atoms in the  $m = 0$  spin component. As in the Anderson experiment, a repulsive barrier is swept through the effectively single-component condensate to generate a vortex dipole. Immediately after the vortex generation a  $\pi/2$  radio-frequency pulse inverts the quadratic Zeeman strength to  $q < 0$  realising the easy-plane polar phase, corresponding to the order parameter  $\Psi_{\text{polar}}^{(1)}$  in Sec. 2.4, where the vortex dipole is unstable and splits into two half-quantum vortex dipoles. The orbital motion of the half-quantum vortex dipoles was observed via their ferromagnetic cores using in situ magnetisation imaging [211]. The annihilation of opposite circulation vortices was observed post collision in these experiments and confirmed numerically in Ref. [212], though the microscopic details, such as whether the annihilation of fractional-charge vortices proceeds via an intermediate soliton state, remain unclear.

Non-Abelian vortices have not yet been realised experimentally, though the rung formation collision dynamics of non-Abelian vortex lines in a spin-2 BEC were elucidated numerically in the pioneering studies of Kobayashi *et al.* [88] for the cyclic-tetrahedral phase, and later for the biaxial nematic phase by Ruostekoski *et al.* [91]. The reaction dynamics of non-Abelian vortex pairs in 2D BECs have remained unexplored. Here, we numerically simulate the vortex dipole collision experiments like those of the Anderson and Shin groups, for both Abelian and non-Abelian vortex pairs in the cyclic-tetrahedral

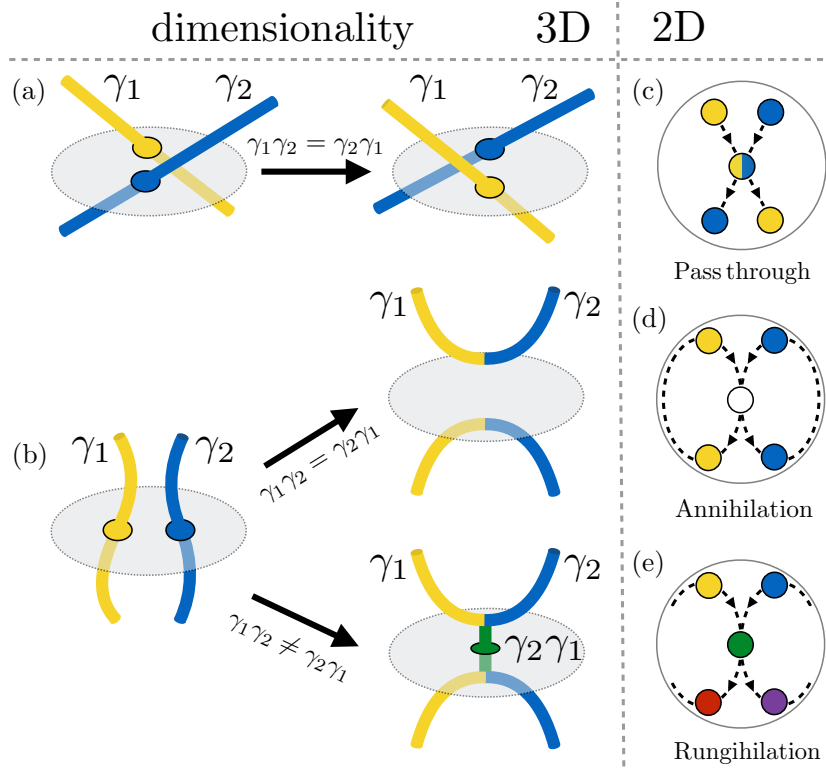


**Figure 4.1:** Schematic of vortex collision dynamics in two and three-dimensional condensates. (a), (b) left: Initial state of vortex lines with charges  $\gamma_1$  and  $\gamma_2$  piercing a two-dimensional condensate plane, grey shaded disk, that intersects the collision cusp. (a) right: Abelian vortices pass through. (b) right top: Abelian vortices undergo a vortex reconnection. (b) right bottom: Non-Abelian vortices form a rung vortex with charge  $\gamma_2\gamma_1$ . (c)–(e) Collision of vortices in a two-dimensional condensate, corresponding to the dynamics of the vortex lines on the disk in (a)–(b). Vortices are denoted by circles with colour representing the charge. (c) Passing through, split circle denotes overlapping vortices. (d) Annihilation, white circle denotes absence of vortices. (e) Rungihilation, green circle denotes the rung vortex.

phase of a 2D spin-2 Bose–Einstein condensate. The work presented here is based on Ref. [107].

As in Sec. 2.6, we can use topology to infer the potential collision dynamics of two-dimensional vortices. As shown in Fig. 4.1, the dynamics of vortices in 2D are expected to correspond to the motion of the intersection sites between virtual 3D vortex lines and a 2D plane. In 3D systems two initially parallel vortex lines can locally change their relative orientation to initiate a topological reaction such as a reconnection; there exists no such freedom for point-like vortices. Therefore, in 2D, only  $\gamma_2\gamma_1$  type topological reactions of vortices  $\gamma_1$  and  $\gamma_2$  may occur with  $\gamma_1\gamma_2^{-1}$  events being suppressed by dimensionality and topological charge conservation. As shown in Fig. 4.1(c), pass through remains unchanged for point-like vortices. Vortex reconnection becomes vortex-antivortex annihilation where,

as shown in Fig. 4.1(d), the collision leaves the condensate vortex free. For non-Abelian vortex pairs we anticipate a new collision event, coined rungihilation. As shown in Fig. 4.1(e), rungihilation is a 2D equivalent of rung formation dynamics of 3D vortices in which two non-Abelian vortices collide and fuse into a non-trivial rung vortex with charge  $\gamma_2\gamma_1$ . In following numerical experiments, we explore each of these collision outcomes for representative vortex pairs.

## 4.1. Numerical experiments

We numerically simulate a condensate of  $^{87}\text{Rb}$  atoms with effective particle number  $N = 75000$  on a mesh with  $2048 \times 2048$  grid points. The condensate is trapped in a harmonic potential with trap frequency  $\omega_{\text{trap}} = 2\pi \times 200$  Hz. The dimensionless coupling constant  $c'_0 = c_0 N / \hbar \omega_{\text{trap}} l^2 = 0.231N$ , where  $c_0$  is specified by the experimentally measured scattering lengths  $a_i$  of  $^{87}\text{Rb}$  [190]. As per Chapter 3 the dimensionless spin interaction strengths are chosen as  $c'_1 = c'_2 = 0.5 c'_0$ . In the following we describe the simulation results for vortex-antivortex annihilation, pass through, and rungihilation for the given representative vortex pairs: the Abelian pair collisions;  $[\text{IV}_0, -\text{VI}_{-1}]$ , and  $[\text{IV}_0, \text{IV}_{-1}]$ ; and a non-Abelian pair collision  $[\text{IV}_0, -\text{VI}_{-1}^y]$ . As in the experiments by the groups of Anderson [95] and Shin [135], the mutual induction field of the vortex pair propels the vortices, inducing a collision event if the paths overlap. In contrast to these experiments, in our simulations the vortices are created using the phase imprinting methods described in Sec. 3.2.

## 4.2. Annihilation and pass through of Abelian vortices

We first consider the vortex-antivortex annihilation for an Abelian vortex pair with charges  $\text{IV}_0$  and  $-\text{VI}_{-1}$ . The representative order parameters are

$$\Psi(\mathbf{r}; \text{IV}_0) = e^{i\theta/3} e^{-i\theta(f_x+f_y+f_z)/3\sqrt{3}} \Psi_{\text{cyclic}} \quad (4.1)$$

and

$$\Psi(\mathbf{r}; -\text{VI}_{-1}) = e^{-i\theta/3} e^{-i\theta(-f_x-f_y-f_z)/3\sqrt{3}} \Psi_{\text{cyclic}}, \quad (4.2)$$

where  $\theta$  is the polar angle. Each vortex has a magnetised core with  $F_z > 0$ , which is useful for tracing the vortex paths shown in Fig. 4.2. The vortices, driven by their mutual induction field, travel along paths which overlap at  $\tilde{t} = 6.0$  and undergo vortex-antivortex annihilation. Our numerical experiments confirm that, Like the scalar vortices, the annihilation is survived by a remnant magnetic “vortexonium” highlighted in Fig. 4.2(c). Topologically, the magnetic vortexonium is equivalent to the trivial vortex  $I_0$ . The vortex pair is reformed when the vortexonium travels into the low density boundary region of the condensate where vortex pair creation becomes energetically feasible. We have confirmed, by measurement (Sec. 3.3), that the reformed vortices have charges  $IV_0$  and  $-VI_{-1}$ .

While pass through is topologically permissible for Abelian vortices, its occurrence depends on the vortex kinematic details. For example, for scalar vortex-vortex (antivortex-antivortex) pairs a pass through event is hindered by the Coulomb-like repulsive interaction arising from the energy barrier associated with the superflow mass currents. In spinor BECs the superflow mass currents of the two vortices may be associated with different spin-components. Consequently, the repulsive energy barrier may not exist thereby allowing the vortices to pass through. Figure 4.2(e)-(g) shows a pass through event for two Abelian vortices with charges  $IV_0$  and  $IV_{-1}$ . To generate such vortex wave functions we consider a second cyclic-tetrahedral ground state  $\Psi' = e^{-i\cos^{-1}(1/\sqrt{3})f_y} e^{-i\pi f_z/4} \Psi_{\text{cyclic}}$ .

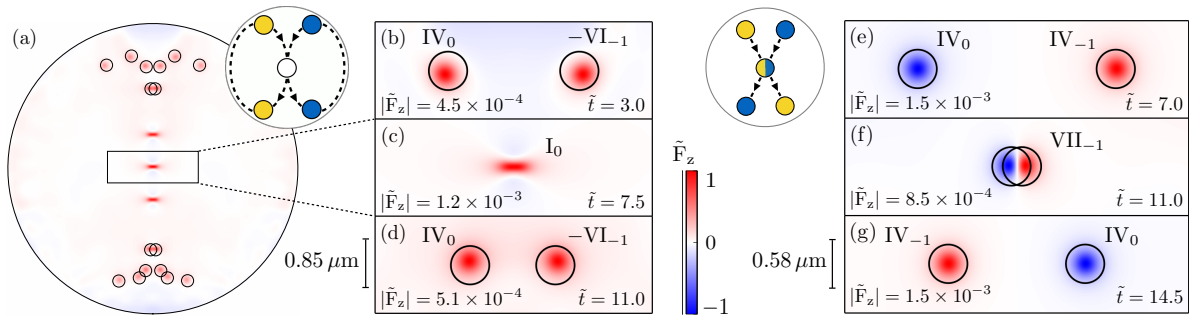


**Figure 4.2:** Collision dynamics of vortex pairs with Abelian algebra. (a)-(d) Annihilation of  $IV_0$  and  $-VI_{-1}$  vortices. (a) Motion of the vortices through the condensate traced by their magnetised cores. The figure is a composite created by overlaying the normalised sum of  $\tilde{F}_z$  at eleven different times. (b)-(d) Vortices at times  $\tilde{t}$  prior, during and post the collision event. (e)-(g) Pass through of  $IV_0$  and  $IV_{-1}$  vortices. The locations of the vortices are represented by the circles surrounding the magnetic vortex cores and the normalisation constant of the magnetisation is provided in each frame (b)-(g).

By applying appropriate gauge and spin rotations to  $\Psi'$  we obtain vortex wave functions

$$\Psi(\mathbf{r}; \text{IV}_0) = e^{i\theta/3} e^{i\theta f_z/3} \Psi' \quad (4.3)$$

and

$$\Psi(\mathbf{r}; \text{IV}_{-1}) = e^{-i2\theta/3} e^{i\theta f_z/3} \Psi', \quad (4.4)$$

with magnetised cores of  $F_z = -\sqrt{2/3}$  and  $F_z = 2/\sqrt{3}$ , respectively. The superfluid mass currents of the vortices are in the  $m = 2$  and  $m = -1$  spin states, respectively. Thus, the vortices are driven towards each other by the interactions with their respective image vortices. The vortices overlap at  $\tilde{t} = 11.0$  and then pass through each other. During the overlap the topology is identified by the total charge given by  $\text{IV}_0\text{IV}_{-1} = \text{VII}_{-1}$ . A clean pass through was observed in simulations with initial states having identically zero population in the unpopulated components of  $\Psi(\mathbf{r}; \text{IV}_0)$  and  $\Psi(\mathbf{r}; \text{IV}_{-1})$ .

### 4.3. Rungihilation of non-Abelian vortices

The non-Abelian vortex pair  $\text{IV}_0$  and  $-\text{VI}_{-1}^y$  are initialised with order parameters

$$\Psi(\mathbf{r}; \text{IV}_0) = e^{i\theta/3} e^{-i\theta(f_x+f_y+f_z)/3\sqrt{3}} \Psi_{\text{cyclic}} \quad (4.5)$$

and

$$\Psi(\mathbf{r}; -\text{VI}_{-1}^y) = e^{-i\theta/3} e^{i\theta(-f_x-f_y+f_z)/3\sqrt{3}} \Psi_{\text{cyclic}}, \quad (4.6)$$

respectively. Both vortices have a core structure with  $F_z > 0$  as shown in Fig. 4.3(a). While the vortex pair is not a strict vortex dipole, the opposing superfluid velocities interact to produce the orbital motion. The vortex pair collides forming a rung vortex with  $F_z = 0$  and non-zero  $|A|$  core highlighted in Figs. 4.3(b) and (e). The rung has a topological charge  $-\text{VI}_{-1}^y\text{IV}_0 = \text{III}_0^y$ . Since an isolated rung vortex can only be classified up to its class, a particular topological charge is ascribed according to the result of  $\gamma_2\gamma_1$ , where  $\gamma_1$  and  $\gamma_2$  are the measured charges of the vortices before their collision. The rung exists for  $\tilde{t} = 5.0$  time units before breaking up into a secondary pair of non-Abelian vortices with different topological charges. The non-Abelian rungihilation and subsequent pair-creation process not only changes the vortex charges but is also accompanied by the

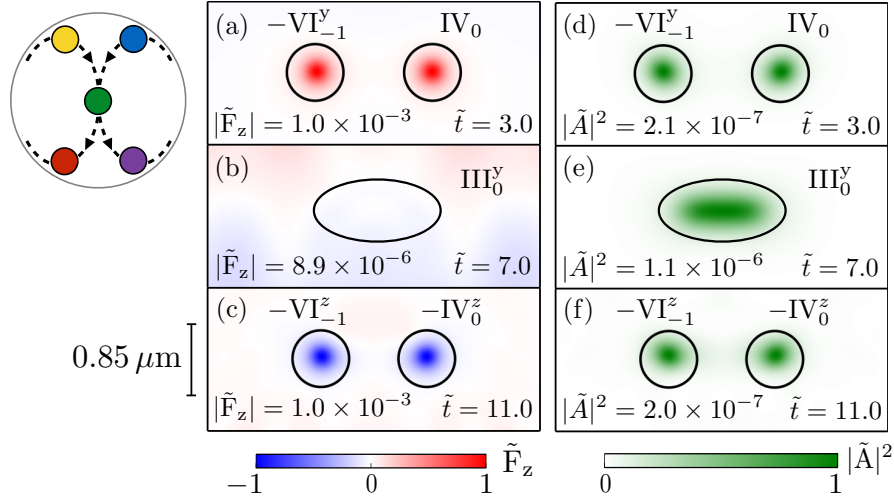


**Figure 4.3:** Rungihilation of  $IV_0$  and  $-VI_{-1}^y$  vortices with non-Abelian algebra. (a)-(f) Vortices at times  $\tilde{t}$  prior, during and post the collision event. (a)-(c) The normalised magnetisation density  $\tilde{F}_z$ . (d)-(f) The normalised spin-singlet amplitude  $|\tilde{A}|^2$ . The locations of the vortices are represented by the circles, the rung is highlighted by the ellipses, and the normalisation constants  $|\tilde{F}_z|$  and  $|\tilde{A}|^2$  are provided for each frame.

reversal of the direction of the magnetised core structure, cf. Figs. 4.3(a) and (c), such that the new vortices have cores with  $F_z < 0$ , providing an experimentally detectable signal of this unconventional topological reaction. The newly spawned vortices are measured to have charges  $-VI_{-1}^z$  and  $-IV_0^z$ , where we have used conservation of charge,  $(-VI_{-1}^y)(-IV_0^y) = III_0^y$ , and the sign of the core magnetisation to refine the measurement beyond the equivalency class. If the pair-created  $-VI_{-1}^z$  and  $-IV_0^z$  vortices are allowed to complete a full orbit they will also collide to form a  $III_0^y$  rung vortex which subsequently spawns the initial vortex pair  $IV_0$  and  $-VI_{-1}^y$ , with the corresponding magnetisation reversal.

## 4.4. Summary

We have investigated the collision dynamics of vortex pairs in the cyclic-tetrahedral state of two-dimensional spin-2 Bose–Einstein condensates. We have shown using numerical experiments that the collision of a pair of vortices may result either in annihilation, passing through, or rungihilation of the two vortices. We have identified the rungihilation event as the two-dimensional counterpart to rung formation of three-dimensional non-Abelian vortices [88, 91]. As these results are grounded in the topology, they apply equally to non-Abelian vortices in higher spin condensates [113, 117, 158], where non-Abelian

collision dynamics are likely a common occurrence, and to non-Abelian topological excitations in other physical systems.

Experimentally, it is relatively simple to extend the procedures used by the Anderson [95] and Shin groups [135] to demonstrate the collision dynamics of non-Abelian vortices in two-dimensional spin-2 condensates. The major limitations are the accessibility of the cyclic-tetrahedral superfluid phase and phase-imprinting non-Abelian pairs, see the discussion in Chap. 3. Nonetheless, it may be possible to create Abelian vortex pairs capable of annihilation by dragging a repulsive barrier through a BEC in the cyclic-tetrahedral phase. However, unless  $|\mathbf{F}(\mathbf{r})| \neq 0$ , which may be the case experimentally, the barrier is likely to shed a pure gauge vortex pair, with charges  $I_1$  and  $I_{-1}$ , rather than fractional-charge vortices [213]. Measuring topological charges of vortices in an experiment is not sufficiently feasible at present. Thus, we depend on characteristic signatures in other physical observables to identify the collision dynamics. Imaging the spin-singlet pair amplitude, useful for characterising the rung vortices, remains an experimental challenge. However, the rungihilation could possibly be inferred by the associated reversal of the vortex core magnetisation using the same magnetisation sensitive imaging techniques [211] employed in the Shin experiment.

There are a number of interesting applications where the topological interactions of non-Abelian vortices play a central role in the characteristics of the system. Rung formation has opened a new research area of three-dimensional non-Abelian quantum turbulence typified by a novel helicity cascade [106]. Similarly, The rungihilation of two-dimensional non-Abelian vortex pairs is anticipated to have interesting ramifications for energy flow in 2D quantum turbulent states involving vortices with non-commuting topological charges. The properties of 2D non-Abelian quantum turbulence will be further explored in Chapter 6.

In the following Chapter 5, we will map the vortex collision dynamics onto the fusion rules of types of non-Abelian vortex anyons. Vortices with topological charges in the same equivalency class are indistinguishable and the class defines a particle type. These particles are similar to the fluxon anyons described in Sec. 2.8. The resultant uuparticles formed from the composition of two anyons are given by a fusion rule. For our non-Abelian vortices the collision dynamics are completely defined by the fusion rules of the non-Abelian vortex anyons.

## Chapter 5.

# Braiding and fusing of non-Abelian vortex anyons

A number of experiments have explored the potential realisation of non-Abelian anyons in condensed matter systems including Majorana zero modes in nanowires [34–37] and quasiparticles in certain fractional quantum Hall states [39–41]. Other non-Abelian anyon models have been proposed to utilise ‘fluxons’ in non-Abelian toric code models [29] or discrete gauge theories [44, 45, 60, 61]. Notwithstanding, the existence of a physical system of non-Abelian anyons capable of universal quantum computation remains an open question.

Discrete gauge theories share many similarities with spinor Bose–Einstein condensates and their non-Abelian topological excitations. These theories are characterised by the spontaneous symmetry breaking of a two-dimensional system, with a continuous gauge symmetry group, to a broken symmetry phase described by a finite subgroup, the stabiliser or isotropy group  $H$ . In the symmetry-broken phase, “vortex-like” topological excitations arise in the form of fluxons carrying a magnetic flux corresponding to an element of the non-Abelian finite group  $H$ . In the context of this chapter we shall refer to all topological charges as fluxes. In addition to fluxons, there are  $H$ -charges or chargeons, labelled by the complete set of unitary irreducible representations of  $H$  [173], and charge-flux composites known as *dyons* [214–217]. The full spectrum of excitations is labelled using the quantum double of the symmetry group. While interesting, the full details of the quantum double algebra are not necessary to understand the physics of fluxon excitations presented here, however Refs. [60] and [61] review the relevant details of the quantum double in the context of discrete gauge theories in high energy physics.

Our discussion of non-Abelian vortex anyons will focus primarily on the fluxon type excitations. In our system, the fluxons map onto the non-Abelian vortices and more specifically the low-energy Bogoliubov quasiparticle eigenstates localised within a vortex core [164]. The fluxons are defined in a very similar way to our non-Abelian vortices. Using homotopy theory, a specific fluxon can be represented by a particular flux or by any of its conjugates within this group. The conjugate fluxes form an equivalency class in  $H$ . There is no invariant way to assign fluxes in a given class to the associated fluxons and, as such, each class defines a distinguishable fluxon type with multiple corresponding indistinguishable fluxes. This degeneracy becomes important during the adiabatic counterclockwise exchange of two fluxons. For fluxons with non-commuting fluxes  $\gamma_1$  and  $\gamma_2$ , respectively, the exchange realises a non-trivial monodromy, which transports the fluxes within their equivalency classes according to the map  $(\gamma_1, \gamma_2)$  to  $(\gamma_2, \gamma_2\gamma_1\gamma_2^{-1})$  [44, 45]. The monodromy interaction between fluxons acts in an identical manner to the topological influence between our non-Abelian vortices. Similarly, the result of fusing two fluxons is given by an ordered product of their fluxes. The fusion of two fluxons,  $a$  and  $b$  of same or different type, may result in multiple fluxon types  $c$ , corresponding to a fusion rule with multiple non-zero multiplicities  $N_{ab}^c \neq 0$ . These characteristics collectively identify fluxons as non-Abelian anyons.

The chargeons are also non-Abelian anyons. They are labelled by unitary irreducible representations of  $H$ , see Appendix C. When  $H$ -charges are braided around fluxes, the result is analogous to the Aharonov-Bohm effect, see Fig. 5.1. The flux  $\gamma$  will act on the charge  $\alpha$  by the matrix  $\alpha(\gamma)$  that represents the element  $\gamma \in H$ , which labels the flux, in the representation  $\alpha$  of  $H$ , which labels the charge. When the group  $H$  is commutative, this matrix reduces to a simple scalar phase factor, the usual Aharonov-Bohm phase. A similar result is obtained when braiding dyons, although in this case the acting group is a centralizer subgroup  $C_H(\gamma) = \{\gamma' \in H \mid \gamma\gamma' = \gamma'\gamma\}$  of  $H$ . Even if no particles with charge are present, charges can still play a role in braiding, since fusion of fluxes may yield anyons with non-trivial charge. For example, two particles (fluxons) each carrying a pure flux may fuse in such a way that the two fluxes annihilate but nevertheless result in a non-trivial  $H$ -charge. Even if such fluxes are kept apart, they act as carrying a single delocalized charge when a third flux is braided around such a pair of fluxes. The delocalized charge associated with the flux pair is the elusive Cheshire charge, so named after the Cheshire cat, which could disappear, but leave its grin visible [218–220]. In our system, the chargeon particles may be viewed as Bogoliubov ‘zero’ modes, such as those associated with a phonon, a magnon or a soliton, which are organised into multiplets under the action of  $H$  (which leaves the state of the condensate invariant). It may also

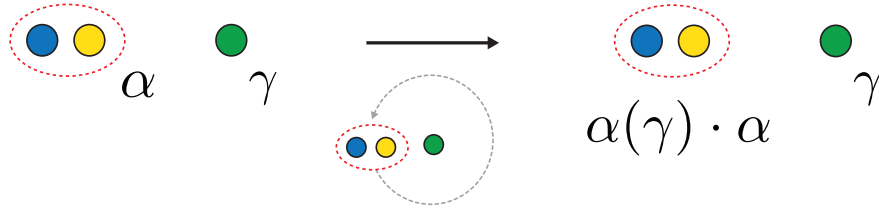


**Figure 5.1:** Effective Aharonov-Bohm effect between a charge and flux. Braid of a fluxon pair with Cheshire charge  $\alpha$ , denoted by the dotted red ellipse, about a fluxon with flux  $\gamma$ . The total flux of the fluxon pair commutes with  $\gamma$ . After the braid the charge acquires a non-Abelian Aharonov-Bohm phase  $\alpha(\gamma)$ .

be possible for these systems to exhibit completely delocalized Cheshire charges, though it remains unclear how the Cheshire charge physically manifests in this context.

Here we demonstrate that the topological interactions of the non-Abelian fractional vortices in spinor Bose–Einstein condensates contain the essential aspects of a non-Abelian ‘fluxon’ anyon model and are potentially useful for applications in topological quantum information processing and storage. The most compelling aspect of these non-Abelian vortex anyons is their capacity to tangibly demonstrate the principles of topological quantum computing, particularly at the fluxon level where the anyons consist of easy to grasp vortex excitations. A key aspect of this tangibility stems from the controllability of spinor condensates which permits simple experimental procedures to controllably enact the braiding and fusion of the vortex anyons [221, 222]. Anderson *et al.* [222] have experimentally demonstrated the capacity to deterministically create, pin and translate vortex dipoles in a highly oblate scalar condensate. The procedure employs two external pinning potentials in the form of blue-detuned Gaussian laser beams which puncture holes in the condensate density. The location of the focus point of each beam can be controlled and freely translated through the condensate. In what is called the ‘chopstick’ technique, the laser beams are propagated, from their initially overlapping positions, along diverging linear paths at a constant speed, substantially slower than the speed of sound and the critical velocity necessary for vortex nucleation. The motion of the separating beams displaces the fluid such that two opposite circulation vortices are created localised to the pinning potentials. From here, the beams were manipulated to bring one vortex back to the starting point. After a short hold time the beams were linearly ramped down, revealing the presence of the vortices at the prior locations of the pinning sites and demonstrating the capacity to controllably transport vortices around the condensate. The rate at which the beams are ramped down must be sufficiently fast that the vortices do not escape too early, complicating the imaging, but slow enough

that the change in the density profile does not generate collective excitations of the condensate, e.g. a sloshing motion or sound waves. It was also demonstrated that both beams could be brought together to fuse the vortices together, resulting in an observed annihilation of the vortices. Additionally it is entirely feasible that the beams could be translated to braid the vortices about each other. The same techniques can be employed in a spin-2 condensate to manipulate vortex anyons. The controlled braiding and fusion operations required for topological information processing are therefore possible.

In the following classical mean-field theory numerical experiments, we simulate the braiding and fusion of non-Abelian vortex anyons by employing such external pinning potentials to manipulate the states of topological qubits constructed from such non-Abelian vortex anyons.

## 5.1. Numerical experiments

The numerical experiments are performed for a condensate with effective particle number of either  $N = 3 \times 10^5$ , for the experiments in Fig. 5.2 and 5.6, or  $N = 1.75 \times 10^5$ , for the single qubit experiment in Fig. 5.4, on a spatial mesh of  $1024^2$  grid points. The numerical results are presented in non-dimensionalised units where  $\omega = 2\pi \times 5$  Hz. The dimensionless coupling constant  $c'_0 = c_0 N / \hbar \omega l^2$  is determined from the experimentally measured scattering lengths of  $^{87}\text{Rb}$  [190–192]. As per Chapter 3 the dimensionless spin interaction strengths are chosen as  $c'_1 = c'_2 = 0.5 c'_0$ .

We consider a quasi-uniform condensate in a trapping potential  $V_{\text{ext}} = A \tanh[(x/a)^6 + (y/b)^6]$ , where  $A = 50 \hbar \omega$ ,  $a = (86, 59, 120) \mu\text{m}$  and  $b = (52, 45, 52) \mu\text{m}$ , for each of the numerical experiments in Figs. 5.2–5.4 and Fig. 5.6, respectively. The pinning potentials used for moving the vortices are modelled as Gaussian laser beams [223]

$$V_{\text{pin}}(r, t) = \frac{P}{\sqrt{2\pi}\sigma^2} e^{-\frac{(x-x_0)^2 + (y-y_0)^2}{2\sigma^2}}, \quad (5.1)$$

where  $(x_0, y_0)$  is the location of the focus point,  $P = 63 \hbar \omega$  and  $\sigma = 0.5l$ . Upon braiding the pinning potentials are moved with an orbital angular frequency  $\omega_{\text{pin}} = \pi^2/2$  rad  $\text{s}^{-1}$ . The vortices are fused by bringing pinning potentials together until they overlap whereupon their amplitudes  $P$  are linearly ramped down over a time period of  $\approx 127$ ms.

## 5.2. Non-Abelian vortex anyons

Physically, vortices with non-commuting topological fluxes are characterised by the non-trivial, path dependent, topological influence. Figure 5.2 shows the outcome of a numerical experiment that demonstrates the exotic braiding and fusion dynamics of non-Abelian vortices. The system is initialised at time  $t = 0$  in Fig. 5.2a by creating four non-Abelian vortices in the BEC by phase-imprinting two vortex-antivortex pairs, one on the left and one on the right hand side of the rectangular condensate. Using pinning potentials that model an array of Gaussian-shaped laser beams that repel atoms, the vortices can be pinned and controllably moved around, forming a braid in their space-time world lines as shown in Fig. 5.2a. A plat closure of the braid is realised by the initial pair-creation and final fusion of the vortex pairs. The full braid and fusion of the vortices realises the link L6a2 in the Thistlethwaite Link Table, which is accessible at Ref [224]. The effects of braiding the vortices are observed at different dimensionless times  $\tilde{t}$  after alternatively, (i) releasing the pinning potentials and measuring the properties of the four vortices, see lower rows in Fig. 5.2(b-f), or, (ii) fusing the two vortex pairs first and then measuring the result after releasing the pinning potentials, see upper rows in Fig. 5.2(b-f). The vortex locations are visualised via their core structure, which may have non-zero spin-singlet pair amplitude,  $|A|^2$ , and/or non-zero magnetisation,  $F_z$ .

A detailed understanding of the observed dynamics comes from labelling the flux of each vortex in Fig. 5.2(b-f), using our vortex identification method described in Sec. 3.3. Prior to fusion at each time step, the fluxes are measured using four paths in the condensate, each originating from a shared base point located in the centre of the condensate. Each of the inner vortices are measured directly by a loop enclosing their vortex core giving fluxes  $\gamma_i$ . The outermost fluxes are determined from the total fluxes measured using loops enclosing the left and right hand vortex pairs, respectively. As an example, for the leftmost pair with unknown charges  $\gamma_1$  and  $\gamma_2$ , the charge  $\gamma_1$  is inferred from  $\gamma_1 = \gamma_2^{-1}\gamma_{\text{TL}}$ , where  $\gamma_2$  and  $\gamma_{\text{TL}}$  are the measured fluxes of the inner vortex and the pair, respectively. Measurements at different time steps do not share a common base point. Therefore, consistency between the measured fluxes at different times must be enforced by hand. From left to right, the initial fluxes are chosen as  $\text{III}_0^x$ ,  $-\text{III}_0^x$ ,  $\text{IV}_0$  and  $-\text{VI}_{-1}$ . In each segment of the braid diagram in Fig. 5.2(a) only two vortices are braided leaving two fluxes unchanged. Thus, an unambiguous assignment of fluxes can be made at each time step via a conjugation of form  $g\gamma_i g^{-1}$  applied to each measured flux,  $\gamma_i$  for a unique  $g \in H$  which enforces the consistency of the unchanged fluxes.

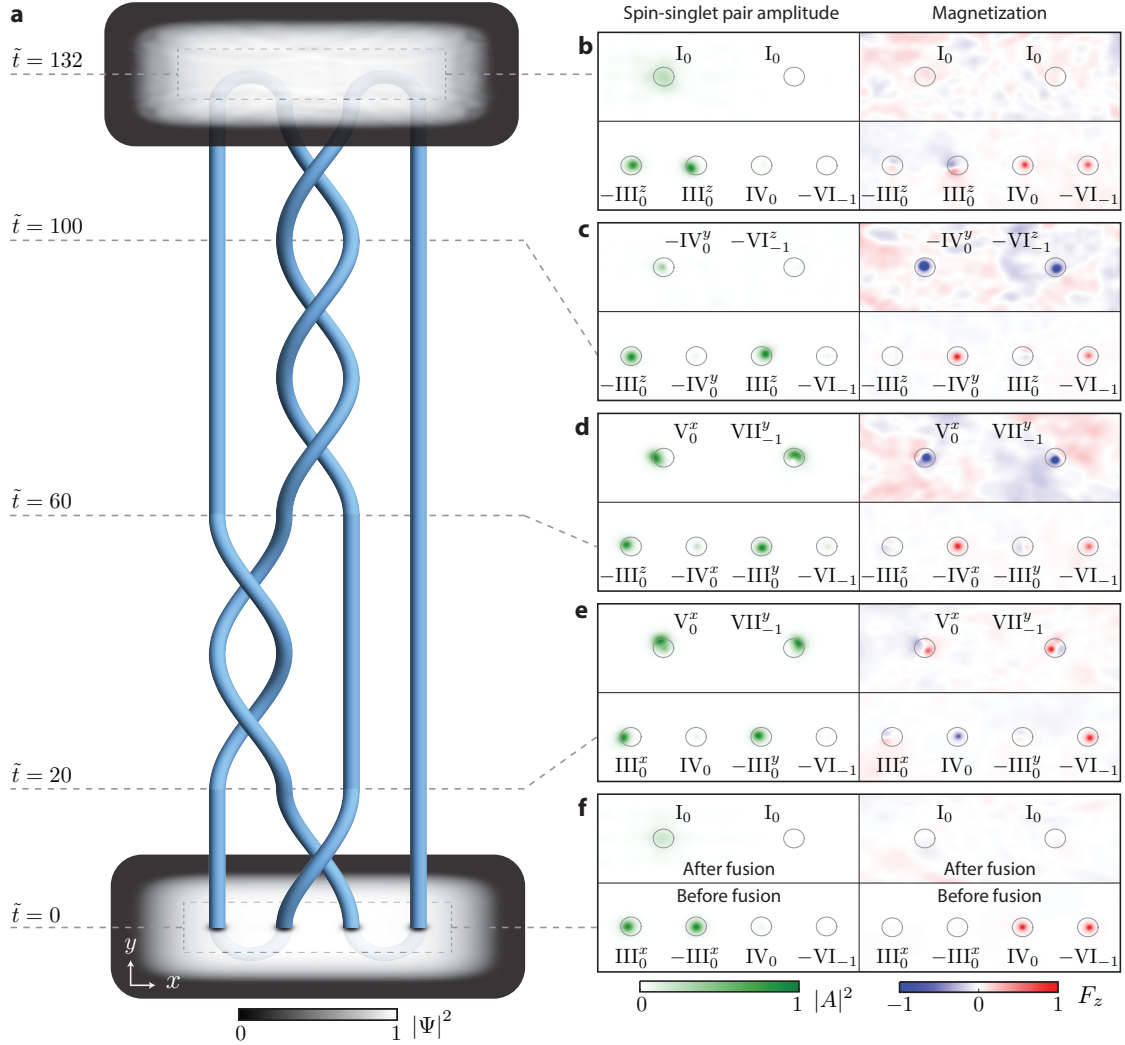


**Figure 5.2:** Braiding and fusion of non-Abelian fractional vortices. **a**, The paths of vortices embedded in a two-dimensional Bose–Einstein condensate trace out world lines that form a braid whose plat closure yields a link L6a2. The total condensate density is shown for the initial ( $\tilde{t} = 0$ ) and final ( $\tilde{t} = 132$ ) states. **b**, Spin-singlet pair amplitude (left column) and magnetization (right column) with vortex locations marked using circles and labelled by the vortex (anyon) types. The upper rows correspond to the system state just after the vortices have been fused pairwise and the lower rows correspond to the state just before the fusion. The field of view of each of the four frames in **b–f** corresponds to the dashed rectangle shown in **a** where the inter-vortex separation is  $27\mu\text{m}$ . The dimensionless times  $\tilde{t} = tw$  of measurement of states **b–f** are marked in **a**.

Underpinning the braiding dynamics is the long-range topological influence between non-Abelian vortices [44, 45, 98]. As we determined in Sec. 2.7, for an anti-clockwise elementary braid (exchange of a pair) of vortices with non-commuting fluxes  $(\gamma_1, \gamma_2)$  their mutual topological influence converts their fluxes to  $(\gamma_2, \gamma_2\gamma_1\gamma_2^{-1})$ , while the clockwise exchange realises the map  $(\gamma_1, \gamma_2) \rightarrow (\gamma_1^{-1}\gamma_2\gamma_1, \gamma_1)$ . Braiding may also enact a local

unitary transformation on the wave function, which reverses the sign of the vortex core magnetisation, turning a red core into a blue core, and vice versa, without changing the value of their fluxes, as shown in Fig. 5.2e and 5.2d. The result of the fusion of each vortex pair is equivalent to the collision dynamics described in Chap. 4. A measurement of the fluxes of each remnant excitation after the fusion is performed using two separate loops with shared base point in the centre of the condensate. These fluxes are then transformed by an equivalency rotation to be consistent with the total flux of the pre-fusion vortex pairs.

The initial vortex-antivortex pairs in Fig. 5.2f (lower row) consist of three particle types; two vortices of same type ( $\text{III}_0$ ) with non-zero  $|A|^2$ , green cores, and two of different types ( $\text{IV}_0$  and  $\text{VI}_{-1}$ ) with  $F_z > 0$ , red cores. Initially, both pairs annihilate upon being fused (Fig. 5.2f, upper row), by construction. An exchange of the two vortices in the middle leads to the state measured at  $\tilde{t} = 20$ , shown in Fig. 5.2e. The braid swaps the positions of two vortices, which trivially changes the pairwise fusion dynamics as neither the green and red, or green and blue, cored vortices can annihilate. The braid between  $\tilde{t} = 60$  and  $\tilde{t} = 100$  consists of two exchanges (elementary braids) of the two middle vortices resulting in the state shown in Fig. 5.2c. Importantly, although this braiding preserves the ordering of the vortex types by returning them to their original pre-braiding positions at  $\tilde{t} = 60$ , the types of vortices formed after fusion are different before ( $\text{V}_0$  and  $\text{VII}_{-1}$  at  $\tilde{t} = 60$ ) and after ( $\text{IV}_0$  and  $\text{VI}_{-1}$  at  $\tilde{t} = 100$ ) the braiding. Such vortex metamorphosis due to braiding is a hallmark of non-Abelian anyons. The final exchange of the middle two vortices results in the state at  $\tilde{t} = 132$ , shown in Fig. 5.2b, where the two non-Abelian vortex anyon pairs again annihilate.

### 5.3. Non-Abelian vortex anyon models

Through a characterisation of all the particle types and their fusion and braiding rules, we can outline a complete anyon model for the non-Abelian vortex anyons in the cyclic-tetrahedral phase of a spin-2 BEC. A complete anyon model for the biaxial nematic phase non-Abelian vortex anyons is also provided in App. D. The cyclic-tetrahedral phase supports 6 non-trivial fluxons and one vacuum state corresponding to the 7 equivalency classes of  $T^*$ , labelled as  $\text{I}_\eta$  -  $\text{VII}_\eta$ . In addition to the fluxons there are chargeons that carry a  $H$ -charge. The centralizers for the fluxon types are  $T^*$  (I, II),  $\mathbb{Z}_4$  (III), and  $\mathbb{Z}_6$  (IV - VII) with 7, 4, and 6 irreducible representations, respectively. For a given  $U(1)$  winding

number, there are 6 non-trivial pure charges (no flux), the same as the 6 pure fluxes. In addition, there are a further 29 dyons (charge-flux composites). Thus in total, the cyclic-tetrahedral phase anyon system has one vacuum state and 41 non-trivial particles comprising 6 fluxons, 6 chargeons, and 29 dyons. Additional fluxons and chargeons are introduced when the  $U(1)$  number is accounted, though many of these particles will behave identically under braiding. The quantum dimension of each anyon is given by a product of the order of the associated equivalency class of its flux with the dimension of the irreducible representation of its charge. The quantum dimension as defined here similarly satisfies the relation in Eq. (2.34). In this work, unless otherwise stated, our focus is only on the fluxons of the theory and their fusion and braiding dynamics.

The fusion outcomes of the lowest energy fluxons are determined by the group algebra of  $H = T^*$ , following the composition rule  $(\pm X_\eta^\alpha)(\pm Y_\nu^\beta) = (\eta + a_X + \nu + a_Y, g_X^\alpha g_Y^\beta)$ . As a result, their flux-level fusion rules can be determined directly from the fusion table, which is presented in Figure 5.3. Although the type  $IV_\eta - VII_\eta$  vortices are non-Abelian anyons, their fusion rules do not preserve the winding number  $\eta$  of the anyons, complicating their potential use for topological quantum computation. However, restricting to the set of three fluxons  $I_0$ ,  $II_0$  and  $III_0$ , hereafter referred to as  $\mathbf{1}$ ,  $\sigma$ , and  $\tau$ , respectively, results in a concise non-Abelian anyon model. For example, the fusion of two fluxes of the  $\tau$  ( $III_0$ ) anyon can produce a flux of the  $\mathbf{1}$  ( $I_0$ ),  $\sigma$  ( $II_0$ ), or  $\tau$  ( $III_0$ ) anyon and hence

$$\tau \otimes \tau = N_{\tau\tau}^{\mathbf{1}} \mathbf{1} \oplus N_{\tau\tau}^{\sigma} \sigma \oplus N_{\tau\tau}^{\tau} \tau. \quad (5.2)$$

The multiplicities are determined as the number of distinct factorizations of the fluxes of each outcome into products of  $\tau$  anyon fluxes, equivalent to considering the reverse process where an anyon  $c$  splits into anyons  $a$  and  $b$  in  $N_c^{ab} = N_{ab}^c$  ways. Hence, the multiplicities are  $N_{\tau\tau}^{\mathbf{1}} = 6$ ,  $N_{\tau\tau}^{\sigma} = 6$ , and  $N_{\tau\tau}^{\tau} = 4$ . The fusion rules for all the cyclic-tetrahedral phase non-Abelian vortex anyons are given at the flux-level in Table 5.1. The remaining flux fusion rules of this anyon model are;  $\tau \otimes \sigma = \tau$ ,  $\sigma \otimes \sigma = \mathbf{1}$  and  $x \otimes \mathbf{1} = x$ , where  $x \in \{\mathbf{1}, \sigma, \tau\}$ . The anyons  $\mathbf{1}$  and  $\sigma$  are Abelian with quantum dimensions  $d_{\mathbf{1}} = d_{\sigma} = 1$ , respectively. The  $\tau$  anyon is the non-Abelian (fluxon) anyon of the theory with a quantum dimension,  $d_{\tau} = 6$ , larger than both the Fibonacci and Ising anyon models.

A·B	$I_0$	$-II_0$	$III_0^+$	$III_0^+$	$III_0^+$	$-III_0^+$	$-III_0^+$	$-III_0^+$	$IV_0$	$-IV_0^+$	$-IV_0^+$	$-IV_0^+$	$-V_0$	$V_0^+$	$V_0^+$	$V_0^+$	$-VI_{-1}$	$-VI_{-1}$	$-VI_{-1}$	$-VI_{-1}$	$VII_{-1}$	$VII_{-1}$	$VII_{-1}^+$	$VII_{-1}^+$
$I_0$	$I_0$	$-II_0$	$III_0^+$	$III_0^+$	$III_0^+$	$-III_0^+$	$-III_0^+$	$-III_0^+$	$IV_0$	$-IV_0^+$	$-IV_0^+$	$-IV_0^+$	$-V_0$	$V_0^+$	$V_0^+$	$V_0^+$	$-VI_{-1}$	$-VI_{-1}$	$-VI_{-1}$	$-VI_{-1}$	$VII_{-1}$	$VII_{-1}$	$VII_{-1}^+$	$VII_{-1}^+$
$-II_0$	$-II_0$	$I_0$	$-III_0^+$	$-III_0^+$	$-III_0^+$	$III_0^+$	$III_0^+$	$III_0^+$	$-V_0$	$V_0^+$	$V_0^+$	$V_0^+$	$IV_0$	$-IV_0^+$	$-IV_0^+$	$-IV_0^+$	$VII_{-1}$	$VII_{-1}$	$VII_{-1}^+$	$VII_{-1}^+$	$-VI_{-1}$	$-VI_{-1}$	$-VI_{-1}^+$	$-VI_{-1}^+$
$III_0^+$	$III_0^+$	$-III_0^+$	$-II_0$	$III_0^+$	$-III_0^+$	$I_0$	$-III_0^+$	$III_0^+$	$V_0^+$	$-IV_0^+$	$V_0^+$	$IV_0$	$-IV_0^+$	$V_0^+$	$-IV_0^+$	$-V_0$	$-VII_{-1}$	$VII_{-1}$	$VII_{-1}$	$-VI_{-1}$	$VII_{-1}^+$	$-VI_{-1}$	$-VI_{-1}$	$VII_{-1}^+$
$III_0^+$	$III_0^+$	$-III_0^+$	$III_0^+$	$-II_0$	$III_0^+$	$III_0^+$	$I_0$	$-III_0^+$	$V_0^+$	$V_0^+$	$IV_0$	$-IV_0^+$	$-IV_0^+$	$-V_0$	$V_0^+$	$-VII_{-1}$	$VII_{-1}$	$-VI_{-1}$	$VII_{-1}^+$	$VII_{-1}$	$-VI_{-1}$	$VII_{-1}^+$	$-VI_{-1}$	$-VII_{-1}$
$III_0^+$	$III_0^+$	$-III_0^+$	$III_0^+$	$-II_0$	$III_0^+$	$III_0^+$	$I_0$	$-III_0^+$	$V_0^+$	$V_0^+$	$IV_0$	$-IV_0^+$	$-IV_0^+$	$-V_0$	$V_0^+$	$-VII_{-1}$	$VII_{-1}$	$-VI_{-1}$	$VII_{-1}^+$	$VII_{-1}$	$-VI_{-1}$	$VII_{-1}^+$	$-VI_{-1}$	$-VII_{-1}$
$-III_0^+$	$-III_0^+$	$III_0^+$	$I_0$	$-III_0^+$	$III_0^+$	$-II_0$	$III_0^+$	$-III_0^+$	$-IV_0^+$	$V_0^+$	$-IV_0^+$	$-V_0$	$V_0^+$	$-IV_0^+$	$V_0^+$	$IV_0$	$VII_{-1}^+$	$-VI_{-1}$	$-VI_{-1}$	$VII_{-1}^+$	$-VI_{-1}$	$VII_{-1}^+$	$-VI_{-1}$	$-VII_{-1}$
$-III_0^+$	$-III_0^+$	$III_0^+$	$III_0^+$	$I_0$	$-III_0^+$	$-III_0^+$	$-II_0$	$III_0^+$	$-IV_0^+$	$-V_0$	$V_0^+$	$-IV_0^+$	$V_0^+$	$IV_0$	$-IV_0^+$	$V_0^+$	$VII_{-1}^+$	$VII_{-1}^+$	$-VI_{-1}$	$-VI_{-1}$	$-VI_{-1}$	$-VI_{-1}$	$VII_{-1}^+$	$VII_{-1}$
$-III_0^+$	$-III_0^+$	$III_0^+$	$-III_0^+$	$III_0^+$	$I_0$	$III_0^+$	$-III_0^+$	$-II_0$	$-IV_0^+$	$-IV_0^+$	$-V_0$	$V_0^+$	$V_0^+$	$IV_0$	$-IV_0^+$	$V_0^+$	$VII_{-1}^+$	$-VI_{-1}$	$VII_{-1}^+$	$-VI_{-1}$	$-VI_{-1}$	$VII_{-1}$	$-VI_{-1}$	$VII_{-1}^+$
$IV_0$	$IV_0$	$-V_0$	$V_0^+$	$V_0^+$	$V_0^+$	$-IV_0^+$	$-IV_0^+$	$-IV_0^+$	$VII_0$	$-VII_0$	$-VII_0$	$-VII_0$	$-VI_0$	$VII_0$	$VII_0$	$VII_0$	$I_0$	$III_0^+$	$III_0^+$	$III_0^+$	$-II_0$	$-III_0^+$	$-III_0^+$	$-III_0^+$
$-IV_0^+$	$-IV_0^+$	$V_0^+$	$IV_0$	$-IV_0^+$	$V_0^+$	$-V_0$	$V_0^+$	$-IV_0^+$	$-VII_0$	$VII_0$	$-VII_0$	$-VI_0$	$VII_0$	$-VII_0$	$VII_0$	$VII_0$	$-III_0^+$	$III_0^+$	$I_0$	$-III_0^+$	$III_0^+$	$-III_0^+$	$-II_0$	$III_0^+$
$-IV_0^+$	$-IV_0^+$	$V_0^+$	$V_0^+$	$IV_0$	$-IV_0^+$	$-IV_0^+$	$-V_0$	$V_0^+$	$-VII_0$	$-VII_0$	$VII_0$	$-VII_0$	$VII_0$	$-VII_0$	$VII_0$	$VII_0$	$-III_0^+$	$-III_0^+$	$III_0^+$	$I_0$	$III_0^+$	$III_0^+$	$-III_0^+$	$-II_0$
$-IV_0^+$	$-IV_0^+$	$V_0^+$	$-IV_0^+$	$V_0^+$	$IV_0$	$V_0^+$	$-IV_0^+$	$-V_0$	$-VII_0$	$-VII_0$	$VII_0$	$-VII_0$	$VII_0$	$-VII_0$	$VII_0$	$VII_0$	$-III_0^+$	$I_0$	$-III_0^+$	$III_0^+$	$III_0^+$	$-II_0$	$III_0^+$	$-III_0^+$
$-V_0$	$-V_0$	$IV_0$	$-IV_0^+$	$-IV_0^+$	$-IV_0^+$	$V_0^+$	$V_0^+$	$V_0^+$	$-VI_0$	$VII_0$	$VII_0$	$VII_0$	$VII_0$	$-VII_0$	$-VII_0$	$-VII_0$	$-II_0$	$-III_0^+$	$-III_0^+$	$-III_0^+$	$I_0$	$III_0^+$	$III_0^+$	$III_0^+$
$V_0^+$	$V_0^+$	$-IV_0^+$	$-V_0$	$V_0^+$	$-IV_0^+$	$IV_0$	$-IV_0^+$	$V_0^+$	$VII_0$	$-VII_0$	$VII_0$	$VII_0$	$-VII_0$	$VII_0$	$-VII_0$	$-VII_0$	$III_0^+$	$-III_0^+$	$-II_0$	$III_0^+$	$-III_0^+$	$III_0^+$	$I_0$	$-III_0^+$
$V_0^+$	$V_0^+$	$-IV_0^+$	$-IV_0^+$	$-V_0$	$V_0^+$	$V_0^+$	$IV_0$	$-IV_0^+$	$VII_0$	$VII_0$	$-VII_0$	$-VII_0$	$-VI_0$	$VII_0$	$-VII_0$	$-VII_0$	$III_0^+$	$III_0^+$	$-III_0^+$	$-II_0$	$-III_0^+$	$-III_0^+$	$III_0^+$	$I_0$
$V_0^+$	$V_0^+$	$-IV_0^+$	$V_0^+$	$-IV_0^+$	$-V_0$	$-IV_0^+$	$V_0^+$	$IV_0$	$VII_0$	$VII_0$	$VII_0$	$-VII_0$	$-VII_0$	$-VII_0$	$-VII_0$	$-VII_0$	$III_0^+$	$-II_0$	$III_0^+$	$-III_0^+$	$-III_0^+$	$I_0$	$-III_0^+$	$III_0^+$
$-VI_{-1}$	$-VI_{-1}$	$VII_{-1}$	$-VII_{-1}$	$-VII_{-1}$	$-VII_{-1}$	$VII_{-1}^+$	$VII_{-1}^+$	$VII_{-1}^+$	$I_0$	$-III_0^+$	$-III_0^+$	$-III_0^+$	$-II_0$	$III_0^+$	$III_0^+$	$III_0^+$	$-V_{-1}$	$-IV_{-1}^+$	$-IV_{-1}^+$	$-IV_{-1}^+$	$IV_{-1}$	$V_{-1}^+$	$V_{-1}^+$	$V_{-1}^+$
$-VII_{-1}$	$-VII_{-1}$	$VII_{-1}^+$	$VII_{-1}$	$-VII_{-1}$	$-VII_{-1}$	$-VII_{-1}$	$-VII_{-1}$	$-VII_{-1}$	$III_0^+$	$-III_0^+$	$III_0^+$	$I_0$	$-III_0^+$	$III_0^+$	$-III_0^+$	$-II_0$	$-IV_{-1}^+$	$V_{-1}^+$	$IV_{-1}$	$-IV_{-1}^+$	$V_{-1}^+$	$-IV_{-1}$	$-V_{-1}$	$V_{-1}^+$
$-VII_{-1}$	$-VII_{-1}$	$VII_{-1}^+$	$VII_{-1}$	$VII_{-1}$	$-VII_{-1}$	$-VII_{-1}$	$-VII_{-1}$	$-VII_{-1}$	$III_0^+$	$I_0$	$-III_0^+$	$III_0^+$	$-III_0^+$	$-II_0$	$III_0^+$	$-III_0^+$	$-IV_{-1}^+$	$-IV_{-1}^+$	$V_{-1}^+$	$IV_{-1}$	$V_{-1}^+$	$-IV_{-1}$	$-V_{-1}$	$-V_{-1}$
$-VII_{-1}$	$-VII_{-1}$	$VII_{-1}^+$	$-VII_{-1}$	$VII_{-1}$	$VII_{-1}$	$VII_{-1}$	$-VII_{-1}$	$-VII_{-1}$	$III_0^+$	$III_0^+$	$I_0$	$-III_0^+$	$-III_0^+$	$-III_0^+$	$-II_0$	$III_0^+$	$-IV_{-1}^+$	$IV_{-1}$	$-IV_{-1}^+$	$V_{-1}^+$	$V_{-1}^+$	$-V_{-1}$	$V_{-1}^+$	$-IV_{-1}^+$
$VII_{-1}$	$VII_{-1}$	$-VII_{-1}$	$VII_{-1}^+$	$VII_{-1}^+$	$VII_{-1}^+$	$-VII_{-1}$	$-VII_{-1}$	$-VII_{-1}$	$-II_0$	$III_0^+$	$III_0^+$	$III_0^+$	$I_0$	$-III_0^+$	$-III_0^+$	$-III_0^+$	$IV_{-1}$	$V_{-1}^+$	$V_{-1}^+$	$V_{-1}^+$	$-V_{-1}$	$-IV_{-1}^+$	$-IV_{-1}^+$	$-IV_{-1}^+$
$VII_{-1}$	$VII_{-1}$	$-VII_{-1}$	$-III_0^+$	$III_0^+$	$-III_0^+$	$-II_0$	$III_0^+$	$-III_0^+$	$III_0^+$	$I_0$	$V_{-1}^+$	$-IV_{-1}^+$	$-V_{-1}$	$V_{-1}^+$	$-IV_{-1}^+$	$V_{-1}^+$	$IV_{-1}$	$-IV_{-1}^+$						
$VII_{-1}$	$VII_{-1}$	$-VII_{-1}$	$-III_0^+$	$-II_0$	$III_0^+$	$-III_0^+$	$III_0^+$	$I_0$	$-III_0^+$	$III_0^+$	$V_{-1}^+$	$V_{-1}^+$	$-IV_{-1}^+$	$-V_{-1}$	$-IV_{-1}^+$	$-IV_{-1}^+$	$V_{-1}^+$	$IV_{-1}$						
$VII_{-1}$	$VII_{-1}$	$-VII_{-1}$	$VII_{-1}^+$	$-VII_{-1}$	$-VII_{-1}$	$-VII_{-1}$	$-VII_{-1}$	$-VII_{-1}$	$-III_0^+$	$-III_0^+$	$-II_0$	$III_0^+$	$III_0^+$	$I_0$	$-III_0^+$	$-III_0^+$	$-V_{-1}$	$-V_{-1}$	$V_{-1}^+$	$-IV_{-1}^+$	$-IV_{-1}^+$	$-IV_{-1}^+$	$-IV_{-1}^+$	$V_{-1}^+$

**Figure 5.3:** Fusion table for the topological charges of the cyclic-tetrahedral phase non-Abelian vortex anyons. The product  $A \cdot B$  is ordered with  $A$  corresponding to the top row and  $B$  to the first column. The thick cell borders divide the regions of each anyon fusion rule. The background colour of each cell signifies the anyon type with the intensity of the shading highlighting the winding number  $\eta$ .

**Table 5.1:** Fusion rules  $a \otimes b$  at flux level for the non-Abelian vortex anyons in the cyclic-tetrahedral phase. The concise anyon model discussed in the text is highlighted.

	$I_0$	$II_0$	$III_0$	$IV_0$	$V_0$	$VI_{-1}$	$VII_{-1}$
$1 = I_0$	$I_0$	$II_0$	$III_0$	$IV_0$	$V_0$	$VI_{-1}$	$VII_{-1}$
$\sigma = II_0$	$II_0$	$I_0$	$III_0$	$V_0$	$IV_0$	$VII_{-1}$	$VI_{-1}$
$\tau = III_0$	$III_0$	$III_0$	$6I_0 \oplus 6II_0 \oplus 4III_0$	$3IV_0 \oplus 3V_0$	$3IV_0 \oplus 3V_0$	$3VI_{-1} \oplus 3VII_{-1}$	$3VI_{-1} \oplus 3VII_{-1}$
$IV_0$	$IV_0$	$V_0$	$3IV_0 \oplus 3V_0$	$3VI_0 \oplus VII_0$	$VI_0 \oplus 3VII_0$	$4I_0 \oplus 2III_0$	$4II_0 \oplus 2III_0$
$V_0$	$V_0$	$IV_0$	$3IV_0 \oplus 3V_0$	$VI_0 \oplus 3VII_0$	$3VI_0 \oplus VII_0$	$4II_0 \oplus 2III_0$	$4I_0 \oplus 2III_0$
$VI_{-1}$	$VI_{-1}$	$VII_{-1}$	$3VI_{-1} \oplus 3VII_{-1}$	$4I_0 \oplus 2III_0$	$4II_0 \oplus 2III_0$	$3IV_{-1} \oplus V_{-1}$	$IV_{-1} \oplus 3V_{-1}$
$VII_{-1}$	$VII_{-1}$	$VI_{-1}$	$3VI_{-1} \oplus 3VII_{-1}$	$4II_0 \oplus 2III_0$	$4I_0 \oplus 2III_0$	$IV_{-1} \oplus 3V_{-1}$	$3IV_{-1} \oplus V_{-1}$

The multiplicities are accounted for by the  $H$ -charges, resulting in richer fusion rules. Considering the  $\tau$  fluxon anyon model summarised in Table 5.1 the charge inclusive fusion rules are:

$$\mathbf{1}_{T0}^{(1)} \otimes \mathbf{1}_{T0}^{(1)} = \mathbf{1}_{T0}^{(1)}, \quad \mathbf{1}_{T0}^{(1)} \otimes \sigma_{T0}^{(1)} = \sigma_{T0}^{(1)}, \quad \mathbf{1}_{T0}^{(1)} \otimes \tau_{Z0}^{(1)} = \tau_{Z0}^{(1)}, \quad (5.3)$$

$$\sigma_{T0}^{(1)} \otimes \sigma_{T0}^{(1)} = \mathbf{1}_{T0}^{(1)}, \quad \sigma_{T0}^{(1)} \otimes \tau_{Z0}^{(1)} = \tau_{Z0}^{(1)}, \quad (5.4)$$

and

$$\begin{aligned} \tau_{Z0}^{(1)} \otimes \tau_{Z0}^{(1)} = & \mathbf{1}_{T0}^{(1)} \oplus \mathbf{1}_{T1}^{(1)} \oplus \mathbf{1}_{T2}^{(1)} \oplus \mathbf{1}_{T3}^{(3)} \oplus \\ & \sigma_{T0}^{(1)} \oplus \sigma_{T1}^{(1)} \oplus \sigma_{T2}^{(1)} \oplus \sigma_{T3}^{(3)} \oplus \\ & 2\tau_{Z0}^{(1)} \oplus 2\tau_{Z2}^{(1)}, \end{aligned} \quad (5.5)$$

where in the above anyon notation  $\tau_c^{(d)}$  the subscript denotes the  $H$ -charge of the anyon and the superscript denotes the quantum dimension of the charge. Here  $Zi$  and  $Ti$  refer to the irreducible representations of the centralizers  $\mathbb{Z}_4$  and  $T^*$ , respectively. The particles  $\mathbf{1}_{T0}^{(1)}$ ,  $\sigma_{T0}^{(1)}$  and  $\tau_{Z0}^{(1)}$  are equivalent to the fluxons  $I_0$ ,  $\Pi_0$  and  $\text{III}_0$ , respectively. The physical content of Eq. (5.5) is thus that the fusion of two  $\tau$  type fluxons on the left may result in an annihilation to a true vacuum, in either of the two fluxons, one of three chargeons or one of six dyons. It is implicitly understood that charge conservation is maintained in the fusion rules by the presence of Cheshire charge as a delocalized property of initial  $\tau$  fluxon pair. The Cheshire charge states given by the  $Ti$  chargeons (eigenstates) in Eq. (5.5) may be expressed in terms of a quantum superposition of  $\tau$  flux eigenstates as

$$\begin{aligned} |T0, \mathbf{1}\rangle &= \frac{1}{\sqrt{6}}[\tau_x\tau_{\bar{x}} + \tau_{\bar{x}}\tau_x + \tau_y\tau_{\bar{y}} + \tau_{\bar{y}}\tau_y + \tau_z\tau_{\bar{z}} + \tau_{\bar{z}}\tau_z], \\ |T1, \mathbf{1}\rangle &= \frac{1}{\sqrt{6}}[\tau_x\tau_{\bar{x}} + \tau_{\bar{x}}\tau_x + \theta(\tau_y\tau_{\bar{y}} + \tau_{\bar{y}}\tau_y) + \theta^*(\tau_z\tau_{\bar{z}} + \tau_{\bar{z}}\tau_z)], \\ |T2, \mathbf{1}\rangle &= \frac{1}{\sqrt{6}}[\tau_x\tau_{\bar{x}} + \tau_{\bar{x}}\tau_x + \theta^*(\tau_y\tau_{\bar{y}} + \tau_{\bar{y}}\tau_y) + \theta(\tau_z\tau_{\bar{z}} + \tau_{\bar{z}}\tau_z)], \\ |T3, \mathbf{1}\rangle &= \frac{1}{\sqrt{2}}\{(\tau_x\tau_{\bar{x}} - \tau_{\bar{x}}\tau_x), (\tau_y\tau_{\bar{y}} - \tau_{\bar{y}}\tau_y), (\tau_z\tau_{\bar{z}} - \tau_{\bar{z}}\tau_z)\}, \end{aligned} \quad (5.6)$$

where  $\mathbf{1}$  is the total flux,  $\theta = e^{i2\pi/3}$  and the notation  $\tau_x\tau_{\bar{x}}$  is a flux eigenstate corresponding to a spinor hosting two vortices,  $\text{III}_0^x$  and  $-\text{III}_0^x$ . The flux eigenstates represent true macroscopic quantum superposition states of a spinor Bose–Einstein condensate, which

can not be constructed as a superposition of the usual classical mean-field theory spinor wave functions. Equation (5.6) can similarly describe the  $\sigma$  dyons after trivially replacing the  $\tau$  vortex pair fluxes with those fusing to  $\Pi_0$ . The Cheshire charges of the  $\tau$  dyons are

$$\begin{aligned} |Z0, \tau\rangle_z &= \frac{1}{\sqrt{2}}\{\tau_x\tau_{\bar{y}} + \tau_{\bar{x}}\tau_y\}, \frac{1}{\sqrt{2}}\{\tau_y\tau_x + \tau_{\bar{y}}\tau_{\bar{x}}\}, \\ |Z2, \tau\rangle_z &= \frac{1}{\sqrt{2}}\{\tau_x\tau_{\bar{y}} - \tau_{\bar{x}}\tau_y\}, \frac{1}{\sqrt{2}}\{\tau_y\tau_x - \tau_{\bar{y}}\tau_{\bar{x}}\}, \end{aligned} \quad (5.7)$$

where  $\tau_x\tau_{\bar{y}}$  corresponds to a spinor hosting two vortices,  $\text{III}_0^x$  and  $-\text{III}_0^y$ , which fuse to the vortex  $\text{III}_0^z$ . Each Cheshire charge is described by two different basis states. One relatively simple way to infer these Cheshire charge states, without employing the quantum double  $D(H)$ , is to consider the action of braiding a fluxon pair with Cheshire charge, represented by a superposition of flux eigenstates, with the fluxes corresponding to the elements of the centralizer group of the total charge of the fluxon pair. This action is represented in Fig. 5.1. As an example, consider the  $\tau$  fluxon pair fusing to the vacuum flux, represented by the superposition of flux eigenstates in Eq. (5.6). The centralizer is  $T^*$  and thus the braid conjugates each flux in the fluxon pairs by the particular element  $\gamma \in T^*$ . This action is equivalent to the flux  $\gamma$  acting on the charge (Cheshire)  $\alpha$  by the matrix  $\alpha(\gamma)$ , which is the group element  $\gamma$  in the irreducible representation  $\alpha$ . For the charge  $|\text{T}0, \mathbf{1}\rangle$ , corresponding to the trivial representation of  $T^*$ ,  $\alpha(\gamma) = 1$  for every  $\gamma \in T^*$ . Hence, the superposition must contain only trivial phases. Comparatively, for the charge  $|\text{T}1, \mathbf{1}\rangle$ , which is one of the non-trivial one-dimensional representations of  $T^*$ , the  $\alpha(\gamma)$  can be determined directly from the character table, see App. C, as  $\alpha(\text{I, II, III}) = 1$ ,  $\alpha(\text{IV, V}) = \theta$  and  $\alpha(\text{VI, VII}) = \theta^*$ ; where the  $\gamma$  are given in terms of their flux type. Hence, the  $|\text{T}1, \mathbf{1}\rangle$  superposition must contain the non-trivial phase  $\theta$  and its conjugate.

The result of fusing two chargeons is determined from the tensor product of their representations, which can be calculated from the character table as described in App. C. The fusion of dyons is more complex as it involves the centralizer groups of the fluxes. Nevertheless, all fusions can be calculated using the tensor product decomposition of the representations of the quantum double  $D(H)$  of  $H$ . This can be done efficiently using the characters of  $D(H)$  [225]. The fusion rules of the remaining chargeons and dyons in the  $\tau$  anyon model are presented in Appendix E.

In addition to the cyclic-tetrahedral phase  $\tau$  anyon model, the biaxial nematic phase additionally supports two concise non-Abelian anyon models, for the full details see Appendix D.

## 5.4. Topological qubit of non-Abelian vortices

As discussed in Sec. 2.8, the different fusion outcomes of anyons define a fusion path, equivalent to a set of topologically distinct states, which can be used for encoding quantum information. Furthermore, in Sec. 2.9 we explored the construction of a topological qubit using the non-Abelian anyons in Fibonacci anyon model. In that case the fusion paths of three Fibonacci  $\tau$  anyons define a two-level system, corresponding to the two states in the fusion space  $V_{\tau\tau\tau}^\tau$ , plus one non-computational state. Comparatively, the fusion of three of our  $\tau$  fluxons results in some 52 distinct fusion paths in which information could be stored, a result of the  $H$ -charges in the system. This is significantly larger than number of states in the Fibonacci anyon model case. Nevertheless, for the sake of demonstration, we consider braiding operations with three fluxons that involve only a subset of the many states in the full fusion space  $V_{\tau z_0 \tau z_0 \tau z_0}^{\tau z_0}$  and may therefore be conveniently discussed in terms of effective qubits. A natural choice for the zero state corresponds to the creation of two pairs of  $\tau$  fluxons from the true vacuum. The rightmost of the four anyons will not be part of the qubit and will not take part in any braiding processes we consider. Therefore its flux will not be mentioned explicitly in the qubit's state. The zero state of the qubit is then  $|0\rangle = \frac{1}{6} \sum_{\gamma_1, \gamma_2 \in \text{III}} |\gamma_1, \gamma_1^{-1}, \gamma_2\rangle$ , corresponding to three  $\tau$  anyons with fluxes  $\gamma_1, \gamma_1^{-1}$  and  $\gamma_2$  respectively. A convenient choice for the second qubit state is  $|1\rangle = \frac{1}{6} \sum_{\gamma_1, \gamma_2 \in \text{III}} |\gamma_1, \gamma_1, \gamma_2\rangle$ , corresponding to the fusion of the leftmost  $\tau$  fluxon pair to the  $\sigma$  fluxon.

Figure 5.4 demonstrates the action of manipulating the state of such a topological qubit by controllable braiding of the anyons. Initially, the fluxons are prepared in such a way that the first two of them are guaranteed to annihilate upon fusion, as in the  $|0\rangle$  state, which in practice could be achieved by nucleating two vortex-antivortex pairs that introduces a fourth, surplus, anyon which is disregarded in this numerical experiment without consequence.

A unitary operation, encoded by the braid in Fig. 5.4a, is applied to the fluxons by moving the vortices with the pinning potentials to exchange the second and third anyons within the qubit structure twice. Once the braiding has been completed, a measurement of the state is made by fusing the first and second anyons from the left of the condensate and observing the remaining core structures shortly after the pinning potentials have been withdrawn. Prior to the fusion the three  $\tau$  anyons are identified by the green  $|A|^2$  cores, as shown in Fig. 5.4b and e, where in Fig. 5.4b-d we have applied thresholding to represent a binary measurement protocol. After the braiding, the measurement outcome

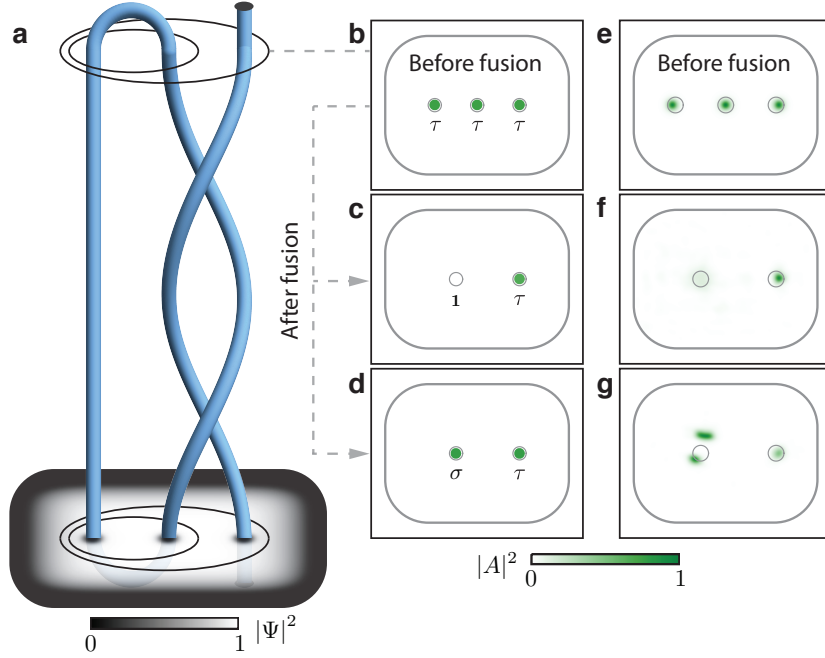


**Figure 5.4:** Single qubit braiding operation. **a**, The paths of the three  $\tau$  anyons trace out braided world lines enacting a unitary operation on the initial state. Time flows upward. The total condensate density is shown for the initial state. The overlaid concentric ellipses denote the orientation of the qubit as a graphical representation of the bracket notation used in the text. **b**, Spin-singlet pair amplitude of the qubit just before the fusion. The rounded rectangle marks the boundary of the condensate and the vortex locations are denoted by the circles, the inter-vortex separation is  $27\mu\text{m}$ . **c**, a fusion outcome corresponding to the annihilation of the first two anyons as in the  $|0\rangle$  state. **d**, a fusion outcome corresponding to the non-annihilation of the first two anyons as in the  $|1\rangle$  state. Data in **b-d** are thresholded relative to half the maximum value in **b** and any maxima within the vortex location markers are mapped to the solid green circles. **e-g**, Raw data for **b-d** without thresholding. The specific fluxes of the three initial state vortices in (c) are  $(\text{III}_0^x, -\text{III}_0^x, \text{III}_0^x)$  and in (d) they are  $(\text{III}_0^x, -\text{III}_0^x, \text{III}_0^y)$ .

depends on the topological influence between the exchanged anyons. The braid maps the  $|0\rangle$  state to a superposition

$$\sum_{\substack{\gamma_1, \gamma_2 \in \text{III} \\ \gamma_1 \gamma_2 = \gamma_2 \gamma_1}} \frac{|\gamma_1, \gamma_1^{-1}, \gamma_2\rangle}{2\sqrt{3}} + \sum_{\substack{\gamma_1, \gamma_2 \in \text{III} \\ \gamma_1 \gamma_2 \neq \gamma_2 \gamma_1}} \frac{|\gamma_1, \gamma_1, \gamma_2\rangle}{2\sqrt{6}}, \quad (5.8)$$

where the two sums contain the combinations of fluxes which braided with trivial and non-trivial topological influence, respectively. The probability  $p$  that a measurement would record complete annihilation  $p(0) = 1/3$  or the formation of a  $\sigma$  fluxon  $p(1) = 2/3$  after the braiding is obtained by projecting the braided superposition state onto the two qubit basis states  $|0\rangle$  and  $|1\rangle$ . Prior to the fusion measurement the two possibilities are indistinguishable by any local observation. In general, braiding with respect to this basis

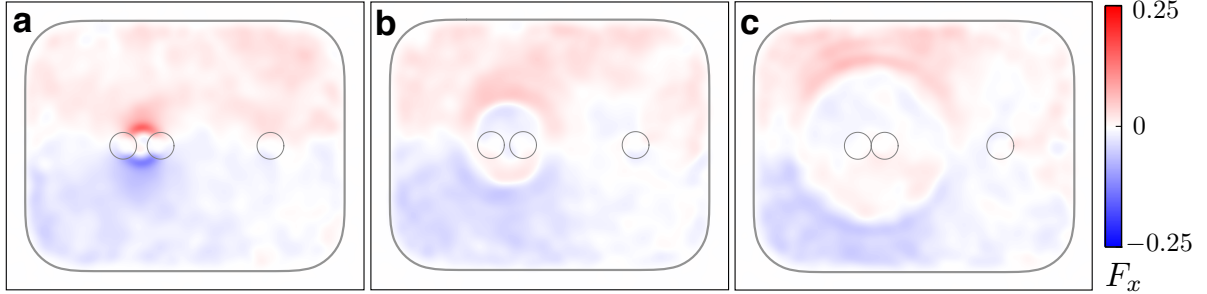


**Figure 5.5:** Signatures of a Cheshire charge. Frames (a)-(c) show the  $x$ -component of the magnetization density of the condensate at the end of the simulation of Fig. 5.4(c). The time interval between the frames is  $\delta t \approx 16\text{ms}$ . The circular markers denote the locations of the vortex pinning sites. The expanding ring shaped magnetic soliton structure is emitted due to the fusion of two fluxons.

would introduce significant leakage into the non-computable fusion paths even for the case of a single qubit. However this is not a real problem as we only restricted to a two dimensional space for illustrative purposes. Any realistic implementation would use the full fusion space for computations.

The numerical experiments are based on classical mean-field theory and thus can not simulate true quantum superpositions. As such, we simulate two specific components of the  $|0\rangle$  state, those with fluxes  $(III_0^x, -III_0^x, III_0^x)$  and  $(III_0^x, -III_0^x, III_0^y)$  and the braid acts on these basis states in a deterministic manner. In the first case the exchanged anyons commute so the braid realises a trivial topological influence and the fusion measures the  $|0\rangle$  state, shown in Fig. 5.4c, characterised by a single green core. However, in the latter case they do not commute so the non-trivial topological influence changes the signs of the anyons and the fusion measures the state  $|1\rangle$  of the topological qubit. Such a measurement of the  $|1\rangle$  state is illustrated in Fig. 5.4d and corresponds to the observation of two green vortex cores, with the additional filled core corresponding to a  $\sigma$  anyon formed in the fusion of the two  $\tau$  anyons.

We have discussed the topological qubit at the fluxon level, ignoring the  $H$ -charges. However, the states considered in the single qubit simulations are  $\tau$  flux eigenstates, which correspond to charge superposition states. Here the charge arises as Cheshire charge [219, 220, 226], which may be revealed when the vortices are annihilated causing the delocalized Cheshire charge to appear. Representations for the four pure (Cheshire)  $H$ -charge states that may result from the annihilation of two type  $\tau$  fluxons are given in Eq. (5.6). After a Cheshire charge localises to a  $H$ -charge, it could reform as a pair of *Alice vortices* or a propagating *Alice ring* [220]. In our single qubit simulations we

have observed a propagating ring-shaped soliton structure in the magnetisation density of the condensate, Fig. 5.5(a-c), which may have been emitted from a potential Cheshire charge. The magnetic soliton may be an observable signature of Cheshire charge in our system. Cheshire charge has also been noted to arise in spinor condensates in the context of a monopole point-defect decaying to a half-quantum vortex ring, also known as an Alice ring [137, 227]. After the decay the monopole charge is conserved as a form of a delocalized topological charge associated with the Alice ring.

## 5.5. Implementing two qubit unitary operations

It is straightforward to extend the creation and manipulation of single flux qubits to multiple topological qubits. Figure 5.6 demonstrates the action of a unitary braiding operation on two topological qubits comprising six  $\tau$  anyons. We consider a initial state  $|00\rangle = \frac{1}{12} \sum_{\gamma_{11}, \gamma_{21}, \gamma_{12}, \gamma_{22} \in \text{III}} |\gamma_{11}, \gamma_{11}^{-1}, \gamma_{21}; \gamma_{12}, \gamma_{12}^{-1}, \gamma_{22}\rangle$ , corresponding to both qubits starting in the  $|0\rangle$  state. The full braid, shown in Fig. 5.6a, causes an intertwining of the two qubits by tying a topologically non-trivial link in their anyon world lines. The topologically trivial operations in Fig. 5.6a (greyed out) only alter the relative orientation of the two qubits and will have no effect on the fusion outcome. The braid maps the  $|00\rangle$  state to a superposition

$$\sum_{\substack{\gamma_{11}, \gamma_{21}, \gamma_{12}, \gamma_{22} \in \text{III} \\ \gamma_{11} \gamma_{12} = \gamma_{12} \gamma_{11}}} \frac{|\gamma_{11}, \gamma_{11}^{-1}, \gamma_{21}; \gamma_{12}, \gamma_{12}^{-1}, \gamma_{22}\rangle}{12\sqrt{3}} + \sum_{\substack{\gamma_{11}, \gamma_{21}, \gamma_{12}, \gamma_{22} \in \text{III} \\ \gamma_{11} \gamma_{12} \neq \gamma_{12} \gamma_{11}}} \frac{|\gamma_{11}, \gamma_{11}, \gamma_{21}; \gamma_{12}, \gamma_{12}, \gamma_{22}\rangle}{12\sqrt{6}}, \quad (5.9)$$

where the two sums contain the combinations of fluxes which braided with trivial and non-trivial topological influence, respectively. The probability  $p$  that a measurement would record complete annihilation  $p(00) = 1/3$  or the formation of two  $\sigma$  fluxons  $p(11) = 2/3$  after the braiding is obtained by projecting the braided superposition state onto the states  $|00\rangle$  and  $|11\rangle$ .

The numerical experiment shown in Fig. 5.6b simulates the action of the topologically non-trivial subsection of the braid on two of the states contributing to  $|00\rangle$ , those with fluxes  $(\text{III}_0^z, -\text{III}_0^z, \text{III}_0^y; \text{III}_0^z, -\text{III}_0^z, \text{III}_0^y)$  and  $(\text{III}_0^x, -\text{III}_0^x, \text{III}_0^y; \text{III}_0^z, -\text{III}_0^z, \text{III}_0^y)$ . The outcomes of measurements corresponding to the first case (d) or second case (e) are shown. Before fusion (c) all anyons have green cores. Upon counting anyons from left

to right, when the second and third (in qubit one), and fourth and fifth (in qubit two) anyons are fused, both pairs may either annihilate (d) or leave a green anyon behind (e).

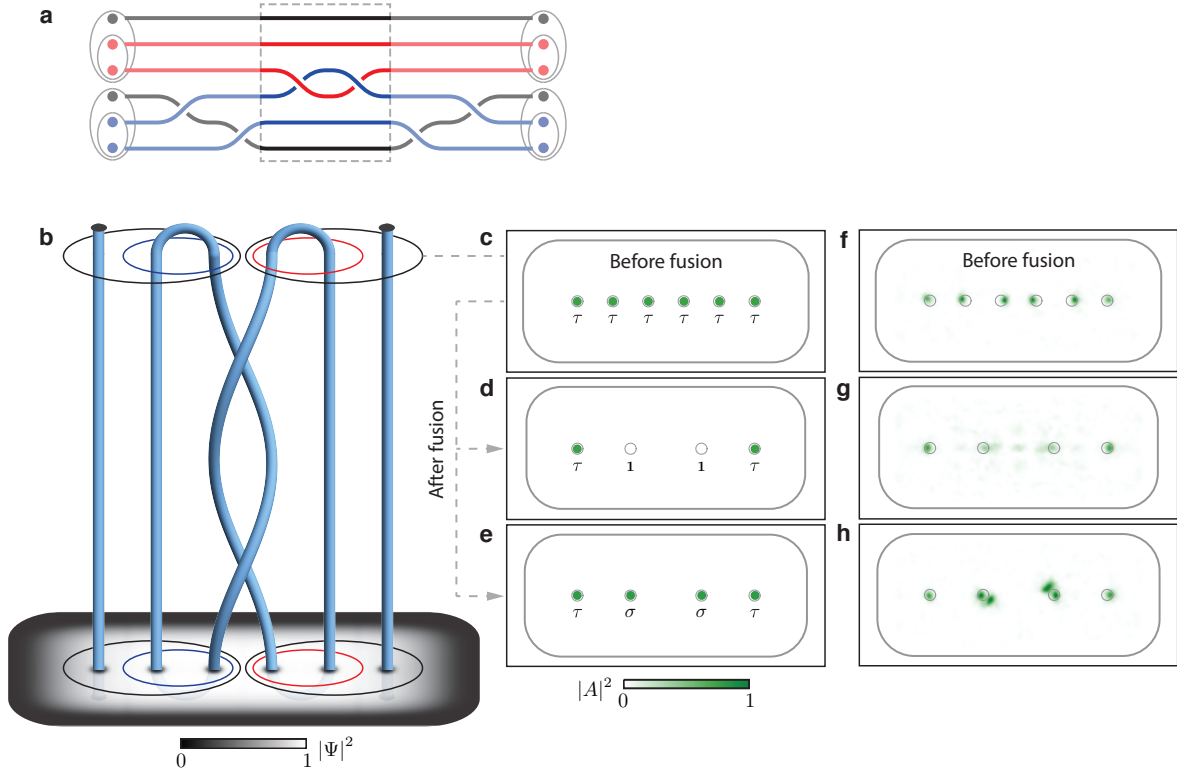


**Figure 5.6:** Two qubit braiding operation. **a**, Braid diagram for a unitary operation applied to an initial  $|00\rangle$  state where the topologically trivial operations are greyed out. Coloured strands are used to distinguish the measurement anyons of each qubit. **b**, The paths of the six  $\tau$  anyons trace out the topologically non-trivial braid shown in **a**. Time flows upward. The total condensate density is shown for the initial state. The overlaid concentric ellipses denote the orientation of the qubits as a graphical representation of the bracket notation used in the text. **c**, Spin-singlet pair amplitude of the qubits just before the fusion. The rounded square marks the boundary of the condensate and the vortex locations are denoted by the circles. The inter-vortex separation is  $27\mu\text{m}$ . **d**, a measurement outcome corresponding to the annihilation of the second and third, and fourth and fifth anyons, counting left to right, as in the  $|00\rangle$  state. **e**, a fusion outcome corresponding to non-annihilation as in the  $|11\rangle$  state. Data in **c-e** are thresholded relative to half the maximum value in **c** and any maxima within the vortex location markers are mapped to the solid green circles. **f-h**, Raw data for **c-e** without thresholding. The specific fluxes of the six vortices in (d) are  $(\text{III}_0^z, -\text{III}_0^z, \text{III}_0^y; \text{III}_0^z, -\text{III}_0^z, \text{III}_0^y)$  and in (e) they are  $(\text{III}_0^x, -\text{III}_0^x, \text{III}_0^y; \text{III}_0^z, -\text{III}_0^z, \text{III}_0^y)$ .

## 5.6. Universality

In Section 2.9, we defined a universal topological quantum computer as one for which any unitary operator can be approximated, up to a phase, to arbitrary accuracy by only braiding the anyons. This implies the existence of a minimum set of unitary operations from which any other may be generated. Mathematically, universality is defined as the existence of a dense mapping of the braid group of the anyons onto  $SU(2)$ . The Fibonacci anyon model does provide such a dense mapping and is thus universal [183, 188, 189]. However, universality is not the case for all anyon models. Indeed, there is a conjecture that a non-Abelian anyon model is universal by braiding alone if, and only if, the square of the quantum dimension is not an integer [228]. For example, Ising anyons [171], which are associated with Majorana zero modes [32], are not universal. The quantum dimension for the non-Abelian anyon in the Ising model is  $\sqrt{2}$ , which is evidently an integer when squared. However, the Ising anyon model can be made universal by supplementing the topologically protected braids with a non-topologically protected  $\pi/8$  phase gate [229, 230]. While the non-topologically protected phase gate introduces greater susceptibility to error, the lack of an experimentally realisable platform based on Fibonacci anyons makes Ising anyons still a promising potential platform for realising topological quantum computing.

Similar to the case of Ising anyons, the pure fluxons considered here are not capable of universal quantum computation by braiding alone. Indeed, the quantum dimension of the  $\tau$  anyons, due to the finite group structure, is integer. It is the underlying finite group structure which fundamentally limits the computational power of fluxons. Consider a single fluxon qubit  $|0\rangle = |\gamma_1, \gamma_1^{-1}, \gamma_2\rangle$  and apply sequences of elementary braids  $\sigma_1$  (clockwise braid of the the first two anyons; see Fig. 2.10(a)) and/or  $\sigma_2$  (clockwise braid of the second and third anyons). Such a sequence is called a braid word. We define the state of the qubit by the configuration of the fluxes, of which there are a finite number ( $4 \times 3 = 12$ ). There is a finite set of braid words corresponding to the operations which produce each configuration in the shortest combination of braids. The longest braid word which does not repeat a configuration of the fluxes is eight braids long. The same general result is obtained whether we choose  $|0\rangle = |\gamma_1, \gamma_1^{-1}, \gamma_1\rangle$ , or if the qubit is in the  $|1\rangle = |\gamma_1, \gamma_1, \gamma_2\rangle$  state, or with the inclusion of the inverse braids. Hence, the fluxon qubits are periodic under braiding and the braid group provides a finite or ‘sparse’ mapping onto  $SU(2)$ .

In a series of papers, Mochon [231, 232] outlined the capacity of certain finite groups to support universal topological quantum computation. For non-solvable finite groups, it

is possible to achieve universal topological quantum computing by only braiding fluxons. In short, the quantum gate operations are constructed by braiding the qubits with ancilla fluxon pairs with predetermined fluxes [231]. Moreover, for finite groups that are solvable but not nilpotent, universality is achieved by employing the full quantum double to introduce additional non-topological operations involving the chargeons. Specifically, the additional operations entail non-destructive probabilistic projective measurements of the qubits made by braiding them with ancilla chargeon pairs, with predetermined charges that fuse to the vacuum. The measurement is completed by a subsequent fusing of the chargeon pair which will, in a probabilistic fashion, either result in the vacuum or a remnant particle. It is not clear how to experimentally generate and then store the large reservoir of ancilla chargeons required for these gate operations. As the binary tetrahedral symmetry group satisfies the criteria of being solvable and not nilpotent, we can use chargeon braiding to escape the periodic nature of the fluxon braiding described above.

## 5.7. Realising quantum superpositions of fluxons

The initial state of a fluxon quantum computer is a flux eigenstate corresponding to some superposition of vacuum flux states. The non-Abelian anyons exist as topological states in the coherent macroscopic spinor wave function describing many condensate atoms. Hence, the ability to perform quantum information processing in this context relies on the capacity to create and maintain true quantum superpositions with a macroscopic number of atoms in a Bose–Einstein condensate. This is a challenging prospect. Macroscopic quantum superpositions, in the form of cat states<sup>1</sup>, have been experimentally investigated in the context of superconducting quantum interference devices (SQUIDS) [233–235]. Here, electron Cooper-pairs form a macroscopic coherent quantum state with dissipationless supercurrent flow about the superconducting ring. By careful tuning of the magnetic flux through the ring, it is proposed that cat states are realised such that prior to a measurement the Cooper-pairs are in a superposition state of clockwise and anticlockwise flow. Cat states have, similarly, been theoretically proposed for number states of BECs [236–239], in effect realising a superposition state of two internal states of the condensate atoms. Moreover, there have been attempts to realise SQUID analogues with persistent superfluid currents in toroidal BECs [240,241].

---

<sup>1</sup>Cat states take the form  $(|0\rangle + |1\rangle)/\sqrt{2}$  and are named for the well known Schrödinger cat thought experiment

Superposition states of counter-flowing superfluid currents, analogous to the flux cat states in SQUIDs, have been considered for these toroidal BECs [242–244]. Such macroscopic cat states are highly sensitive to decoherence, with the atoms realising a definite pure number/supercurrent state rather than a superposition. Furthermore, it is not clear whether an actual cat state is realised in these systems or whether an effective spinor structure is achieved with half the atomic population existing in one state and the other half in the other state.

Similarly, it might be expected that an  $N$ -atom superposition state realising a particular fluxon could decohere, for example to a state where the atoms realise a definite flux state instead of a superposition of fluxes. In that case, the length of the coherence time will determine whether useful computational operations can be performed. However, while the SQUID and toroidal BEC experiments represent superposition states of orbital angular momentum, our  $\tau$  fluxon anyons are pure spin vortices and the flux eigenstates are superpositions of different projections of spin angular momentum. As such, the  $\tau$  flux eigenstates may exhibit longer coherence times. Furthermore, considering the limit of very small condensate atom numbers may promote longer lived superpositions but also the mean-field description of the bosonic condensates becomes inapplicable. Ultimately, answering the question of fluxon decoherence is beyond the scope of this thesis and the classical mean-field theory techniques employed therein.

## 5.8. Summary

We have demonstrated that certain non-Abelian fractional vortices in spinor Bose–Einstein condensates may be non-Abelian anyons and have shown how such vortex anyons could be braided and fused using guiding laser beams. Mochon showed [232] that anyons based on finite groups that are solvable but not nilpotent are capable of universal quantum computation. Since the binary tetrahedral group does satisfy these criteria, it may be a fruitful platform for developing a universal quantum computer. Although, similar to the case of Ising anyons [32, 171], the pure fluxons considered here are not capable of universal quantum computation by braiding alone and additional operations involving chargeons will be required to achieve universality [231, 232]. However, even non-universal anyons may be capable of being used as a quantum memory and even performing certain quantum algorithms with full topological protection, such as a specific Grover search algorithm [14] and a calculation of the Jones polynomial at a specific root of unity [33].

To realise such vortices experimentally a series of engineering challenges must be confronted. The foremost experimental challenge for the realisation of non-Abelian vortex anyons is preparing a Bose–Einstein condensate in a stable non-Abelian ground state phase. Presently, experiments with spinor condensates are limited to phases accessible in the presence of background magnetic field noise and with the natural scattering lengths of available atomic species, since the spin-dependent coupling constant  $c_2$  cannot be independently modified using standard Feshbach resonance techniques, see Chap. 3. The biaxial nematic phase also hosts non-Abelian vortex anyons and is perhaps a better prospect experimentally, since it may be realised in the presence of an external magnetic field and could potentially be achieved with naturally occurring scattering lengths [91]. Furthermore, experimental searches for non-Abelian vortices are not limited to spin-2 condensates with many other non-Abelian phases having been predicted for higher spin BEC systems [156–161]. Indeed, the spin-6 condensate, recently realised with erbium atoms [114], has a phase that is symmetric under the non-solvable non-Abelian binary icosahedral group [161] and is therefore an attractive prospect for realising universal topological quantum computation employing only fluxons [231].

As discussed in the introduction to this chapter, vortices in Bose–Einstein condensates can be manipulated using dynamical pinning potentials generated by focused laser beams [221, 222]. This enables controlled braiding and fusion of vortex anyons. Condensates containing a few hundred vortices can realistically be achieved using current experimental technologies and it may be possible to control them using laser fields morphed with high resolution digital micro-mirror devices (DMDs) [68]. Hence, the creation of 100 high quality topological qubits is a plausible prospect. A potential drawback is the adiabatic speed limit of massive vortices [245, 246], in turn limiting the clock speed of such a BEC vortex topological quantum abacus. This issue could perhaps be overcome if robust synthetic non-Abelian fluxons could be created using artificial gauge field techniques [247–249]. Furthermore, if the system is not sufficiently 2D, i.e. more oblate than pancake, bending of the vortices could become a source of decoherence.

While challenges remain for realising non-Abelian vortex anyons capable of topological information processing and storage, non-Abelian vortices in spinor Bose–Einstein condensates hold promise for a tangible demonstration of the underlying principles of topological quantum computation and should be pursued further. Naturally, the degree of interest in non-Abelian vortex anyons will be tempered by any progress on realising topological quantum computing in Majorana fermion or fractional quantum Hall platforms. Regardless of the implications for quantum computation, there are still a number

---

of fascinating details that merit further exploration, notably the transmutation of fluxes under the topological influence with the attendant change in the vortex fusion dynamics. The potential existence of Cheshire charge as a delocalised property of non-Abelian vortex pairs similarly warrants further investigation. Indeed, detecting Cheshire charge in an explicit condensed matter system is of interest in its own right [250]. Optimistically, during these investigations new experimental procedures may be discovered which overcome some or all of the stated challenges. Similarly, a deeper understanding of non-Abelian vortices in few atom condensates, from a theory standpoint, may resolve any potential issues with creating flux superposition states.



# Chapter 6.

## Two-dimensional quantum turbulence in spinor condensates

In this chapter we explore the properties of two-dimensional quantum turbulent flows formed from disordered arrays of fractional-charge vortices, of both Abelian and non-Abelian algebra, in a spinor Bose–Einstein condensate. This entails first modelling protocols for initiating turbulence through the interference of condensate fragments. The chapter concludes with an analysis of turbulent dynamics and examines the prospects for uncovering new stochastic phenomena which might arise from prevailing non-Abelian interactions.

### 6.1. Quantum turbulence

The important characteristics of a turbulent state are; (I) an entangled array of quantum vortices producing a disordered fluid flow; (II) a non-linear interaction of the vortices of the kind  $(\mathbf{v} \cdot \nabla)\mathbf{v}$ , present in the Euler equation; (III) a distribution of kinetic energy across a number of length scales and a corresponding self-similar cascade of the energy from one length scale to another.

Quantum turbulence contains all three of these characteristics. Quantum turbulence manifests as a disordered tangle of quantised vortices [251, 252]. The non-linearity of the fluid flow is evident in the Gross–Pitaevskii equation due to the interaction terms, which can be re-written in a form similar to the non-linear term in the Euler equation. The important length scales for a turbulent state of a trapped Bose–Einstein condensate are the system size  $L$ , the inter-vortex separation  $l$  and the vortex core size  $\xi$ . Depending

on the length scale at which energy is injected into the turbulent state there can either exist a turbulent state with large quasi-classical flows ( $> l$ ) or without ( $< l$ ) [253]. These two states are Kolmogorov type, or Vinen type turbulence, respectively. We should also distinguish between driven turbulence, where energy is constantly injected and dissipated, and decaying turbulence, where the fluid is stirred then left to equilibriate. In this thesis, we focus exclusively on the latter type of turbulence.

One useful observable for characterising turbulent flows is the incompressible kinetic energy. Using the Helmholtz decomposition [132], the velocity field  $\mathbf{v}$  can be decomposed into its incompressible,  $\mathbf{v}^i$ , and compressible,  $\mathbf{v}^c$ , components as  $\mathbf{v} = \mathbf{v}^i + \mathbf{v}^c$ . By definition,  $\nabla \cdot \mathbf{v}^i = 0$  and  $\nabla \times \mathbf{v}^c = 0$ . Hence, the incompressible and compressible components can be thought of as arising from the velocity fields associated with the vortices and sound waves, respectively. The kinetic energy,

$$E_k(t) = \int \frac{\hbar}{2M} n(r, t) d\mathbf{r}, \quad (6.1)$$

can be similarly decomposed into its incompressible and compressible contributions, respectively, as

$$\begin{aligned} E_k^i(t) &= \frac{M}{2} \int n(r, t) (V^i)^2 \\ E_k^c(t) &= \frac{M}{2} \int n(r, t) (V^c)^2. \end{aligned} \quad (6.2)$$

Experiments on Kolmogorov type quantum turbulence in three-dimensional superfluid helium suggest the existence of a  $k^{-5/3}$  scaling law in the spectra of the incompressible kinetic energy, where  $k$  is the wavevector, over the intermediate length scales between  $L$  and  $l$  [254, 255]. Numerical simulations using the Gross–Pitaevskii equation have also obtained spectra consistent with this result [251, 256]. This spectrum, consistent with classical turbulence [101, 102], outlines a distribution of the incompressible kinetic energy predominately in large scale vortex structures with a direct energy cascade toward small scale vortex structures. This Richardson cascade proceeds in the  $k^{-5/3}$  inertial scaling region via the scale invariant transport of energy from large to small vortex loops via reconnections [257]. However, a self-similar energy cascade requires a mechanism for dissipating energy at the smallest scales. In a superfluid, without true viscosity, it remains unclear what mechanism causes dissipation at the smallest scales. There is some support in numerical studies for the existence of a Kelvin wave cascade for length scales  $l < k < 2\pi/\xi$  [258, 259]. Here, the energy is transported from long to short wavelength

Kelvin waves, which are excited during the reconnections, until a point is reached that the energy is transferred to the compressible kinetic energy via the shedding of sound waves [260].

Two dimensional (2D) turbulence can occur in nature for systems where the transverse extent is significantly greater than the depth, for example, ocean or atmospheric currents and soap films. As discussed in Chap. 3 it is possible to achieve a two-dimensional condensate by tightly confining the gas along one direction [168]. In two-dimension, vortices become point-like objects and their vortex collision dynamics change accordingly. As we saw in Chap. 4, the collision dynamics of two-dimensional Abelian vortices are dominated by vortex-antivortex annihilation. The change in the collision dynamics is predicted to result in characteristically different turbulence. Spectra of the incompressible kinetic energy are proposed to show three regions corresponding to (1)  $k < 2\pi/\xi$  with power law  $k^{-3}$ , (2)  $2\pi/\xi < k < 2\pi/l$  with Kolmogorov scaling  $k^{-5/3}$  and (3)  $k > 2\pi/l$  with scaling  $k$  [132]. Unlike in the three dimensional system, the Kolmogorov scaling apparent in 2D turbulence is thought to correspond to an inverse energy cascade with the energy aggregating within large negative temperature vortex structures [261, 262]. The inverse cascade proceeds via the clustering of liked sign vortices into large fluid flow structures called Onsager vortices [206, 263, 264]. The inverse energy cascade is usually paired with a direct cascade in the enstrophy, defined as the total squared vorticity. The  $k^{-5/3}$  power law has been observed in some numerical simulations [264–266], though seems to be dependent on the particular configuration of the vortices [132]. The regime of 2D quantum has been attained in recent BEC experiments [104, 105, 208, 267], which provide a realisation of the negative-temperature Onsager vortex clusters [104, 105], and potential evidence of the  $k^{-5/3}$  power law [105, 267].

Recent experiments have also explored turbulence in a two-dimensional spin-1 condensate [135, 268, 269] where the spin degree of freedom permits a new kind of spin turbulence [270–272]. The characteristics of spin turbulence depend on the superfluid phase of the condensate. For a condensate in the ferromagnetic phase, after excitation into the turbulent state, the spins are spatially disordered but remain temporally frozen allowing a description using a spin glass order parameter [273]. Comparatively, in the polar phase the spins have small oscillations [271]. In both the ferromagnetic and polar phases the spin turbulence is characterised by a  $k^{-7/3}$  scaling law in the spin interaction energy spectra.

Spinor condensates may also host vortices with non-commuting topological charges whose collisions result in the formation of a rung vortex. The prospect of a turbulent

state of non-Abelian vortices which cannot reconnect presents the possibility of a new kind of non-Abelian quantum turbulence. Kobayashi *et al.* [106] numerically simulated a three-dimensional quantum turbulent state of non-Abelian vortices. Injecting energy at large length scales was observed to result in a unique  $k^{-7/3}$  power law in spectra of the incompressible energy. The power law is directly connected with a cascade in helicity,  $\mathbf{v} \cdot (\nabla \times \mathbf{v})$ , associated with the large-scale vortex network formed as a result of the rung formation collision dynamics.

The existence of the novel rung-hilition collision event, see Chap. 4, presents the possibility of a new kind of two-dimensional non-Abelian quantum turbulence, the properties of which we will explore in Sec. 6.7.

## 6.2. Initiating turbulence from multi-wave interference

There are many ways to create vortices in a Bose–Einstein condensate including rotating traps [197–200], stirring with a repulsive laser [274], imprinting of phase using Laguerre–Gauss beams [201] and rapid quenches through phase transitions [275]. In this chapter we focus on vortex production based on multi-wave interference to achieve a controllable and repeatable technique to generate quantum turbulence. This concept is illustrated in the schematic Fig. 6.1. The destructive interference of two wave packets produces dark stripe solitons, each of which may subsequently disintegrate due to non-linear interactions into rows of alternating vortices and antivortices [276–279]. However, the destructive interference of three waves may produce lattices of vortices and antivortices in predictable regular honeycomb lattice structures [280–284]. BECs are coherent matter waves which can interfere. Scherer *et al.* used such a method and by colliding three Bose–Einstein condensate fragments they observed quantised vortices in the system [285]. In their experiment an external potential was used for separating the condensate initially into three condensate fragments. Adiabatic removal of the separating potential provided a statistical prediction of the presence or absence of a vortex in the resulting condensate, depending on the random relative phases of the initial condensate components. In contrast with this experiment, under sufficiently rapid non-adiabatic removal of the separating potential, three colliding condensate fragments have been predicted and demonstrated to form a honeycomb vortex-antivortex lattice, equivalent to two interleaved non-rotating honeycomb Abrikosov vortex lattices—one of vortices and the other of anti-

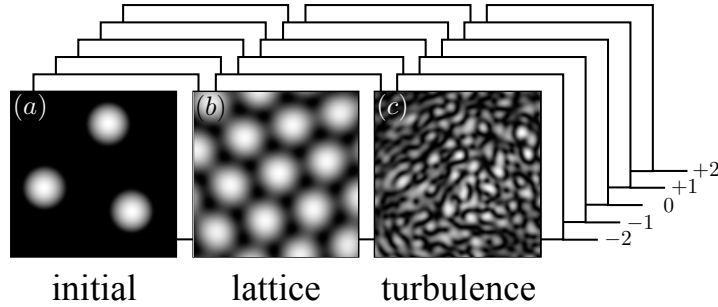


**Figure 6.1:** Schematic of our numerical experiment showing the total particle density at three different times of evolution. (a) The five hyperfine states behind the total density images of the  $F = 2$  Bose–Einstein condensate are initially confined in a species-independent triple-well trap, superposed with a global harmonic potential. (b) Upon removal of the triple-well potential, the three condensate fragments expand and interfere in the central portion of the harmonic trap. The multi-wave interference of the condensate fragments produces transient honeycomb vortex-antivortex lattices in each of the occupied hyperfine spin states. (c) At later times the system transitions to quantum turbulence.

vortices [282, 286, 287]. Similar honeycomb vortex lattices could also be produced by using aberrated matter wave lensing technique [288, 289]. Moreover, the Kjergaard group has developed a versatile optical tweezer based collider for cold atoms [221]. Possible adaption of this experimental set-up for 2D confinement could enable generic multi-wave condensate collisions with controllable initial momentum vectors of the wave packets. For a two-component pseudo-spin system, three-wave collisions lead to condensate pseudo-spin textures [283]. In the following sections we detail the theoretical framework of three-wave interference, first for a scalar condensate in Sec. 6.3 and then extending to an  $F = 2$  spinor BEC in Sec 6.4 with the motivation of devising an experimentally controllable method to produce lattices of fractional-charge vortices.

### 6.3. Collision of three scalar condensates

We will first consider a collision of three single-component scalar condensates and thereafter extend the results to the multi-component spinor condensates. While the condensate fragments are modelled as three symmetrically arranged wave packets of equal initial population and shape, on a local scale their interference may be modelled as that of three plane waves. This approximation is represented by a wave function

$$\psi(\mathbf{r}) = \sum_{j=1}^3 e^{i\zeta_j(\mathbf{r})}, \quad (6.3)$$

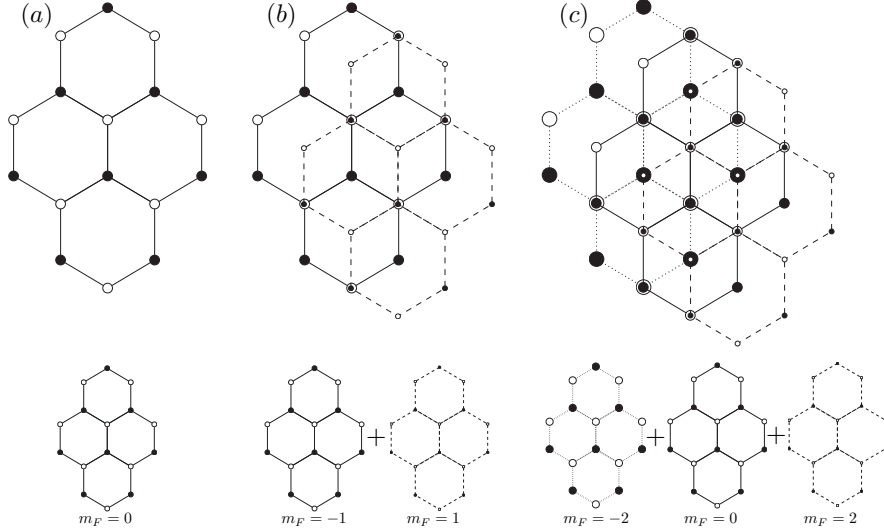


**Figure 6.2:** Structure of vortex lattices with black and white circles corresponding to the locations of vortices and antivortices, respectively. (a) A honeycomb lattice structure due to three-plane-wave interference in a single spin state of a condensate. (b) AB stacking of two honeycomb lattices. (c) ABC stacking of three honeycomb lattices.

where  $\zeta_j(\mathbf{r}) = \mathbf{k}_j \cdot \mathbf{r} + \phi_j$ . The  $\mathbf{k}_j$  are momentum vectors of equal magnitude  $|\mathbf{k}|$  of the three colliding condensate fragments and  $\phi_j$  specifies the phase of the  $j$ th condensate fragment at the origin. For the rest of this section  $\phi_1 = 0$ .

The quantised vortices are nodal lines of the complex valued wave function and are identified as singularities of the phase function  $\arg(\psi)$ . For destructive three-plane-wave interference the locations of the vortices,  $r_{n,m}^+$ , and antivortices,  $r_{n,m}^-$ , are given by the simple geometric relations

$$\begin{aligned}
 r_{n,m}^+ &= \frac{4\pi}{3|\mathbf{k}|} (n + m/2 + 1/2\pi(\phi_2 + \phi_3)) \hat{e}_x \\
 &\quad + \frac{2\pi}{\sqrt{3}|\mathbf{k}|} (m + \phi_2/\pi) \hat{e}_y, \\
 r_{n,m}^- &= \frac{4\pi}{3|\mathbf{k}|} (n + m/2 + 1/2\pi(\phi_2 + \phi_3) + 1/2) \hat{e}_x \\
 &\quad + \frac{2\pi}{\sqrt{3}|\mathbf{k}|} (m + \phi_2/\pi + 1/3) \hat{e}_y
 \end{aligned} \tag{6.4}$$

describing a honeycomb lattice, as illustrated in Fig. 6.2(a). The  $\hat{e}_i$  are Cartesian basis vectors. In comparison, by treating the colliding wave packets as Gaussian functions the

interference is described by the wave function [282, 290]

$$\begin{aligned} \psi(\mathbf{r}, t) = & \sqrt{\frac{\pi^{-\frac{1}{2}} \frac{\Delta p}{\hbar}}{1 + i \frac{(\Delta p)^2 t}{m\hbar}}} \\ & \times \sum_{j=1}^3 \exp\left(\frac{-\left(\frac{\Delta p}{\hbar}\right)^2 |\mathbf{r} - \mathbf{r}_j|^2}{2 \left[1 + i \frac{(\Delta p)^2 t}{m\hbar}\right]} + i\phi_j\right), \end{aligned} \quad (6.5)$$

where  $\Delta p$  defines the momentum uncertainty or the width of the initial condensate fragments and  $|\mathbf{r} - \mathbf{r}_j|$  is the distance between the centre of the  $j$ th Gaussian and an observation point. The subsequent vortex and antivortex locations, derived in detail by Ruben et al. [282], are respectively

$$\begin{aligned} r'_{n,m}{}^+ = & \frac{1}{2} \left( r - \frac{\beta M(m)}{r} \right) \hat{e}_x \\ & + \frac{1}{2\sqrt{3}} \left( r - \frac{\beta [2N(n) - M(m)]}{r} \right) \hat{e}_y, \\ r'_{n,m}{}^- = & \frac{1}{2} \left( r - \frac{\beta M'(n)}{r} \right) \hat{e}_x \\ & + \frac{1}{2\sqrt{3}} \left( r - \frac{\beta [2N'(m) - M'(n)]}{r} \right) \hat{e}_y, \end{aligned} \quad (6.6)$$

where  $r$  is the separation between the centres of each condensate fragment and  $\beta = 2 \left[ (\hbar t)^2 + m^2 (\hbar/\Delta p)^4 \right] / 3m\hbar t$ . The integers  $n$  and  $m$  index the lattice points via the functions

$$\begin{aligned} M(m) &= 2\pi \left[ 1 + 3 \left( m - \frac{\phi_2}{2\pi} \right) \right] \\ N(n) &= 2\pi \left[ 2 + 3 \left( n - \frac{\phi_3}{2\pi} \right) \right] \\ M'(n) &= 2\pi \left[ 2 + 3 \left( n - \frac{\phi_2}{2\pi} \right) \right] \\ N'(m) &= 2\pi \left[ 1 + 3 \left( m - \frac{\phi_3}{2\pi} \right) \right]. \end{aligned} \quad (6.7)$$

Interestingly, also the Gaussian wave packet model, Eq. (6.6), produces a uniform honeycomb vortex lattice and hence the vortex lattice vectors of Eq. (6.4) and Eq. (6.6) can be mapped onto each other at any time.

## 6.4. Collision of three spinor condensates

Within the weak interaction approximation of three-source interference of spinor condensates, where the kinetic energy of the system dominates over the particle interactions, the structure of the vortex lattice formed in each internal spin component is independent of influence from the condensate particles in other spin states. The vortex lattice structure in each spin component is thus equivalent to that produced by three source interference in a scalar condensate. Hence the semi-analytical three-plane-wave interference model can be extended to a spinor wave function by modelling each spinor component as a scalar wave function. The spinor wave function describing the lattice structure local to the trap centre is then

$$\Psi(\mathbf{r}) = \sum_{j=1}^3 \begin{pmatrix} |\psi_2(\mathbf{r})| e^{i\zeta_{2j}(\mathbf{r})} \\ |\psi_1(\mathbf{r})| e^{i\zeta_{1j}(\mathbf{r})} \\ |\psi_0(\mathbf{r})| e^{i\zeta_{0j}(\mathbf{r})} \\ |\psi_{-1}(\mathbf{r})| e^{i\zeta_{-1j}(\mathbf{r})} \\ |\psi_{-2}(\mathbf{r})| e^{i\zeta_{-2j}(\mathbf{r})} \end{pmatrix}, \quad (6.8)$$

where  $|\psi_i(\mathbf{r})|$  is constant and  $\zeta_{ij}(\mathbf{r}) = \mathbf{k}_j \cdot \mathbf{r} + \phi_{ij}$ . The phase at  $\mathbf{r} = 0$  of the  $j$ th condensate fragment in the  $i$ th spin component is denoted by  $\phi_{ij}$ . While the magnitude of the momentum vector  $\mathbf{k}_j$  determines the vortex lattice spacing and is used as a free parameter for matching the semi-analytical description and the numerical results. Similarly to the scalar case, the phases  $\phi_{ij}$  determine the positions of the vortices nucleated in the spinor condensate [see Eq. (6.7)].

In spinor systems the vortex lattice produced during the interference can be thought of as a composition of vortex-antivortex lattices in each of the internal spin states, see Fig. 6.2. Hence there are three possible alignments of each vortex-antivortex lattice; (I) vortex in one component aligns with a vortex in the other component; (II) antivortex aligns with vortex in the other component or (III) vortex (antivortex) aligns with a region of non-zero condensate density in the other component. The relative position of

the vortices in different spin states determine which spinor-vortex types are generated in the spinor condensate. By controlling the spinor phases during preparation of the initial condensate any desired alignment of the vortex lattices in different spin states may be achieved [283]. The various ways these vortex lattices may be stacked is analogous to those in multilayer graphene structures [291]. Figure 6.2(a) shows a honeycomb vortex lattice structure in a single component scalar (spin-0) condensate. Frame (b) shows an AB stacking of two honeycomb lattices and frame (c) shows an ABC stacking of three-layer honeycomb lattices. Both (b) and (c) yield three different kinds of antisymmetric vortices in the global order parameter and the same is true for ABA and BAB stackings. Unshifted stackings such as AA and AAA all result in two different kinds of vortices only, which are equivalent to the scalar condensate vortices and antivortices shown in (a). Populating 4 or all 5 spin components further increases the complexity and the variety of possible vortex states.

As shown in the case of colliding scalar condensate fragments, the outcome is a honeycomb vortex lattice irrespective of the initial phases of the condensate fragments. In such a case the collision itself acts as a measurement process determining the relative phases between the condensate fragments [292]. Similarly for a spinor case the collision will result in a vortex lattice but this time the vortex types nucleated in the lattice will depend on the phase structure of the full spinor wave function. In the numerical simulations the initial phases  $\phi_{ij}$  can be set explicitly without loss of generality. In experiments, the relative phases within a given spin state could be controlled using Laguerre–Gauss laser modes to imprint any order vortex phase winding [73, 293]. It is feasible that the different diffraction orders of a single Laguerre–Gauss beam could potentially be used to control each  $\phi_{ij}$ . However, to determine the vortex positions it is sufficient to fix only the relative winding numbers between the spin components. This is because the relative phases between the spin states cause a local rotation of the spin but leave the alignment of the vortex lattices unchanged. Alternatively, suitable initial states could be generated by imprinting the desired spin textures using spin-engineering techniques similar to those used in Refs. [74, 77, 78].

## 6.5. Numerical experiments

We numerically simulate a condensate of  $^{87}\text{Rb}$  atoms with effective particle number  $N = 5.0 \times 10^4$ . The dimensionless coupling constant  $c'_0 = c_0 N / \hbar \omega l^2$  is determined from the experimentally measured scattering lengths of  $^{87}\text{Rb}$  [190–192]. As per Chapter 3 the dimensionless spin interaction strengths are chosen as  $c'_1 = c'_2 = 0.5 c'_0$ , which specify the cyclic-tetrahedral phase.

The three-source interference simulations are performed on a Cartesian numerical grid with  $2048 \times 2048$  points. The trapping potential is a combination of a harmonic oscillator potential with a frequency  $\omega = 2\pi \times 4.9$  Hz and a sum of three localised Gaussian terms. This produces a triple-well potential,  $V_{\text{ext}} = m\omega^2 r^2 / 2 + \sum_{i=1}^3 P \exp(-\frac{1}{2}(\mathbf{r} - \mathbf{r}_i)^2 / \sigma^2)$ , where  $P = 300 \hbar \omega$  and  $\sigma = 18.8 l$  are the potential height and standard deviation of the Gaussian potentials centred at positions  $\mathbf{r}_i$ . The initial-state spinor is chosen to represent either a biaxial nematic or cyclic-tetrahedral vortex state. The vortex phase windings are initialised by setting the phases  $\phi_{ij}$  as described in Sec. 6.4. An example phase structure, corresponding to the biaxial nematic half quantum vortex case, is shown in Fig. 6.3. Similar initial particle densities and phase maps of the other vortex states are shown in the Supplemental Material of Ref. [109].

We also perform simulations of initiating turbulence from disordered arrays of vortices, with both commuting and non-commuting topological charges, created using the phase

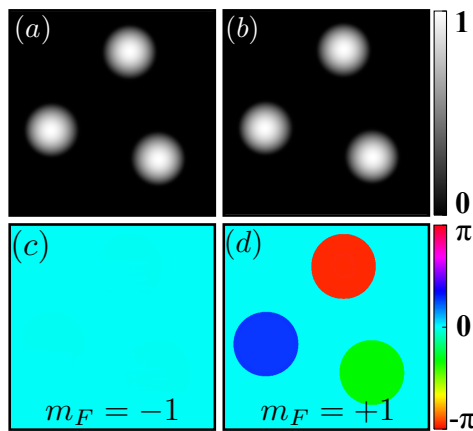


**Figure 6.3:** Initial state of the biaxial nematic half quantum vortex. (a)-(b) show the probability densities in the  $m = 1$  and  $m = -1$  spin states normalised to the maximum density. (c)-(d) show the phases of the two spin states. In all figures in this section, the range of the colourbar is from the minimum to maximum value of the observable in arbitrary units. The field of view of each frame is  $(23.4 \times 23.4) l$ .

imprinting methods discussed in Sec. 3.2. These simulations are performed on a numerical grid with  $512 \times 512$  grid points. To realise a uniform condensate density, we use a hard-wall trapping potential  $V_{\text{ext}} = r^8/4$ , with a radius  $R_{\text{hw}} \approx 58 \mu\text{m}$ .

## 6.6. Vortex lattices from three-source interference in a spin-2 Bose–Einstein condensate

In the following, we present simulation results for three representative initial states with spinor structures corresponding to a biaxial nematic half quantum vortex, a cyclic spin vortex, and a cyclic one third vortex. We use the destructive three-plane-wave interference in Eq. (6.8) as an analytical model for comparison with the numerical results. While the values of our coupling constants preference the cyclic-tetrahedral phase, their strengths are unimportant in determining the initial lattice structure. However the particular spin interaction strengths will play an important role in determining the subsequent turbulent state.

We initialise the biaxial nematic half quantum vortex state  $\sqrt{2}(0, 1, 0, \exp(i\theta), 0)/2$  by setting the phases  $\phi_{-1j} = 0$  and  $\phi_{1j} = 0, \frac{2\pi}{3}, \frac{4\pi}{3}$  for the  $j = 1, 2, 3$  condensate fragments, respectively, with the other spin components empty. The semi-analytical model of Eq. (6.8) is initialised similarly. The initial probability density and phase map for the two non-zero population spin components are presented in Fig. 6.3 showing the  $2\pi$  phase winding across the three condensate fragments in the  $m = +1$  spin component. In all figures in this section, the range of the colourbar is from the minimum to maximum value of the observable in arbitrary units. Additionally, in this section we use the jet and copper colourmaps to represent the magnetization and spin-singlet pair amplitude densities, respectively. Both the magnetization and spin singlet pair amplitude density are initially zero.

After the triple-well component of the external potential is switched off, the three condensate fragments collide and a honeycomb lattice is formed in the condensate interior of each spin state, Fig. 6.4(a-d), while the exterior regions, where initially only two of the three condensate fragments have collided, are dominated by interference fringes. An expanded view of the honeycomb lattices in each spin component is provided in Fig. 6.5. The full and expanded views of the vortex lattices of the other vortex states can be found in the Supplemental Material of Ref. [109]. The vortex lattice consists of the three fractional

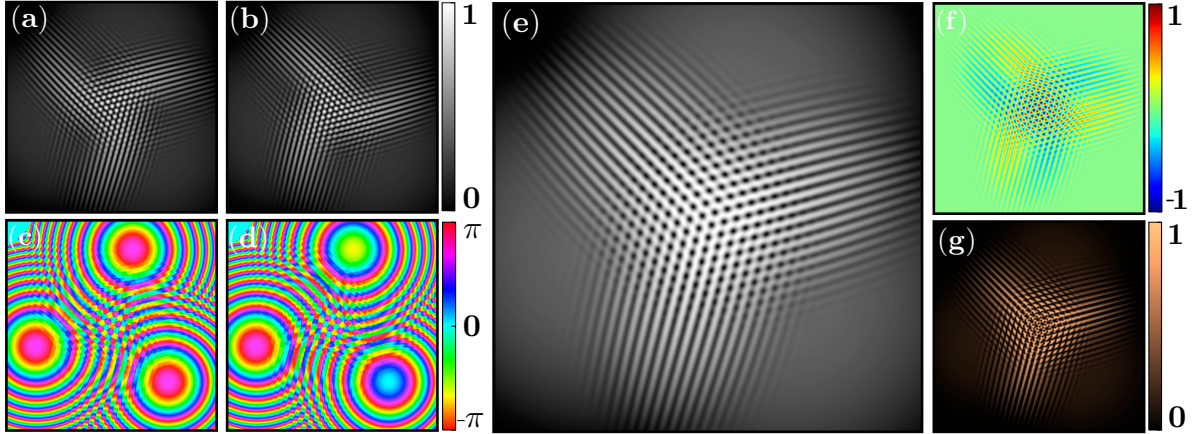


**Figure 6.4:** The lattice for the half quantum vortex initial state from a Gross–Pitaevskii simulation. (a)-(d) show the probability density of the  $m = -1$  and  $m = 1$  spin states normalised to the maximum density and the corresponding phases. (e)-(g) show the total particle density, magnetization density and the spin singlet pair amplitude density. The field of view of each frame is  $(23.4 \times 23.4) l$  and the images are for a time  $\tau = 0.55 1/\omega$  after the triple-well trapping potential is switched off.

vortex types, which are measured by visually inspection of the order parameter rotations, as discussed in Sec. 3.3. The vortices are two  $3\pi/2$  half quantum vortices;  $-\text{VIIb}_0^x$  with  $\Psi(\mathbf{r}, -\text{VIIb}) = \sqrt{2}(0, 1, 0, e^{-i\theta}, 0)/2$  and  $-\text{VIIb}_{-1}^x$ , and an integer spin vortex  $-\text{IIb}_0$ . The order parameters of these vortices are  $\Psi(\mathbf{r}, -\text{VIIb}_0^x) = \sqrt{2}(0, 1, 0, e^{-i\theta}, 0)/2$ ,  $\Psi(\mathbf{r}, -\text{VIIb}_{-1}^x) = \sqrt{2}(0, e^{i\theta}, 0, 1, 0)/2$ , and  $\Psi(\mathbf{r}, -\text{IIb}_0) = \sqrt{2}(0, e^{-\theta}, 0, e^{i\theta}, 0)/2$ . Here we use the letter b in the vortex label to distinguish the biaxial nematic vortices from their cyclic-tetrahedral counterparts. For a description of these vortices see Appendix D. The topological charges of the lattice vortices all commute, hence their topological interactions are Abelian. The total particle density  $n(\mathbf{r})$ , magnetization density  $F_z(\mathbf{r})$  and the spin singlet pair amplitude density  $|A(\mathbf{r})|$  are shown in Fig. 6.4(e-g), respectively. The densities in the two populated spin components develop prominent spiral arms with opposite chirality, preserving the three-fold symmetry in the total density.

Figure 6.6(a-c) shows an expanded view of Fig. 6.4(e-g) local to the trap centre. These frames should be compared with the respective frames Fig. 6.6(d), (e) and (f) showing the corresponding densities calculated using the semi-analytical model. From such comparison it is evident that the semi-analytical non-interacting model is in good agreement with the full Gross–Pitaevskii simulation, as far as the predicted lattice structure is concerned, with the produced vortex types being identical.

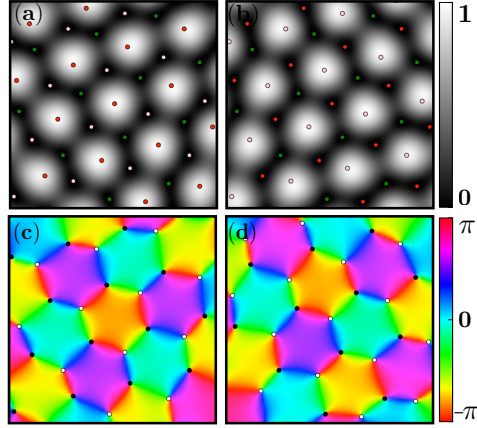


**Figure 6.5:** Enhanced view, local to the trap centre, to the lattice for the half quantum vortex initial state from a Gross–Pitaevskii simulation. (a)-(d) show the particle probability densities in the  $m = -1$  and  $m = 1$  spin states, normalised to the maximum density, and the corresponding phases. The locations of the  $-VII_0^x$ ,  $-VII_{-1}^x$  and  $-II_0$  lattice vortices are denoted by coloured dots of pink, red, and green, respectively. While the white and black dots denote quantum vortices and antivortices, respectively, in each spin component. The field of view of each frame is  $(2.3 \times 2.3) l$  and the images are for a time  $\tau = 0.55 1/\omega$  after the triple-well trapping potential is switched off.

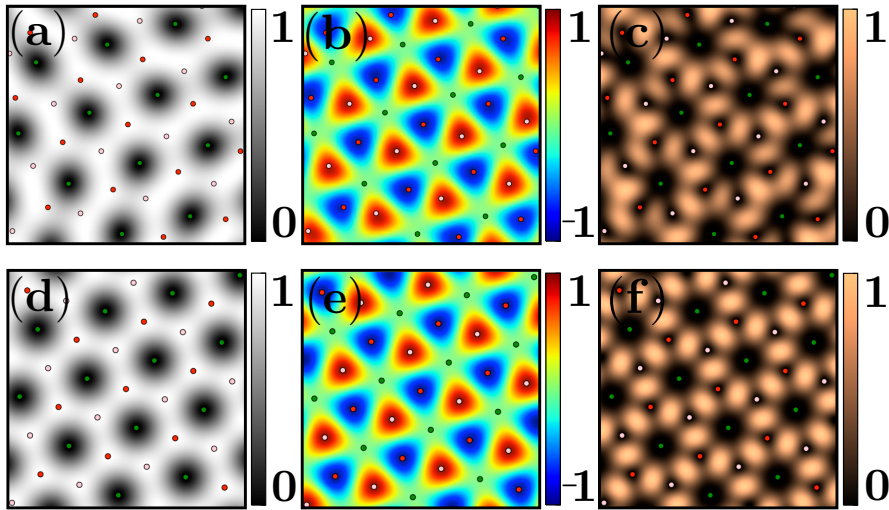


**Figure 6.6:** An expanded view, local to the trap centre, of the lattice for the half quantum vortex initial state. (a)-(c) The results from a Gross–Pitaevskii simulation showing the total particle density, magnetization density and the spin singlet pair amplitude density for a time  $\tau = 0.55 1/\omega$  after the triple-well trapping potential is switched off. (d)-(f) The corresponding observables calculated from the semi-analytical spinor in Eq. (6.8) where  $\phi_{-1j} = 0$  and  $\phi_{1j} = 0, \frac{2\pi}{3}, \frac{4\pi}{3}$  for  $j = 1, 2, 3$ , with the other spin components empty. The locations of the  $-VII_0^x$ ,  $-VII_{-1}^x$  and  $-II_0$  lattice vortices are denoted by coloured dots of pink, red, and green, respectively. The field of view of each frame is  $(2.3 \times 2.3) l$ .

The biaxial nematic phase initial state contains equal population of atoms in both spin states  $m = \pm 1$ . The particle density is non-zero in the cores of the half quantum vortex types. Therefore the half quantum vortices have magnetic cores with a magnetization of equal magnitude but opposite sign as shown in Fig. 6.6(b). The spin vortex has a zero particle density core structure and consequently zero magnetization and spin singlet amplitude. The magnetization density in Fig. 6.6(b) shows a honeycomb pattern of maxima and minima, coinciding with the locations of the  $-\text{VII}_0^x$  and  $-\text{VII}_{-1}^x$  vortex cores, respectively. From both the magnetization and the spin singlet pair amplitude we note that the cores of the half quantum type vortices have a triangular core structure in comparison to the circular structure of the  $-\text{II}_0$  spin vortex. The spin singlet pair amplitude density in Fig. 6.6(c) displays distinctly different lattice structure when contrasted with the particle and magnetization densities.

Consider next a condensate with three spin components populated with condensate particles, which leads to the ABC stacking of vortex lattices. For this we initialise the cyclic-tetrahedral phase spin vortex state  $\left(\frac{i}{2} \exp(-2i\theta), 0, \frac{\sqrt{2}}{2}, 0, \frac{i}{2} \exp(2i\theta)\right)$  by setting the phases  $\phi_{-2j} = 0, \frac{8\pi}{3}, \frac{4\pi}{3}$ ,  $\phi_{0j} = 0$  and  $\phi_{2j} = 0, \frac{4\pi}{3}, \frac{8\pi}{3}$  for the  $j = 1, 2, 3$  condensate fragments, respectively, with the other spin components empty. The semi-analytical model of Eq. (6.8) is initialised similarly.

The vortex lattice, formed after the condensate collision, contains the spin vortex  $-\text{II}_0$ , with order parameter  $\Psi(\mathbf{r}, -\text{II}_0) = (ie^{i\theta}, 0, \sqrt{2}, 0, ie^{-i\theta})/2$ , and two vortices with order parameters  $\Psi(\mathbf{r}, \text{A1}) = (i, 0, \sqrt{2}e^{-i\theta}, 0, ie^{i\theta})/2$  and  $\Psi(\mathbf{r}, \text{A2}) = (ie^{-i\theta}, 0, \sqrt{2}e^{i\theta}, 0, i)/2$ , respectively, which can not be described as any of the cyclic-tetrahedral vortices. We shall refer to these vortices with the labels A1 and A2, respectively. The core of the  $\text{II}_0$  vortex has  $F_z = 0$  and non-zero particle density. The remaining vortices have normalised magnetised cores with  $F_z = 1$  and  $F_z = -1$ , respectively, and both have a non-zero particle density at the vortex core.

An expanded view of the lattice is shown in Fig. 6.7. As shown in Fig. 6.7(b), non-zero magnetisation density emerges due to the nucleation of vortices with magnetic core structures, which changes the topology of the condensate. The total particle density, see Fig. 6.7(a), does not vanish anywhere although the magnetisation density remains nearly identical to that in Fig. 6.6(e). The spin singlet pair amplitude density in Fig. 6.7(c) reveals the asymmetry between the initial state vortices and those spawned by the condensate collision.

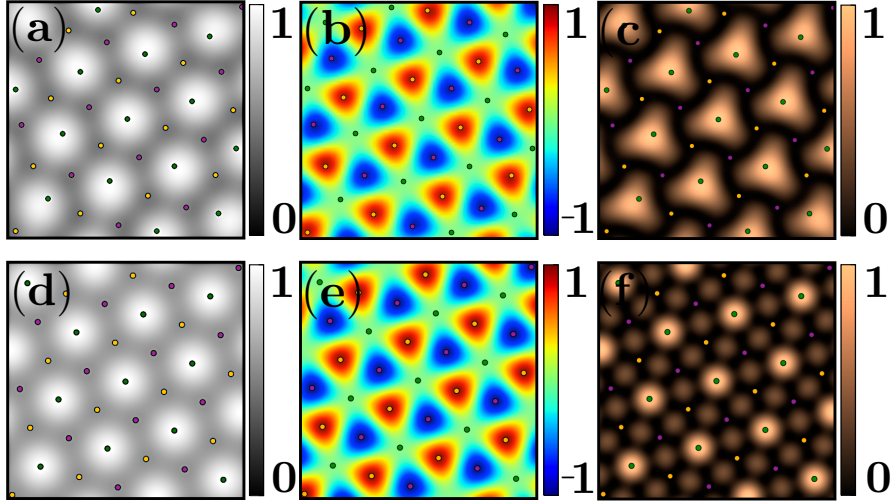


**Figure 6.7:** An expanded view, local to the trap centre, of the lattice for the spin vortex initial state. (a)-(c) The results from a Gross–Pitaevskii simulation showing the total particle density, magnetization density and the spin singlet pair amplitude density for a time  $\tau = 0.55 \, 1/\omega$  after the triple-well trapping potential is switched off. (d)-(f) The corresponding observables calculated with the semi-analytical spinor in Eq. (6.8) where  $\phi_{-2j} = 0, \frac{8\pi}{3}, \frac{4\pi}{3}$ ,  $\phi_{0j} = 0$  and  $\phi_{2j} = 0, \frac{4\pi}{3}, \frac{8\pi}{3}$  for  $j = 1, 2, 3$ , with the other spin components empty. The locations of the  $-\Pi_0$ , A1, and A2 vortices are denoted by coloured dots of green, yellow and purple respectively. The field of view of each frame is  $(2.3 \times 2.3) \, l$ .

Comparing Fig. 6.7(a-c) with Fig. 6.7(d-f), the  $-\Pi_0$ , A1, and A2 vortices have nucleated in the spinor wave function in complete agreement with our semi-analytical model. The triangular structure of the spin singlet pair amplitude density differs from the semi-analytical prediction of a snow-flake pattern illustrating the sensitivity of the spin singlet pair amplitude to relative phase differences between the spin components. The total particle and magnetisation densities are not similarly sensitive to these relative phases. By altering the relative phase differences in the semi-analytical model it is possible to obtain the same level of agreement between the numerical and semi-analytical spin singlet pair amplitude densities as is apparent between Fig. 6.6(c) and (f). The different spin singlet pair amplitude density patterns could be a potential means to measure the phase structure of the spinor order parameter.

We initialise the one third vortex state  $(0, \sqrt{\frac{2}{3}}, 0, 0, \frac{1}{\sqrt{3}} \exp(i\theta))$  by setting the phases  $\phi_{-1j} = 0$  and  $\phi_{2j} = 0, \frac{2\pi}{3}, \frac{4\pi}{3}$  for the  $j = 1, 2, 3$  condensate fragments, respectively, with the other spin components empty. The semi-analytical model of Eq. (6.8) is initialised similarly. The AB stacking produces lattice vortices measured as,  $IV_0$ ,  $IV_{-1}$  and  $-V_0$ . The vortex order parameters are  $\Psi(\mathbf{r}, IV_0) = \frac{1}{\sqrt{3}}(e^{i\theta}, 0, 0, \sqrt{2}, 0)$ ,  $\Psi(\mathbf{r}, IV_{-1}) =$

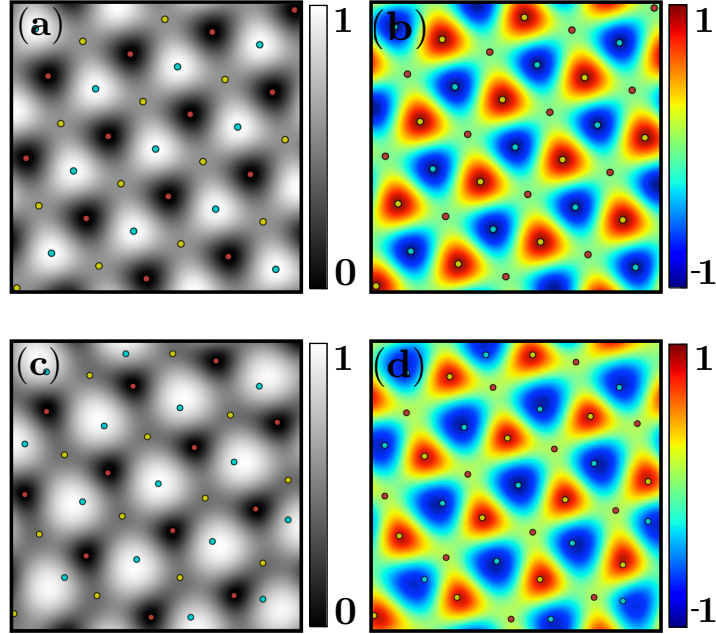


**Figure 6.8:** An expanded view, local to the trap centre, of the lattice for the one third vortex initial state. (a)-(b) The results from a Gross–Pitaevskii simulation showing the total particle density and magnetization density for a time  $\tau = 0.55 1/\omega$  after the triple-well trapping potential is switched off. (c)-(d) The corresponding observables calculated with the semi-analytical spinor in Eq. (6.8) where  $\phi_{-1j} = 0$  and  $\phi_{2j} = 0, \frac{2\pi}{3}, \frac{4\pi}{3}$  for  $j = 1, 2, 3$ , with the other spin components empty. The locations of the  $IV_0$ ,  $IV_{-1}$  and  $-V_0$  lattice vortices are denoted by coloured dots of cyan, yellow and brown respectively. The field of view of each frame is  $(2.7 \times 2.7) l$ .

$\frac{1}{\sqrt{3}}(1, 0, 0, \sqrt{2}e^{-i\theta}, 0)$ , and  $\Psi(\mathbf{r}, -V_0) = \frac{1}{\sqrt{3}}(e^{-i\theta}, 0, 0, \sqrt{2}e^{i\theta}, 0)$ . The topological charges of these vortices commute and hence they obey Abelian collision dynamics.

The particle densities at the cores of the  $IV_0$ ,  $IV_{-1}$  and  $-V_0$  vortices are  $n = \frac{2}{3}n_{\max}$ ,  $\frac{1}{3}n_{\max}$  and 0 respectively, where  $n_{\max}$  is the peak total particle density. Thus the  $-V_0$  vortex has a zero particle density core while the  $IV_0$ ,  $IV_{-1}$  vortex cores have dimensionless magnetizations  $-\frac{2}{3}$  and  $\frac{2}{3}$ , respectively. An expanded view of the lattice structures present in the total particle density and magnetization density is shown in Fig. 6.8(a-b), while the spin singlet pair amplitude density is zero across all space. Note that the vortex cores in both of the non-zero observables have a prominent triangular structure. The vortex lattices and the total density and magnetization density structures are indistinguishable from those predicted by the semi-analytical model.

Based on these three examples, it is clear that the multi-wave interference technique can be used to deterministically produce desired vortex lattice topologies in spinor Bose–Einstein condensates.

## 6.7. Towards two-dimensional non-Abelian quantum turbulence in a spin-2 condensate

As shown in the previous section, the one-third vortex initial states can be used for generating vortex lattices of Abelian vortices and antivortices. Keeping the global harmonic trapping potential turned on and only switching off the triple-well potential will cause the condensate to undergo breathing mode oscillations in the harmonic trap. Figure 6.9(a)-(e) shows snapshots of such a simulation and the frames (f)-(k) show the enlarged images zoomed to the trap centre. Despite the initial three-fold symmetry, the chaotic dynamics of the vortices rapidly leads to the loss of such symmetry and a transition to 2D Abelian quantum turbulence as shown in (c)-(d). The vortex dynamics during the break down of the lattice are dominated by the instability of the  $-V_0$ . After  $\tau = 0.55 \text{ } 1/\omega$ , the  $-V_0$  vortex splits into an antivortex and a vortex in the  $m = 2$  and  $m = -1$  spin-components, respectively. The uncoupled antivortex typically annihilates with the  $IV_0$  vortex, though both vortices may later reform and produce scalar vortex bound states with the  $IV_{-1}$  and the uncoupled vortex, respectively, see Fig. 6.9(g). The decoupling of the  $-V_0$  vortex replaces the interleaved triangular lattice with a hexagonal lattice of scalar vortices.

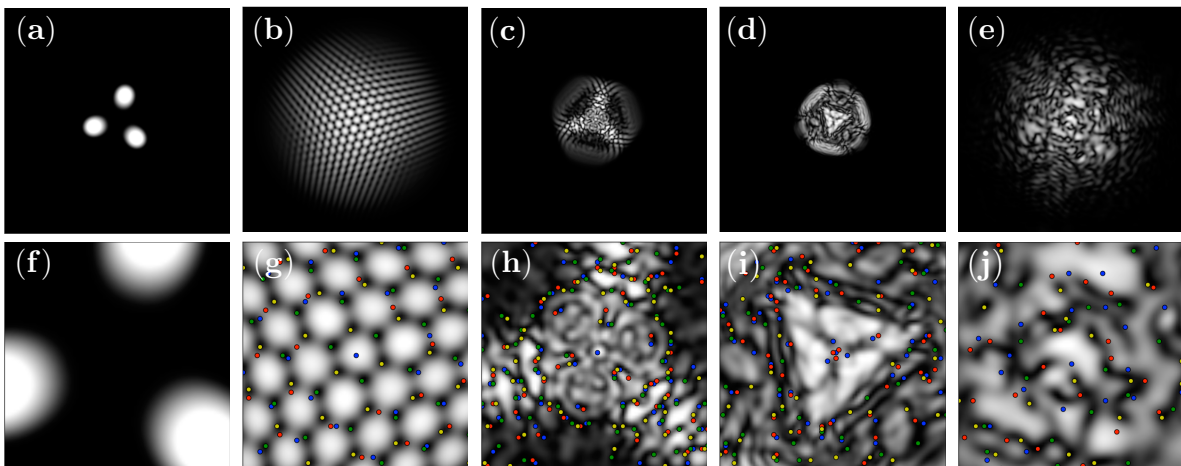


**Figure 6.9:** Emergence of non-Abelian two-dimensional quantum turbulence showing a selection of snapshots from the one third initial state simulation. (a)-(e): The total probability density of the condensate including the initial state, lattice and turbulent regime. The field of view of each frame is  $(29.2 \times 29.2) l$ . (f)-(k): The same frames in (a)-(e) but with a field of view of  $(2.92 \times 2.92) l$ . The coloured dots of blue, red, green and yellow denote the vortices (blue/green) and antivortices (red/yellow) in the  $m = 2$  and  $m = -1$  spin states, respectively.

The collective excitations, such as the breathing mode, excited after the collisions of the condensate fragments, obscure the vortex dynamics in the turbulent state. Thus, rather than using three source interference, in a harmonic trap, we can instead phase imprint the initial vortex configuration into a 2D uniform trap, as used in the recent scalar 2D quantum turbulence experiments [104, 105]. By suppressing the collective excitations and smoothing the condensate density profile, we obtain a cleaner system to visualise the topological interactions. Furthermore, by phase imprinting the vortices, we can control the algebra of their charges, allowing for the potential realisation of both Abelian and non-Abelian 2D quantum turbulence.

Initial states of disordered arrays of vortices are imprinted using the techniques outlined in Sec. 3.2. Abelian vortex initial states, where the topological charges of all the vortices commute, are created directly from the product states in Eq. (3.4). In Figure 6.10, we provide an initial state of  $IV_0$  and  $-VI_{-1}$  vortices, which seeds an Abelian quantum turbulent state. Initial states of non-Abelian vortices are realised by using the phase matching technique to construct a cell of four vortices, two of each charge, which are then tiled across the condensate to imprint many non-Abelian vortices. Figure 6.11(a)-(e), shows such a phase structure for the non-Abelian vortices  $IV_0$  and  $-VI_{-1}^x$ . The boundaries between the different vortex order parameters introduce domain walls, as evidenced by the observable densities in Fig. 6.11(g)-(h). The decay of these domain walls is a source of noise, in the form of sound waves, magnons and spurious vortices. However, the energy released from the decaying domain walls could be beneficial, by stimulating the onset of turbulent dynamics.

Evolving the initial states in Figs. 6.10 and 6.11 produces a turbulent state. Each system is evolved for a period of dimensionless time  $\tau = 2000$ , where  $\tau = t\omega'$  and the angular frequency  $\omega' = 2\pi \times 10$  Hz. To make a preliminary characterisation of these turbulent states we consider the vortex number decay, see Fig. 6.12 and spectra of the incompressible kinetic energy, see Eq. (6.2), shown in Figs. 6.13 and 6.14. A thorough analysis of the turbulent states would perform ensemble averaging over many simulations with different initial state vortex configurations.

Our identification methodology for spinor vortices, see Sec. 3.3, fails for many-vortex systems in which the vortices are both irregularly and densely distributed, as is the case in these turbulent states. In such situations, the measured spherical harmonic series of a vortex is perturbed by the order parameter transformations of neighbouring vortices outside the measurement loop, prohibiting accurate overlap measurements. Furthermore, measurements of the total rotation of the order parameter across the measured series

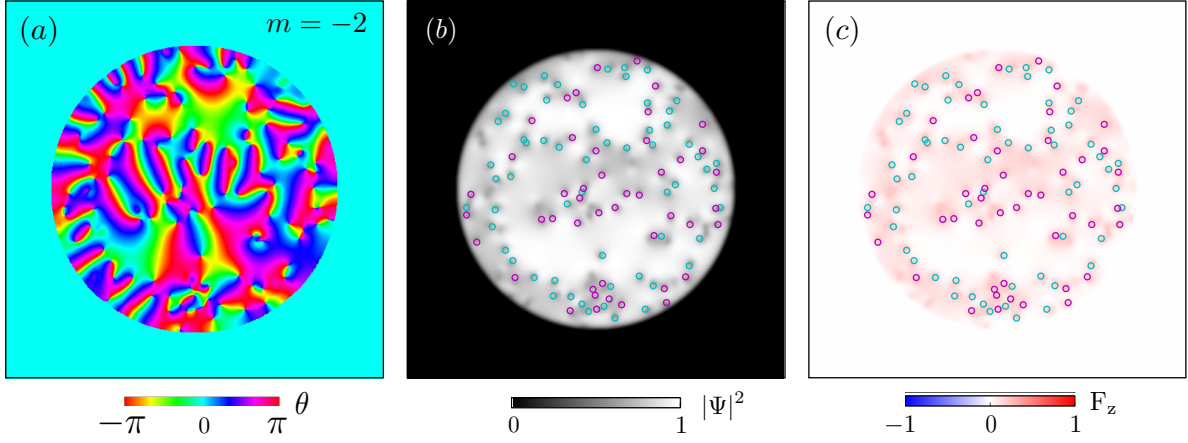


**Figure 6.10:** An initial state of 95 Abelian vortices with topological charges  $IV_0$  (42) and  $-VI_{-1}$  (53). (a) The phase  $\theta$  of the  $m = -2$  spin component which contains the phase windings of the  $IV_0$  and  $-VI_{-1}$  vortices. (b) The total density,  $|\Psi|^2$ . (c) The magnetization density,  $F_z$ . The locations of the  $IV_0$  and  $-VI_{-1}$  vortices are denoted by the magenta and cyan circles, respectively. The radius of the hard-wall trapping potential is  $R_{\text{hw}} \approx 58\mu m$ .

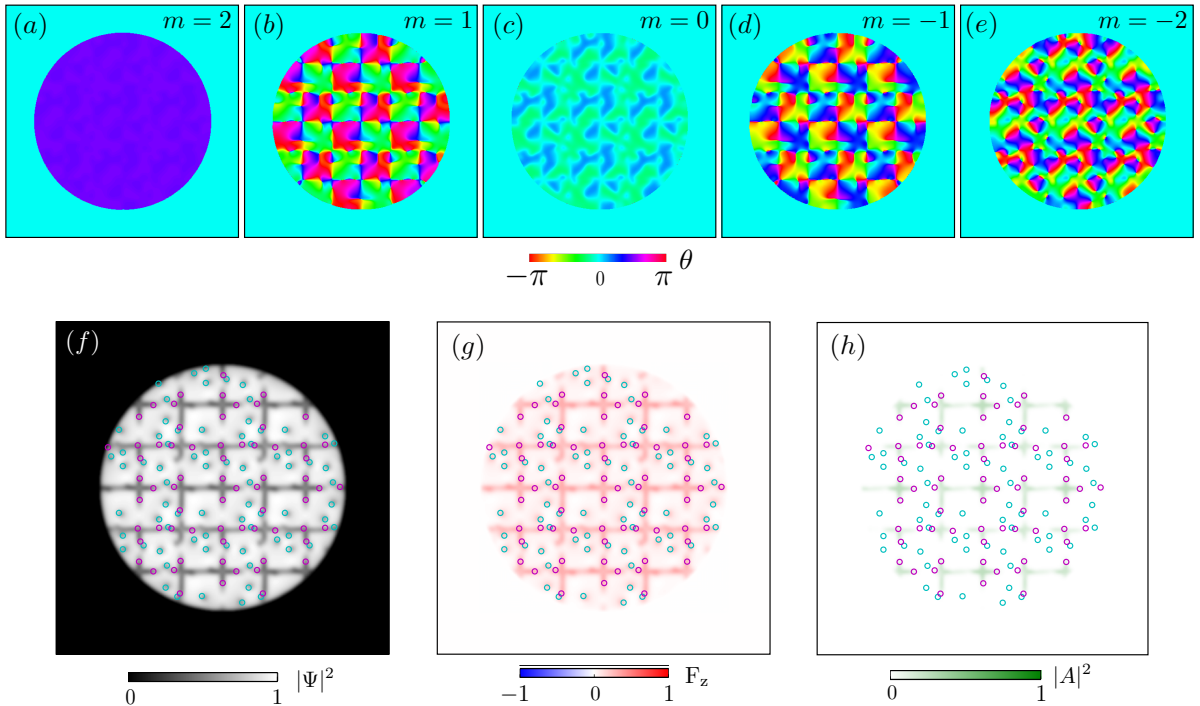


**Figure 6.11:** An initial state of 100 non-Abelian vortices with topological charges  $IV_0$  (50) and  $-VI_{-1}^x$  (50). (a)-(e) The phases  $\theta$  of the  $m = -2, \dots, 2$  spin components. (f) The total density,  $|\Psi|^2$ . (g) The magnetization density,  $F_z$ . (h) The spin-singlet pair amplitude,  $|A|^2$ . The locations of the  $IV_0$  and  $-VI_{-1}^x$  vortices are denoted by the magenta and cyan circles, respectively, corresponding to the phase windings in the  $m = -2$  spin component. The radius of the hard-wall trapping potential is  $R_{\text{hw}} \approx 58\mu m$ .

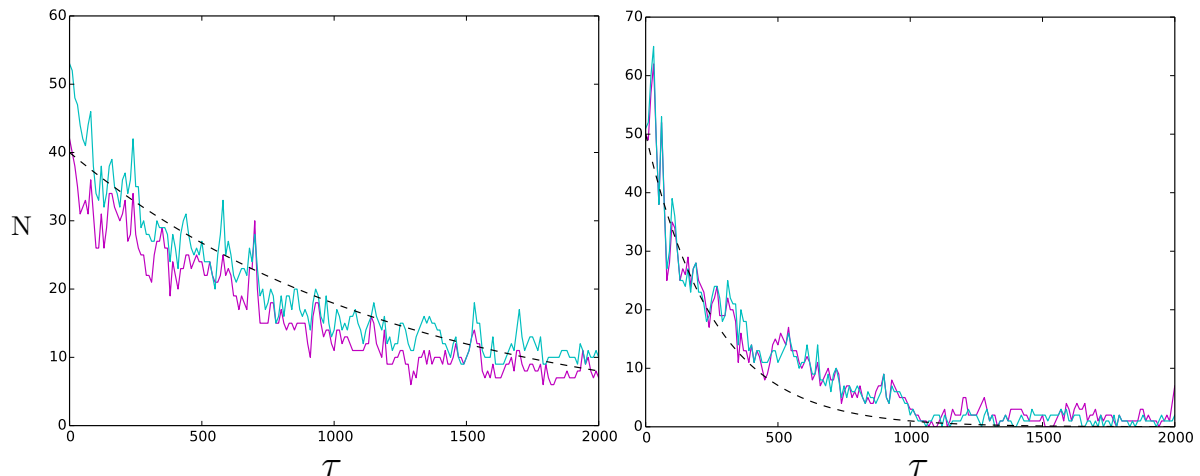


**Figure 6.12:** Vortex number decay curves for quantum turbulent states of, (a) Abelian vortices, and (b) non-Abelian vortices. The magenta and cyan curves give the number  $N$ ; of  $IV_0$  and  $-VI_{-1}$  vortices in (a), respectively; and  $IV_0$  and  $-VI_{-1}^x$  vortices in (b), respectively. In each subfigure, we provide a reference exponential decay curve, dashed black line, of form  $B_1 e^{-t/B_2}$ , with parameters  $B_1 = \{40, 50\}$  and  $B_2 = \{1243, 256\}$ , for the curves in (a) and (b), respectively.

are hampered by insufficient spatial sampling of the order parameter. Thus, rather than performing a direct count of the vortex types, we locate and count the correlated phase windings, which are typically present in only one component of the order parameter. To avoid counting spurious vortices, which can be excited via pair creation in regions with near-zero density, we smooth the phase by transforming the order parameter into Fourier space and thresholding the high energy modes. Counting the phase windings in the  $m = -2$  spin component, we obtain effective vortex number decay curves for the  $IV_0$  and  $-VI_{-1}$  vortices in the Abelian turbulent state, see Fig. 6.12(a), and for the  $IV_0$  and  $-VI_{-1}^x$  vortices in the potentially non-Abelian turbulent state, see Fig. 6.12(b). As the turbulence progresses, there is a notably steeper decay in the number of the initial state vortices left in the system in the non-Abelian case in comparison to the Abelian state. By comparing the curves in each turbulent state to an exponential decay  $B_1 e^{-t/B_2}$  we obtain mean lifetimes of  $B_2 = \{1242, 256\}$  for the Abelian and non-Abelian cases, respectively. Indeed, by  $\tau = 1000$  for the non-Abelian case, it appear as if there are few or no vortices left in the system at all. However, the collisions of the non-Abelian  $IV_0$  and  $-VI_{-1}^x$  vortices induce rungihilation events that spawn rung vortices of kind class III. Since the order parameters of the class III vortices do not necessarily contain explicit, and thus locatable, phase windings, the rung vortices are absent from the count.

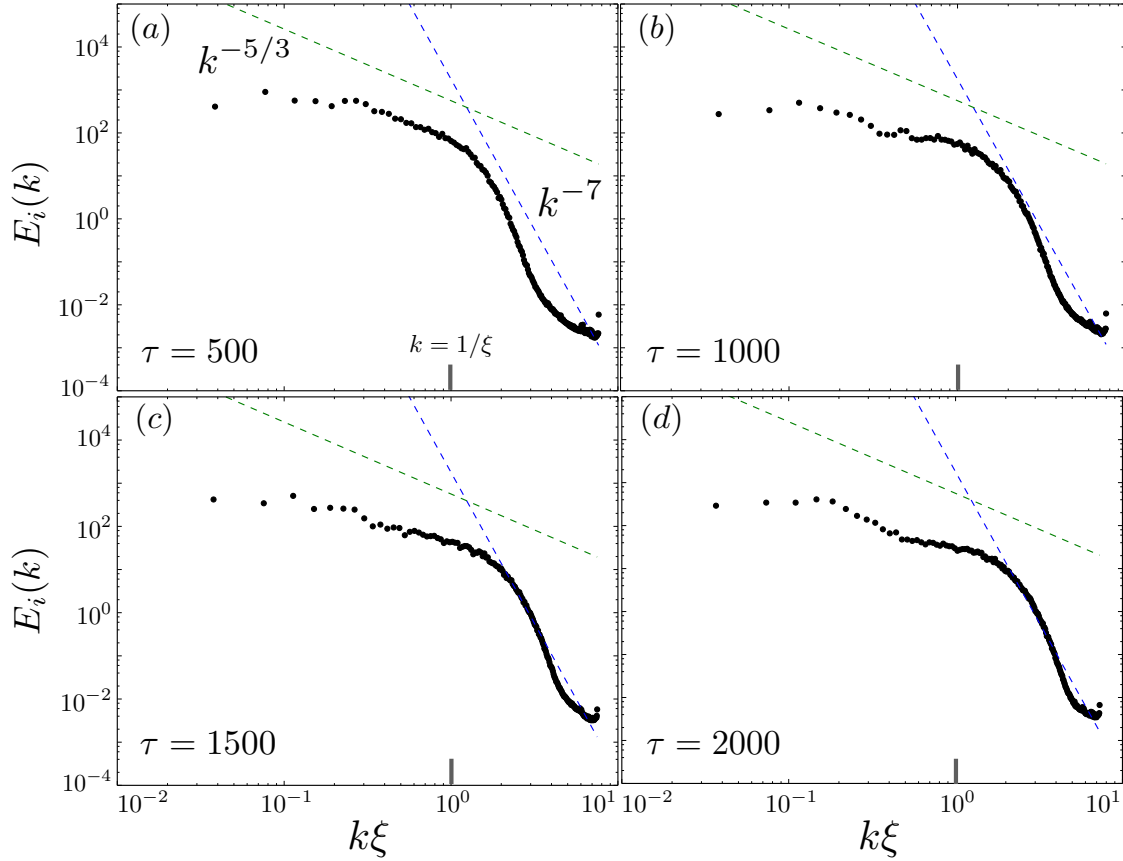


**Figure 6.13:** Spectra of the incompressible kinetic energy  $E_i(k)$  for the quantum turbulent state of Abelian vortices. The wavevector is scaled with respect to the density healing length to  $\xi$ . As a guide to the eye, we provide the green and blue dotted lines corresponding to the  $k^{-5/3}$  and  $k^{-7}$  power laws, respectively.

In Figures. 6.13 and 6.14, we provide spectra of the incompressible kinetic energy at multiple timesteps during the evolution of the turbulent states of Abelian and non-Abelian vortices, respectively. In the Abelian case, in the region  $K\xi > 1$  there appears to be some tendency towards the Kolmogorov  $k^{-5/3}$  power law, which appears in some numerical [264–266] and experimental [105] studies of scalar 2D Abelian quantum turbulence [132]. While the spectra for the Abelian and non-Abelian cases are initially similar, see Figs. 6.14(a)-(b), for  $\tau > 1000$  an unusual “flat” spectrum develops. The exact mechanism driving the flatness of the spectra is unclear. However, a possible connection may be the transference of kinetic energy in the mass current circulations of the  $IV_0$  and  $-VI_{-1}^x$  vortices to the spin current circulation of the rung vortices. In both the Abelian and non-Abelian spectra, the scaling in the region  $k\xi < 1$ , associated with the vortex core, is distinctly different to the  $k^{-3}$  power law in scalar 2D quantum turbulence, perhaps associated with the populated spinor vortex core structures.

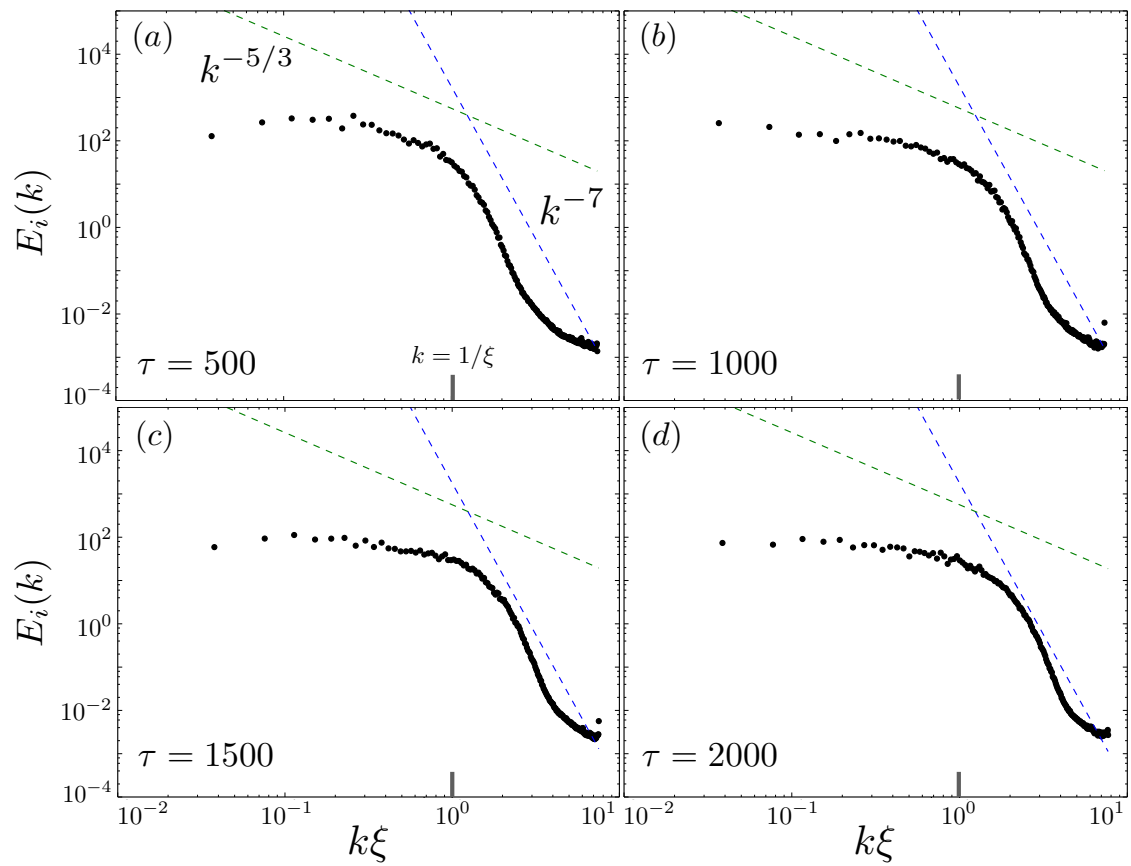


**Figure 6.14:** Spectra of the incompressible kinetic energy  $E_i(k)$  for the quantum turbulent state of non-Abelian vortices. The wavevector is scaled with respect the density healing length to  $\xi$ . As a guide to the eye, we provide the green and blue dotted lines corresponding to the  $k^{-5/3}$  and  $k^{-7}$  power laws, respectively.

## 6.8. Summary

We have studied computationally the generation of quantised vortex lattices and quantum turbulence in spin-2 spinor Bose–Einstein condensates by simulating collisions of three condensate fragments. We have shown that the structure of the resulting honeycomb vortex lattices can be predicted by modelling each of the spinor wave function components independently in terms of linear superposition of three waves. The lattice states thus produced, correctly predict the structure of fractional-vortex lattices observed in full simulations of the spinor Gross–Pitaevskii equation.

We have shown that using realistic initial state preparation, honeycomb lattices of fractional-charge vortices with commuting topological charges can be produced using a three wave interference technique. It remains to be seen if initial phase configurations can be realised which produce lattices of non-Abelian vortices. The generated vortex lattices are robust even in the presence of fairly large phase fluctuations because any such uncertainties would only act to translate the vortex positions in each spin component and small shifts in the vortex positions are not sufficient to destroy the topology of the vortices. This technique is anticipated to open a route to experimental studies of quantum turbulence in spinor Bose–Einstein condensates. Despite the relatively short life-times of the  $F = 2$  Bose–Einstein condensates, the dynamical method presented for creating the honeycomb vortex lattices and their subsequent decay to turbulence should allow sufficiently long time scales for observations of quantum turbulence to be made. The resulting vortex configurations could potentially be observed using the vortex sign detection methods [105, 294, 295] in combination with Stern–Gerlach imaging.

We studied turbulent states of vortices, with either commuting or non-commuting topological charges, by directly phase imprinting disordered configurations of vortices into a uniform condensate. Noticeable differences were observed between the two turbulent states regarding the rate of vortex number decay and the kinetic energy spectra. Such differences act as a potential indicator that the non-Abelian algebra manifests a different kind of 2D non-Abelian quantum turbulence. There remain many open questions in this context; what mechanism is causing the non-Kolmogorov power law in the incompressible kinetic energy spectra of the non-Abelian turbulent state?; can evaporative heating of fractional vortices lead to the emergence of Onsager vortices of non-Abelian kind [261, 263]?; and does magnetization cascade emerge in these systems alongside incompressible kinetic energy and enstrophy cascades? These important questions are left as topics for further studies.



# Chapter 7.

## Conclusions

In this thesis we presented an investigation into the topological interactions of non-Abelian vortices in spin-2 spinor Bose–Einstein condensates. We studied these interactions in increasingly complex systems, starting with two vortex collisions, then extending to few vortex explorations of the braiding and fusion dynamics of non-Abelian vortex anyons, and finally modelling chaotic many-vortex dynamics of quantum turbulence.

In Chapter 4, we discussed the topological interactions of spinor vortices by characterising the collision dynamics of vortex dipoles with both commuting and non-commuting topological charges. Abelian vortices were found to undergo annihilation, mediated by a magnetic soliton state, and pass through. For non-Abelian vortices we discovered a new collision event—rungihilation—in which a vortex pair collides forming a rung vortex and subsequently decays forming a further non-Abelian vortex pair with different topological charges. The observed collision dynamics were mapped onto, and explained in terms of the fusion rules, of the corresponding vortex anyons.

In Chapter 5 we observed that the topological influence between non-Abelian vortices results in braiding and fusion dynamics that are characteristic of non-Abelian anyons. We developed and characterised non-Abelian vortex anyon models based on the quantum double construction, where the vortices were mapped to particle-like excitations called fluxons and additional  $H$ -charges were introduced. Beginning at the fluxon level, We derived the fusion rules for these anyons by mapping between the flux fusion rules and the vortex collision dynamics discussed in Chap. 4, and subsequently including the  $H$ -charge property. We constructed a toy-model for a topological qubit and demonstrated the actions required to perform a single qubit superposition operation and a two-qubit entangling operation. While our non-Abelian vortices were demonstrated to have the potential to yield non-Abelian anyons, we noted that this may be compromised by the

substantial challenge of creating and maintaining true quantum superpositions of fluxon eigenstates necessary to create useful qubit states in real superfluid systems.

Finally, in Chapter 6 we demonstrated the use of three-source interference of spin-2 condensate fragments to deterministically generate lattices of Abelian fractional-charge vortices. Furthermore, we showed that three-source interference is a potential route to quantum turbulence in spinor condensates. We performed preliminary studies of quantum turbulent states of vortices with either commuting or non-commuting topological charges, observing potential indicators of a new kind of non-Abelian quantum turbulence.

In this work we obtained answers to a number of questions regarding the basic topological interactions of non-Abelian vortices, their potential applications to quantum computation and the expanding knowledge of quantum turbulence phenomena. As the research progressed a number of tantalising unexplored avenues were revealed.

Vortex-antivortex annihilation was observed, in Chapter 4, to be mediated by the formation of a magnetic Jones-Roberts soliton, with true annihilation likely requiring some many-body scattering process. The specific details of this annihilation process may help reveal the mechanisms underlying the properties of 2D Abelian quantum turbulence in spinor condensates. In three dimensions, our vortex dipole orbits map to co-propagating elongated axisymmetric vortex lines. It has been demonstrated that such motion for scalar vortex lines seeds a Crow instability [296, 297], where the mutual induction field of the dipole excites Kelvin waves along the vortex lines which grow in amplitude until the vortices reconnect to form many vortex rings. It would be interesting to explore whether the crow instability exists for non-Abelian vortices, where rung formation might instead lead to a chain of linked vortex rings. Our results in Chapter 5 provide a number of avenues for further research. Foremost, is a thorough investigation of the potential to create and maintain true flux superposition states in a BEC with a macroscopic number of atoms. Such superpositions may be more readily realised in condensates in the few-atom limit. Supposing fluxon superpositions could be realised, it would be up to experiments to determine their decoherence time. We postulate that the  $H$ -charges would correspond to Bogoliubov ‘zero’ modes realised on a given vortex order parameter background. These excitations could be characterised, by solving the Bogoliubov–de Gennes equation for the spin-2 BEC [119], and mapped onto the  $H$ -charges by comparison with the representation theory. There is also great potential to explore Cheshire charge in these systems. We have already begun an investigation into the magnetic soliton structure, revealed in our single qubit simulations, and its potential connection to the Cheshire charge. For the three-source interference technique in Chapter 6, realising initial

---

phase configurations which result in vortex lattices with non-Abelian vortices remains an open problem. Our preliminary turbulence results point towards a number of interesting research opportunities. Exhaustive numerical simulations could provide more accurate power laws in the spectra of the incompressible kinetic energy. Similarly, amending the vortex detection method, such that it can robustly detect and identify vortices of all types in dense vortex configurations, would permit a more accurate measure of the vortex number decay. The analysis could also be expanded to calculate spectra of the spin interaction energy. There are also rich connections that could be made to coarsening dynamics [298], particularly in the magnetisation, and to non-thermal fixed points [299].

Topology in physics is presently undergoing a resurgence, to which this thesis makes a contribution. The novel topological interactions of non-Abelian vortices provide the possibility of uncovering fascinating new physics in 2D spinor condensate systems; potentially including non-Abelian vortex anyons and a new kind of non-Abelian quantum turbulence. Quantum turbulence and quantum computation may appear to be quite disparate systems, yet in the context of this thesis they are connected via the non-Abelian vortex anyons. Indeed, the chaotic braiding and fusions of vortices in a quantum turbulent state could be viewed as a form of stochastic quantum computation. Even if the vortices would not turn out to be true non-Abelian anyons, they still (even at mean-field level) have the unusual topological influence and rung formation dynamics. These interesting topological interactions alone are a major motivation for further studies to pave the way for future experimental verification. We hope that this work contributes toward encouraging the experimental realisation of these exciting non-Abelian topological structures.



# Appendix A.

## Spin-2 rotation matrix

The  $5 \times 5$  matrix representation of the phase and spin rotation of the spin-2 BEC order parameter is

$$R = e^{i\phi} \begin{pmatrix} e^{-2i(\alpha+\gamma)}C^4 & -2e^{-i(2\alpha+\gamma)}C^3S & \sqrt{6}e^{-2i\alpha}C^2S^2 & -2e^{-i(2\alpha-\gamma)}CS^3 & e^{-2i(\alpha-\gamma)}S^4 \\ 2e^{-i(\alpha+2\gamma)}C^3S & e^{-i(\alpha+\gamma)}C^2(C^2 - 3S^2) & -\sqrt{\frac{3}{8}}e^{-i\alpha}\sin(2\beta) & -e^{-i(\alpha-\gamma)}S^2(S^2 - 3C^2) & -2e^{-i(\alpha-2\gamma)}CS^3 \\ \sqrt{6}e^{-2i\gamma}C^2S^2 & \sqrt{\frac{3}{8}}e^{-i\gamma}\sin(2\beta) & \frac{1}{4}(1 + \cos(2\beta)) & -\sqrt{\frac{3}{8}}e^{i\gamma}\sin(2\beta) & \sqrt{6}e^{2i\gamma}C^2S^2 \\ 2e^{i(\alpha-2\gamma)}CS^3 & -e^{i(\alpha-\gamma)}S^2(S^2 - 3C^2) & \sqrt{\frac{3}{8}}e^{i\alpha}\sin(2\beta) & e^{i(\alpha+\gamma)}C^2(C^2 - 3S^2) & -2e^{i(\alpha+2\gamma)}C^3S \\ e^{2i(\alpha-\gamma)}S^4 & 2e^{i(2\alpha-\gamma)}CS^3 & \sqrt{6}e^{2i\alpha}C^2S^2 & 2e^{i(2\alpha+\gamma)}C^3S & e^{2i(\alpha+\gamma)}C^4 \end{pmatrix}, \quad (\text{A.1})$$

where  $C = \cos(\frac{\beta}{2})$  and  $S = \sin(\frac{\beta}{2})$  [119].



## Appendix B.

### Cyclic-tetrahedral non-Abelian vortices

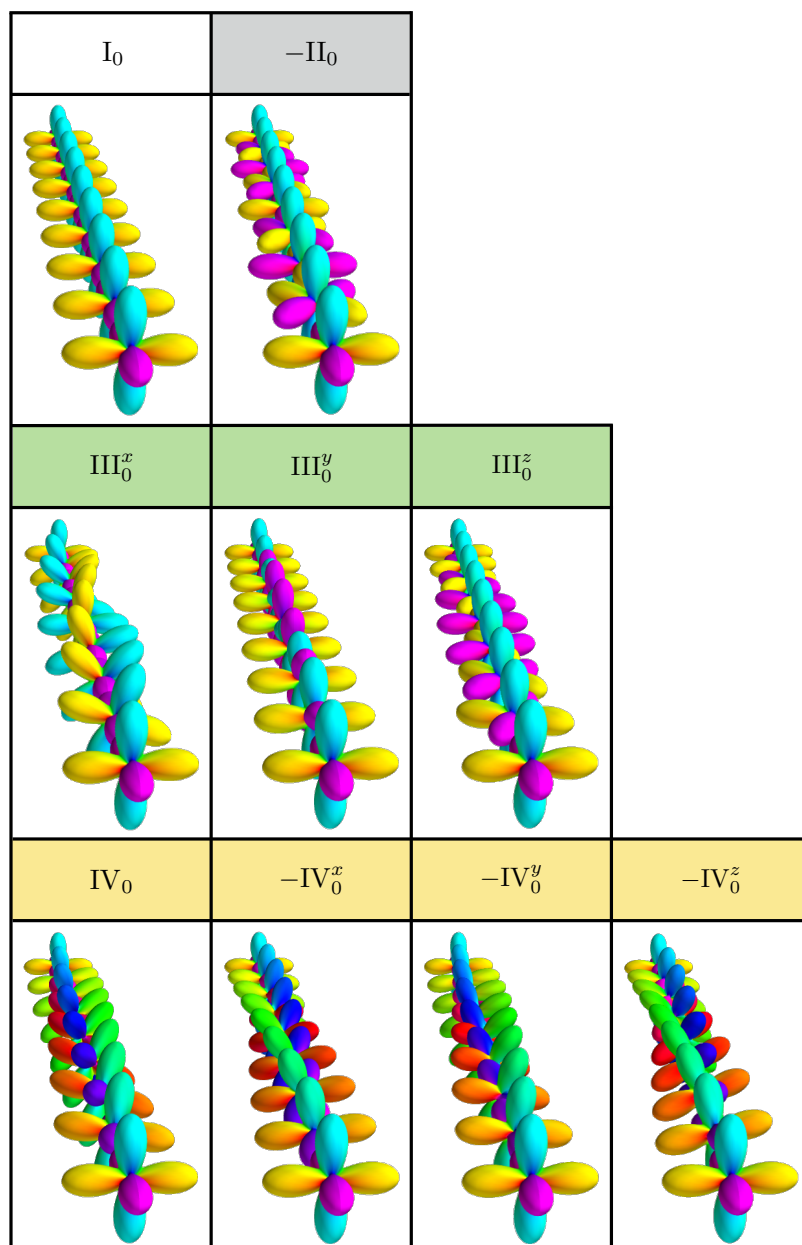


**Figure B.1:** Order parameter transformations of the cyclic-tetrahedral phase vortices in Fig. 2.4 viewed along the axis of the sequence. Order parameter traverses out of the page for the given labels and into the page for their inverses.

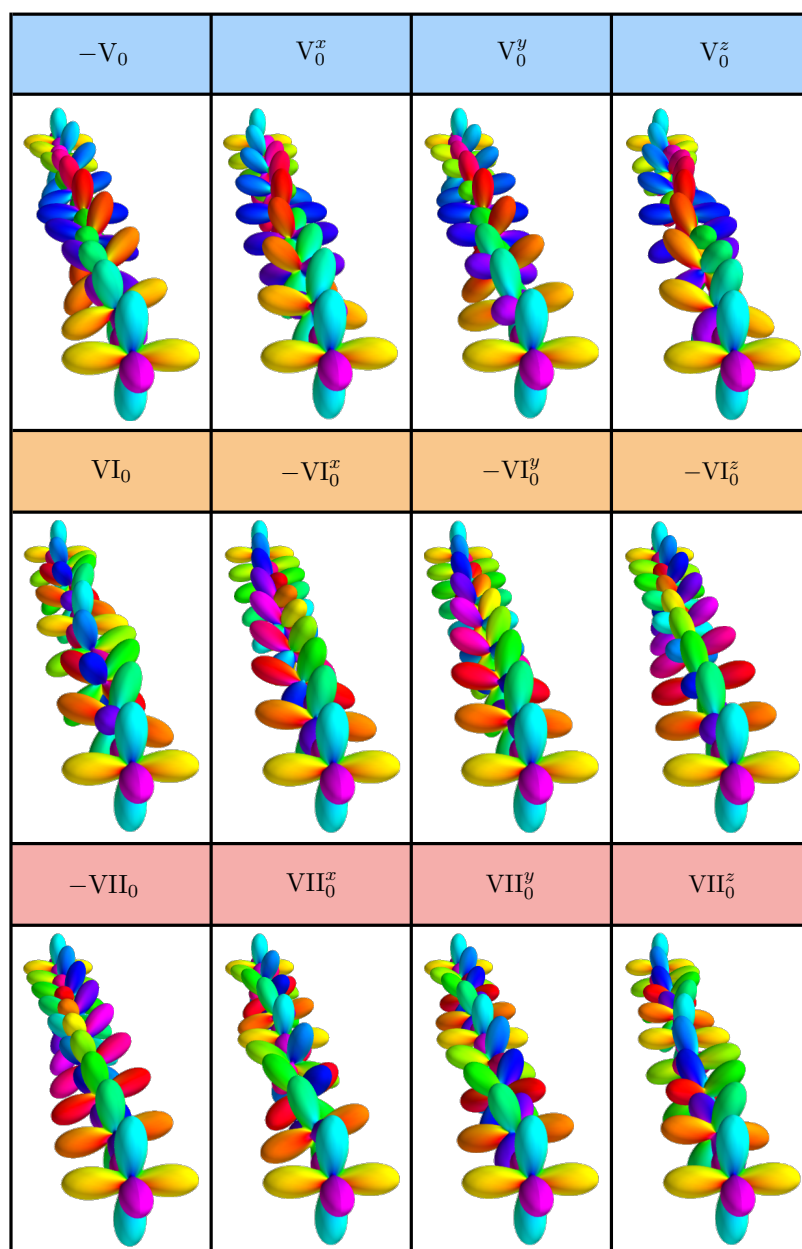


**Figure B.2:** Order parameter transformations of the cyclic-tetrahedral phase vortices in Fig. 2.4 viewed along the axis of the sequence. Order parameter traverses out of the page for the given labels and into the page for their inverses.



# Appendix C.

## Representation theory

The unitary representations of a finite group  $H$  correspond to homomorphisms  $\alpha : H \rightarrow GL(V)$  which map the group elements onto a set of unitary linear operators (matrices) on a vector space  $V$ , for a detailed description see Ref. [300]. For a particular representation, the identity element  $e$  is mapped onto the identity operator,  $\alpha(e) = \mathbb{I}$ , and the group operation is carried over into the multiplication of the unitary operators,  $\alpha(\gamma_1)\alpha(\gamma_2) = \alpha(\gamma_1\gamma_2)$ . The dimension of the associated vector space defines the dimension of the representation.

We define a subspace  $W \subset V$  as invariant if  $\alpha(\gamma)w \in W$  for all  $\gamma \in H$  and  $w \in W$ . A representation is defined to be irreducible if the only invariant subspaces are trivial, e.g. the vector space  $V$  or the set  $\{0\}$ . The irreducible representations of a group are in one-to-one correspondence with the equivalency classes of the group. Hence, the number of irreducible representations is the same as the number of equivalency classes of the group.

A useful way to look at the representations of a group is through their characters. The characters  $\chi_\alpha$  of a representation  $\alpha$  are defined as the traces of the corresponding unitary operators

$$\chi_\alpha(\gamma) \equiv \text{Tr}\alpha(\gamma) = \sum_i [\alpha(\gamma)]_{ii}. \quad (\text{C.1})$$

The nonequivalent irreducible representations have different sets of characters, however the character table does not determine the representations up to isomorphism. Additionally, since the trace is unaffected by the action of an equivalency operation on the group elements, each element of an equivalency class shares the same character. The characters also provide a simple way to decompose a tensor product of representations into a direct

sum of irreducible representations, i.e.  $\alpha_1 \otimes \alpha_2 = \bigoplus_i N_i \alpha_i$ , where  $N_i$  is a multiplicity. A representation constructed from a tensor product or a direct sum of irreducible representations  $\alpha_1$  and  $\alpha_2$  has characters  $\chi_{\alpha_1 \otimes \alpha_2} = \chi_{\alpha_1} \chi_{\alpha_2}$  or  $\chi_{\alpha_1 \oplus \alpha_2} = \chi_{\alpha_1} + \chi_{\alpha_2}$ , respectively. Thus to determine the decomposition of the tensor product we need to find the sum of characters with non-zero multiplicities, such that  $\chi_{\alpha_1 \otimes \alpha_2} = \sum_i N_i \chi_{\alpha_i}$ .

As an example consider the representations of the group  $T^*$ , the corresponding character table is given in Table C.1. Every group has the trivial representation,  $\alpha(\gamma) = 1$  for all  $\gamma \in H$ , represented here as T0. The characters of the trivial representation are evidently  $\chi_{T0}(\gamma) = 1$ . The group has two further one-dimensional representations T1 and T2, with the former case defined directly from the characters as  $\alpha(\text{I, II, III}) \rightarrow 1$ ,  $\alpha(\text{IV, V}) \rightarrow \theta$ ,  $\alpha(\text{VI, VII}) \rightarrow \theta^*$ , where  $\theta = e^{i2\pi/3}$ . Since  $T^*$  is a non-Abelian group it must have some representations where the elements are matrices, in particular the representations T3 – T6. Of these matrix representations, T3 is three-dimensional and defined as

$$\begin{aligned} \alpha(\text{I, II}) &\rightarrow \begin{pmatrix} 1 & 0 & 0 \\ 0 & 1 & 0 \\ 0 & 0 & 1 \end{pmatrix}, & \alpha(\text{III}_0^x, -\text{III}_0^x) &\rightarrow \begin{pmatrix} 1 & 0 & 0 \\ 0 & -1 & 0 \\ 0 & 0 & -1 \end{pmatrix}, \\ \alpha(\text{III}_0^y, -\text{III}_0^y) &\rightarrow \begin{pmatrix} -1 & 0 & 0 \\ 0 & 1 & 0 \\ 0 & 0 & -1 \end{pmatrix}, & \alpha(\text{III}_0^z, -\text{III}_0^z) &\rightarrow \begin{pmatrix} -1 & 0 & 0 \\ 0 & -1 & 0 \\ 0 & 0 & 1 \end{pmatrix}, \\ \alpha(\text{IV}_0, -\text{V}_0) &\rightarrow \begin{pmatrix} 0 & 1 & 0 \\ 0 & 0 & 1 \\ 1 & 0 & 0 \end{pmatrix}, & \alpha(-\text{IV}_0^x, \text{V}_0^x) &\rightarrow \begin{pmatrix} 0 & 1 & 0 \\ 0 & 0 & -1 \\ -1 & 0 & 0 \end{pmatrix}, \\ \alpha(-\text{IV}_0^y, \text{V}_0^y) &\rightarrow \begin{pmatrix} 0 & -1 & 0 \\ 0 & 0 & 1 \\ -1 & 0 & 0 \end{pmatrix}, & \alpha(-\text{IV}_0^z, \text{V}_0^z) &\rightarrow \begin{pmatrix} 0 & -1 & 0 \\ 0 & 0 & -1 \\ 1 & 0 & 0 \end{pmatrix} \end{aligned}$$

$$\begin{aligned}
\alpha(-VI_0, VII_0) &\rightarrow \begin{pmatrix} 0 & 0 & 1 \\ 1 & 0 & 0 \\ 0 & 1 & 0 \end{pmatrix}, & \alpha(-VI_0^x, VII_0^x) &\rightarrow \begin{pmatrix} 0 & 0 & 1 \\ -1 & 0 & 0 \\ 0 & -1 & 0 \end{pmatrix}, \\
\alpha(-VI_0^y, VII_0^y) &\rightarrow \begin{pmatrix} 0 & 0 & -1 \\ 1 & 0 & 0 \\ 0 & -1 & 0 \end{pmatrix}, & \alpha(-VI_0^z, VII_0^z) &\rightarrow \begin{pmatrix} 0 & 0 & -1 \\ -1 & 0 & 0 \\ 0 & 1 & 0 \end{pmatrix}. \quad (C.2)
\end{aligned}$$

The representation corresponding to the tensor product  $T3 \otimes T3$  has the characters shown in the table below:

Class	I	II	III	IV	V	VI	VII
$T3 \otimes T3$	9	9	1	0	0	0	0

The above characters are equivalent to those obtained from the sum  $\chi_{T0} + \chi_{T1} + \chi_{T2} + 2\chi_{T3}$ , where the multiplicity  $N_{T3} = 2$ . Thus the tensor product is decomposed as  $T3 \otimes T3 = T0 \oplus T1 \oplus T2 \oplus 2T3$ .

We similarly provide the character table of  $D_4^*$ , which is the isotropy group of the biaxial nematic phase, and of the centralizer groups  $\mathbb{Z}_4 (T^*, D_4^*)$ ,  $\mathbb{Z}_6 (T^*)$ ,  $\mathbb{Z}_8 (D_4^*)$ , in Tables C.2-C.5, respectively.

Class	I	II	III	IV	V	VI	VII
T0	1	1	1	1	1	1	1
T1	1	1	1	$\theta$	$\theta$	$\theta^*$	$\theta^*$
T2	1	1	1	$\theta^*$	$\theta^*$	$\theta$	$\theta$
T3	3	3	-1	0	0	0	0
T4	2	-2	0	-1	1	1	-1
T5	2	-2	0	$-\theta^*$	$\theta^*$	$\theta$	$-\theta$
T6	2	-2	0	$-\theta$	$\theta$	$\theta^*$	$-\theta^*$

**Table C.1:** Character table of the binary tetrahedral group  $T^*$  [301], which is isomorphic to  $SL(2, 3)$ . The 3rd root of unity is denoted by  $\theta = e^{i2\pi/3}$ .

Class	I	II	III	IV	V	VI	VII
D0	1	1	1	1	1	1	1
D1	1	1	-1	1	1	1	-1
D2	1	1	1	1	-1	-1	-1
D3	1	1	-1	1	-1	-1	1
D4	2	-2	0	-2	0	0	0
D5	4	-4	0	0	$2\sqrt{2}$	$-2\sqrt{2}$	0
D6	4	-4	0	0	$-2\sqrt{2}$	$2\sqrt{2}$	0

**Table C.2:** Character table of the binary dihedral-4 group  $D_4^*$  [302] which is isomorphic to the dicyclic-4 group  $Dic_4$ .

Class	$x^0$	$x^1$	$x^2$	$x^3$
$Z_40$	1	1	1	1
$Z_41$	1	1	-1	-1
$Z_42$	1	-1	$-i$	$i$
$Z_43$	1	-1	$i$	$-i$

**Table C.3:** Character table of the group  $Z_4$  which is a centralizer group of  $T^*$  and  $D_4^*$ .

Class	$x^0$	$x^1$	$x^2$	$x^3$	$x^4$	$x^5$
Z <sub>6</sub> 0	1	1	1	1	1	1
Z <sub>6</sub> 1	1	-1	1	1	-1	-1
Z <sub>6</sub> 2	1	1	$\omega^4$	$\omega^2$	$\omega^2$	$\omega^4$
Z <sub>6</sub> 3	1	-1	$\omega^4$	$\omega^2$	$\omega^5$	$\omega$
Z <sub>6</sub> 4	1	1	$\omega^2$	$\omega^4$	$\omega^4$	$\omega^2$
Z <sub>6</sub> 5	1	-1	$\omega^2$	$\omega^4$	$\omega$	$\omega^5$

**Table C.4:** Character table of the group  $\mathbb{Z}_6$  which is a centralizer group of  $T^*$ . The 6th root of unity is denoted by  $\omega = e^{i2\pi/6}$ .

Class	$x^0$	$x^1$	$x^2$	$x^3$	$x^4$	$x^5$	$x^6$	$x^7$
Z <sub>8</sub> 0	1	1	1	1	1	1	1	1
Z <sub>8</sub> 1	1	1	1	1	-1	-1	-1	-1
Z <sub>8</sub> 2	1	-1	$i$	$-i$	$\zeta^7$	$\zeta^5$	$\zeta^3$	$\zeta$
Z <sub>8</sub> 3	1	1	-1	-1	$-i$	$i$	$-i$	$i$
Z <sub>8</sub> 4	1	-1	$-i$	$i$	$\zeta^5$	$\zeta^7$	$\zeta$	$\zeta^3$
Z <sub>8</sub> 5	1	-1	$i$	$-i$	$\zeta^3$	$\zeta$	$\zeta^7$	$\zeta^5$
Z <sub>8</sub> 6	1	1	-1	-1	$i$	$-i$	$i$	$-i$
Z <sub>8</sub> 7	1	-1	$-i$	$i$	$\zeta$	$\zeta^3$	$\zeta^5$	$\zeta^7$

**Table C.5:** Character table of the group  $\mathbb{Z}_8$  which is a centralizer group of  $D_4^*$ . The 8th root of unity is denoted by  $\zeta = e^{i2\pi/8}$ .



# Appendix D.

## Biaxial nematic non-Abelian vortex anyons

The biaxial nematic phase also permits non-Abelian vortex anyon models. The representative biaxial nematic order parameter  $\Psi_{\text{BN}} = (1, 0, 0, 0, 1)^T/\sqrt{2}$ , has an order parameter manifold  $G/H = \text{U}(1) \times \text{SU}(2)/D_4^*$ , where  $D_4^*$  is the sixteen-element non-Abelian binary dihedral-4 group. The vortex types of the biaxial nematic phase have been characterised by Borgh and Ruostekoski [91]. Similar to the cyclic-tetrahedral phase, the topological charges are classified into seven equivalency classes. The vortex types are: (I) the vacuum state; (II) the integer spin vortex; (III)-(IV) the half quantum vortices; (V) a half quantum vortex with  $\pi/2$  spin rotation; (VI) a half quantum vortex with  $3\pi/2$  spin rotation and (VII) a half quantum vortex with  $\pi$  spin rotation. The corresponding charges are

$$\begin{aligned}
 & \text{(I)} \{(\eta, \mathbb{I})\} \\
 & \text{(II)} \{(\eta, -\mathbb{I})\} \\
 & \text{(III)} \{(\eta, \pm i\sigma_x), (\eta, \pm i\sigma_y)\} \\
 & \text{(IV)} \{(\eta, i\sigma_z), (\eta, -i\sigma_z)\} \\
 & \text{(V)} \{(\eta + 1/2, \tilde{\sigma}), (\eta + 1/2, -i\sigma_z\tilde{\sigma})\} \\
 & \text{(VI)} \{(\eta + 1/2, -\tilde{\sigma}), (\eta + 1/2, i\sigma_z\tilde{\sigma})\} \\
 & \text{(VII)} \{(\eta + 1/2, \pm i\sigma_x\tilde{\sigma}), (\eta + 1/2, \pm i\sigma_y\tilde{\sigma})\},
 \end{aligned} \tag{D.1}$$

$$\tag{D.2}$$

where  $\tilde{\sigma} \equiv (\mathbb{I} + i\sigma_z)/\sqrt{2}$ . It is noted that the vortices of equivalency classes I-IV are the same as those in equivalency classes I-III of the cyclic-tetrahedral phase. The 24

$I_0$		$I_0$
$-II_0$		$-II_0$
$III_0^x$		$-III_0^x$
$III_0^y$		$-III_0^y$
$IV_0^z$		$-IV_0^z$
$V_0$		$-V_{-1}^z$
$-V_0^z$		$V_{-1}$
$-VI_0$		$VI_{-1}^z$
$VI_0^z$		$-VI_{-1}$
$VII_0^x$		$-VII_{-1}^x$
$-VII_0^x$		$VII_{-1}^x$
$VII_0^y$		$-VII_{-1}^y$
$-VII_0^y$		$VII_{-1}^y$

**Figure D.1:** Order parameter transformations of the lowest energy biaxial nematics phase vortices. For each vortex, the biaxial nematic phase order parameter is discretely sampled at multiple points along a path enclosing the vortex core and represented using the spherical harmonic decomposition. Order parameter traverses left (right) to right (left) for labels on the left (right). The background colour of the vortex labels denotes the equivalency classes.

lowest energy vortices, as fixed by the  $U(1)$  winding number, are represented in Fig. D.1 using the spherical harmonic decomposition of the order parameter to display their characteristic rotations. In Table D.1, we provide explicit order parameters for classes V-VII, while the order parameters for classes I-III were previously presented in Table 2.1 for the cyclic-tetrahedral superfluid phase.

**Table D.1:** Explicit order parameters for a representative set of biaxial nematic phase vortices. For each vortex, labelled  $\pm X_\eta^\nu$ , we provide the corresponding rotation  $R(\theta; \pm X_\eta^\nu)$ , in terms of an angle  $\theta$ , which acts on  $\Psi_{\text{BN}}$  to generate the order parameter  $\Psi(\mathbf{r}; \pm X_\eta^\nu)$ .

$\pm X_\eta^\nu$	$R(\theta; \pm X_\eta^\nu)$	$\Psi(\mathbf{r}; \pm X_\eta^\nu)$
$V_0$	$e^{i\frac{\theta}{2}} e^{-i\frac{\theta}{4} f_z}$	$(\frac{1}{\sqrt{2}}, 0, 0, 0, \frac{1}{\sqrt{2}} e^{i\theta})^\top$
$-VI_0$	$e^{i\frac{\theta}{2}} e^{-i\frac{3\theta}{4} f_z}$	$(\frac{1}{\sqrt{2}} e^{2i\theta}, 0, 0, 0, \frac{1}{\sqrt{2}} e^{-i\theta})^\top$
$VII_0^x$	$e^{i\frac{\theta}{2}} e^{-i\frac{\theta}{2} \frac{f_x + f_y}{\sqrt{2}}}$	$\frac{e^{i\frac{\theta}{2}}}{\sqrt{2}} (\cos(\frac{\theta}{2}), e^{-i\frac{\pi}{4}} \sin(\frac{\theta}{2}), 0, e^{-i\frac{\pi}{4}} \sin(\frac{\theta}{2}), \cos(\frac{\theta}{2}))^\top$

Similar to the cyclic-tetrahedral phase, the biaxial nematic phase supports 6 non-trivial fluxons and one vacuum state corresponding to the 7 equivalency classes of  $D_4^*$ , labelled as  $I_\eta - VII_\eta$ . The  $H$ -charges correspond to irreducible representations of the centralizer groups of  $D_4^*$ . The centralizers are  $D_4^*$  (I, II),  $\mathbb{Z}_4$  (III, VII), and  $\mathbb{Z}_8$  (IV - VI) with 7, 4, and 8 irreducible representations, respectively. In total, for a given  $\eta$ , the biaxial nematic phase anyon system has one vacuum state and 45 non-trivial particles comprising 6 fluxons, 6 chargeons, and 33 dyons. The fusion rules of the 16 lowest energy fluxons are determined from the group multiplication table in Fig. D.2 and are presented in Table D.2. The biaxial nematic phase supports two concise non-Abelian anyon models. These models consist of the restricted sets of particles  $\{I_0, II_0, IV_0\}$  and  $\{I_0, II_0, III_0, IV_0\}$ , respectively. In both models, the anyons  $I_0$  and  $II_0$  are Abelian with quantum dimensions  $d_{I_0} = d_{II_0} = 1$ , while  $III_0$  and  $IV_0$  are non-Abelian anyons with quantum dimensions  $d_{III_0} = 4$  and  $d_{IV_0} = 2$ , respectively. We shall refer to these anyons as  $\mathbf{1}$ ,  $\sigma$ ,  $\tau$  and  $\xi$ , for  $I_0$ - $IV_0$ , respectively. As with the full fusion rules of the cyclic-tetrahedral anyon models, such as Eq. (5.5), incorporating the  $H$ -charges will result in a greater number of distinguishable anyons in the model. The charge inclusive fusion rules for these models are:

$$\mathbf{1}_{D0}^{(1)} \otimes \mathbf{1}_{D0}^{(1)} = \mathbf{1}_{D0}^{(1)}, \quad \mathbf{1}_{D0}^{(1)} \otimes \sigma_{D0}^{(1)} = \sigma_{D0}^{(1)}, \quad \mathbf{1}_{D0}^{(1)} \otimes \tau_{Z40}^{(1)} = \tau_{Z40}^{(1)}, \quad \mathbf{1}_{D0}^{(1)} \otimes \xi_{Z80}^{(1)} = \xi_{Z80}^{(1)} \quad (\text{D.3})$$

$$\sigma_{D0}^{(1)} \otimes \sigma_{D0}^{(1)} = \mathbf{1}_{D0}^{(1)}, \quad \sigma_{D0}^{(1)} \otimes \tau_{Z40}^{(1)} = \tau_{Z40}^{(1)}, \quad \sigma_{D0}^{(1)} \otimes \xi_{Z80}^{(1)} = \xi_{Z80}^{(1)}, \quad (\text{D.4})$$

$$\begin{aligned} \xi_{Z80}^{(1)} \otimes \xi_{Z80}^{(1)} = & \mathbf{1}_{D0}^{(1)} \oplus \mathbf{1}_{D1}^{(1)} \oplus \\ & \sigma_{D0}^{(1)} \oplus \sigma_{D1}^{(1)}, \end{aligned} \quad (\text{D.5})$$

$$\tau_{Z_{40}}^{(1)} \otimes \xi_{Z_{80}}^{(1)} = \tau_{Z_{40}}^{(1)} \oplus \tau_{Z_{42}}^{(1)}, \quad (\text{D.6})$$

and

$$\begin{aligned} \tau_{Z_{40}}^{(1)} \otimes \tau_{Z_{40}}^{(1)} &= \mathbf{1}_{D_0}^{(1)} \oplus \mathbf{1}_{D_3}^{(1)} \oplus \mathbf{1}_{D_4}^{(2)} \\ &\quad \sigma_{D_0}^{(1)} \oplus \sigma_{D_3}^{(1)} \oplus \sigma_{D_4}^{(2)} \\ &\quad \xi_{Z_{80}}^{(1)} \oplus \xi_{Z_{81}}^{(1)} \oplus \xi_{Z_{83}}^{(1)} \oplus \xi_{Z_{86}}^{(1)}, \end{aligned} \quad (\text{D.7})$$

where  $Z_{4i}$ ,  $Z_{8i}$  and  $D_i$  refer to the irreducible representations of the centralizers  $\mathbb{Z}_4$ ,  $\mathbb{Z}_8$  and  $D_4^*$ . The particles  $\mathbf{1}_{D_0}^{(1)}$ ,  $\sigma_{D_0}^{(1)}$ ,  $\tau_{Z_{40}}^{(1)}$  and  $\xi_{Z_{80}}^{(1)}$  refer to the fluxons  $I_0$ ,  $II_0$ ,  $III_0$  and  $IV_0$ , respectively. The Cheshire charge states corresponding to the  $D_i$  chargeons in Eq. (D.5) and (D.7) may be expressed in terms of a superposition of  $\xi$  or  $\tau$  flux eigenstates, respectively, as

$$\begin{aligned} |D_0, \mathbf{1}\rangle &= \frac{1}{\sqrt{2}} [\xi_z \xi_{\bar{z}} + \xi_{\bar{z}} \xi_z] \\ &= \frac{1}{2} [\tau_x \tau_{\bar{x}} + \tau_{\bar{x}} \tau_x + \tau_y \tau_{\bar{y}} + \tau_{\bar{y}} \tau_y], \\ |D_1, \mathbf{1}\rangle &= \frac{1}{\sqrt{2}} [\xi_z \xi_{\bar{z}} - \xi_{\bar{z}} \xi_z], \\ |D_3, \mathbf{1}\rangle &= \frac{1}{2} [\tau_x \tau_{\bar{x}} + \tau_{\bar{x}} \tau_x - \tau_y \tau_{\bar{y}} - \tau_{\bar{y}} \tau_y], \\ |D_4, \mathbf{1}\rangle &= \frac{1}{\sqrt{2}} \{(\tau_x \tau_{\bar{x}} - \tau_{\bar{x}} \tau_x), (\tau_y \tau_{\bar{y}} - \tau_{\bar{y}} \tau_y)\}. \end{aligned} \quad (\text{D.8})$$

Equation (D.8) can similarly represent the  $\sigma$  dyons after replacing the  $\xi$  and  $\tau$  vortex fluxes with their counterparts fusing to  $II_0$ . The Cheshire charges of the  $\tau$  dyons in Eq. (D.4) are

$$\begin{aligned} |Z_{40}, \tau\rangle_x &= \frac{1}{\sqrt{2}} [\xi_z \tau_y + \xi_{\bar{z}} \tau_{\bar{y}}], \\ |Z_{42}, \tau\rangle_x &= \frac{1}{\sqrt{2}} [\xi_z \tau_y - \xi_{\bar{z}} \tau_{\bar{y}}], \end{aligned} \quad (\text{D.9})$$

while the Cheshire charges of the  $\xi$  dyons in Eq. (D.7) are

$$\begin{aligned}
|Z_{80}, \xi\rangle_z &= \frac{1}{2}[\tau_x\tau_{\bar{y}} + \tau_y\tau_x + \tau_{\bar{x}}\tau_y + \tau_{\bar{y}}\tau_{\bar{x}}], \\
|Z_{81}, \xi\rangle_z &= \frac{1}{2}[\tau_x\tau_{\bar{y}} - \tau_y\tau_x + \tau_{\bar{x}}\tau_y - \tau_{\bar{y}}\tau_{\bar{x}}] \\
|Z_{83}, \xi\rangle_z &= \frac{1}{\sqrt{2}}\{\tau_x\tau_{\bar{y}} + \tau_{\bar{x}}\tau_y\}, \frac{1}{\sqrt{2}}\{\tau_y\tau_x + \tau_{\bar{y}}\tau_{\bar{x}}\}, \\
|Z_{86}, \xi\rangle_z &= \frac{1}{\sqrt{2}}\{\tau_x\tau_{\bar{y}} + \tau_{\bar{x}}\tau_y\}, \frac{1}{\sqrt{2}}\{-\tau_y\tau_x - \tau_{\bar{y}}\tau_{\bar{x}}\}.
\end{aligned} \tag{D.10}$$

The full set of fusion rules can be calculated using the tensor product decomposition of the representations of the quantum double  $D(H)$  of  $H$ .

**Table D.2:** Fusion rules  $a \otimes b$  for the non-Abelian vortex anyons in the biaxial nematic phase. The concise anyon models discussed in the text are highlighted.

	$I_0$	$II_0$	$III_0$	$IV_0$	$V_0$	$VI_0$	$VII_0$
$I_0$	$I_0$	$II_0$	$III_0$	$IV_0$	$V_0$	$VI_0$	$VII_0$
$II_0$	$II_0$	$I_0$	$III_0$	$IV_0$	$VI_0$	$V_0$	$VII_0$
$III_0$	$III_0$	$III_0$	$4I_0 \oplus 4II_0 \oplus 4IV_0$	$2III_0$	$2VII_0$	$2VII_0$	$4V_0 \oplus 4VI_0$
$IV_0$	$IV_0$	$IV_0$	$2III_0$	$2I_0 \oplus 2II_0$	$V_0 \oplus VI_0$	$V_0 \oplus VI_0$	$2VII_0$
$V_0$	$V_0$	$VI_0$	$2VII_0$	$V_0 \oplus VI_0$	$2I_1 \oplus IV_1$	$2II_1 \oplus IV_1$	$2III_1$
$VI_0$	$VI_0$	$V_0$	$2VII_0$	$V_0 \oplus VI_0$	$2II_1 \oplus IV_1$	$2I_1 \oplus IV_1$	$2III_1$
$VII_0$	$VII_0$	$VII_0$	$4IV_0 \oplus 4V_0$	$2VII_0$	$2III_1$	$2III_1$	$4I_1 \oplus 4II_1 \oplus 4IV_1$

A·B	$I_0$	$-II_0$	$III_0^x$	$III_0^y$	$-III_0^x$	$-III_0^y$	$IV_0^z$	$-IV_0^z$	$V_0$	$-V_0^z$	$-VI_0$	$VI_0^z$	$VII_0^x$	$-VII_0^x$	$VII_0^y$	$-VII_0^y$
$I_0$	$I_0$	$-II_0$	$III_0^x$	$III_0^y$	$-III_0^x$	$-III_0^y$	$IV_0^z$	$-IV_0^z$	$V_0$	$-V_0^z$	$-VI_0$	$VI_0^z$	$VII_0^x$	$-VII_0^x$	$VII_0^y$	$-VII_0^y$
$-II_0$	$-II_0$	$I_0$	$-III_0^x$	$-III_0^y$	$III_0^x$	$III_0^y$	$-IV_0^z$	$IV_0^z$	$-VI_0$	$VI_0^z$	$V_0$	$-V_0^z$	$-VII_0^x$	$VII_0^x$	$-VII_0^y$	$VII_0^y$
$III_0^x$	$III_0^x$	$-III_0^x$	$-II_0$	$IV_0^z$	$I_0$	$-IV_0^z$	$-III_0^y$	$III_0^y$	$-VII_0^y$	$VII_0^x$	$VII_0^y$	$-VII_0^x$	$VI_0^z$	$-V_0^z$	$V_0$	$-VI_0$
$III_0^y$	$III_0^y$	$-III_0^y$	$-IV_0^z$	$-II_0$	$IV_0^z$	$I_0$	$III_0^x$	$-III_0^x$	$VII_0^x$	$VII_0^y$	$-VII_0^x$	$-VII_0^y$	$-VI_0$	$V_0$	$VI_0^z$	$-V_0^z$
$-III_0^x$	$-III_0^x$	$III_0^x$	$I_0$	$-IV_0^z$	$-II_0$	$IV_0^z$	$III_0^y$	$-III_0^y$	$VII_0^y$	$-VII_0^x$	$-VII_0^y$	$VII_0^x$	$-V_0^z$	$VI_0^z$	$-VI_0$	$V_0$
$-III_0^y$	$-III_0^y$	$III_0^y$	$IV_0^z$	$I_0$	$-IV_0^z$	$-II_0$	$-III_0^x$	$III_0^x$	$-VII_0^x$	$-VII_0^y$	$VII_0^x$	$VII_0^y$	$V_0$	$-VI_0$	$-V_0^z$	$VI_0^z$
$IV_0^z$	$IV_0^z$	$-IV_0^z$	$III_0^y$	$-III_0^x$	$-III_0^y$	$III_0^x$	$-II_0$	$I_0$	$VI_0^z$	$V_0$	$-V_0^z$	$-VI_0$	$VII_0^y$	$-VII_0^y$	$-VII_0^x$	$VII_0^x$
$-IV_0^z$	$-IV_0^z$	$IV_0^z$	$-III_0^y$	$III_0^x$	$III_0^y$	$-III_0^x$	$I_0$	$-II_0$	$-V_0^z$	$-VI_0$	$VI_0^z$	$V_0$	$-VII_0^y$	$VII_0^y$	$VII_0^x$	$-VII_0^x$
$V_0$	$V_0$	$-VI_0$	$VII_0^x$	$VII_0^y$	$-VII_0^x$	$-VII_0^y$	$VI_0^z$	$-V_0^z$	$IV_1^z$	$I_1$	$-IV_1^z$	$-II_1$	$III_1^y$	$-III_1^y$	$-III_1^x$	$III_1^x$
$-V_0^z$	$-V_0^z$	$VI_0^z$	$-VII_0^y$	$VII_0^x$	$VII_0^y$	$-VII_0^x$	$V_0$	$-VI_0$	$I_1$	$-IV_1^z$	$-II_1$	$IV_1^z$	$III_1^x$	$-III_1^x$	$III_1^y$	$-III_1^y$
$-VI_0$	$-VI_0$	$V_0$	$-VII_0^x$	$-VII_0^y$	$VII_0^x$	$VII_0^y$	$-V_0^z$	$VI_0^z$	$-IV_1^z$	$-II_1$	$IV_1^z$	$I_1$	$-III_1^y$	$III_1^y$	$III_1^x$	$-III_1^x$
$VI_0^z$	$VI_0^z$	$-V_0^z$	$VII_0^y$	$-VII_0^x$	$-VII_0^y$	$VII_0^x$	$-VI_0$	$V_0$	$-II_1$	$IV_1^z$	$I_1$	$-IV_1^z$	$-III_1^x$	$III_1^x$	$-III_1^y$	$III_1^y$
$VII_0^x$	$VII_0^x$	$-VII_0^x$	$-VI_0$	$VI_0^z$	$V_0$	$-V_0^z$	$-VII_0^y$	$VII_0^y$	$III_1^x$	$III_1^y$	$-III_1^x$	$-III_1^y$	$-II_1$	$I_1$	$IV_1^z$	$-IV_1^z$
$-VII_0^x$	$-VII_0^x$	$VII_0^x$	$V_0$	$-V_0^z$	$-VI_0$	$VI_0^z$	$VII_0^y$	$-VII_0^y$	$-III_1^x$	$-III_1^y$	$III_1^x$	$III_1^y$	$I_1$	$-II_1$	$-IV_1^z$	$IV_1^z$
$VII_0^y$	$VII_0^y$	$-VII_0^y$	$-V_0^z$	$-VI_0$	$VI_0^z$	$V_0$	$VII_0^x$	$-VII_0^x$	$III_1^y$	$-III_1^y$	$-III_1^x$	$III_1^x$	$-IV_1^z$	$IV_1^z$	$-II_1$	$I_1$
$-VII_0^y$	$-VII_0^y$	$VII_0^y$	$VI_0^z$	$V_0$	$-V_0^z$	$-VI_0$	$-VII_0^x$	$VII_0^x$	$-III_1^y$	$III_1^y$	$III_1^x$	$-III_1^x$	$IV_1^z$	$-IV_1^z$	$I_1$	$-II_1$

**Figure D.2:** Fusion table for the topological charges of the biaxial nematic phase non-Abelian vortex anyons. The product A·B is ordered with A corresponding to the top row and B to the first column. The thick cell borders divide the regions of each anyon fusion rule. The background colour of each cell signifies the anyon type with the intensity of the shading highlighting the winding number  $\eta$ .

# Appendix E.

## Fusion rules of the tau vortex anyon model

The fusion rules of form  $\mathbf{1}_{T_i} \otimes \mathbf{1}_{T_j}^{(1)}$ ,  $\mathbf{1}_{T_i} \otimes \sigma_{T_j}$ ,  $\sigma_{T_i} \otimes \sigma_{T_j}$  can be determined trivially from the tensor products of the irreducible representations of  $T^*$  using the approach described in App. C. The  $\mathbf{1}_{T_i} \otimes \tau_{Z_j}$  fusion rules are

$$\begin{aligned}
 \mathbf{1}_{T_0}^{(1)} \otimes \tau_{Z_i}^{(1)} &= \mathbf{1}_{T_1}^{(1)} \otimes \tau_{Z_i}^{(1)} = \mathbf{1}_{T_2}^{(1)} \otimes \tau_{Z_i}^{(1)} = \tau_{Z_i}^{(1)}, \\
 \mathbf{1}_{T_3}^{(3)} \otimes \tau_{Z_i}^{(1)} &= \tau_{Z_i}^{(1)} \oplus 2\tau_{Z(2i+1)}^{(1)} \pmod{4} \\
 \mathbf{1}_{T_4}^{(2)} \otimes \tau_{Z_i}^{(1)} &= \mathbf{1}_{T_5}^{(2)} \otimes \tau_{Z_i}^{(1)} = \mathbf{1}_{T_6}^{(2)} \otimes \tau_{Z_i}^{(1)} = \tau_{Z(i-i)}^{(1)} \pmod{4} \oplus \tau_{Z(i+i)}^{(1)} \pmod{4}, \quad (\text{E.1})
 \end{aligned}$$

where the  $\sigma_{T_0} \otimes \tau_{Z_i}$  rules are defined equivalently by replacing  $\mathbf{1}_{T_i}$  with  $\sigma_{T_i}$ . Finally, the  $\tau_{Z_i} \otimes \tau_{Z_j}$  fusion rules are

$$\begin{aligned}
 \tau_{Z_0}^{(1)} \otimes \tau_{Z_0}^{(1)} &= \tau_{Z_2}^{(1)} \otimes \tau_{Z_2}^{(1)} = \mathbf{1}_{T_0}^{(1)} \oplus \mathbf{1}_{T_1}^{(1)} \oplus \mathbf{1}_{T_2}^{(1)} \oplus \mathbf{1}_{T_3}^{(3)} \oplus \\
 &\quad \sigma_{T_0}^{(1)} \oplus \sigma_{T_1}^{(1)} \oplus \sigma_{T_2}^{(1)} \oplus \sigma_{T_3}^{(3)} \oplus \\
 &\quad 2\tau_{Z_0}^{(1)} \oplus 2\tau_{Z_2}^{(1)}, \\
 \tau_{Z_1}^{(1)} \otimes \tau_{Z_1}^{(1)} &= \tau_{Z_3}^{(1)} \otimes \tau_{Z_3}^{(1)} = \mathbf{1}_{T_0}^{(1)} \oplus \mathbf{1}_{T_1}^{(1)} \oplus \mathbf{1}_{T_2}^{(1)} \oplus \mathbf{1}_{T_3}^{(3)} \oplus \\
 &\quad 2\sigma_{T_3}^{(3)} \oplus \\
 &\quad 2\tau_{Z_0}^{(1)} \oplus 2\tau_{Z_2}^{(1)},
 \end{aligned}$$

$$\begin{aligned}
\tau_{Z(\text{even})}^{(1)} \otimes \tau_{Z(\text{odd})}^{(1)} &= \mathbf{1}_{T4}^{(2)} \oplus \mathbf{1}_{T5}^{(2)} \oplus \mathbf{1}_{T6}^{(2)} \oplus \\
&\quad \sigma_{T4}^{(2)} \oplus \sigma_{T5}^{(2)} \oplus \sigma_{T6}^{(2)} \oplus \\
&\quad 2\tau_{Z1}^{(1)} \oplus 2\tau_{Z3}^{(1)}, \\
\tau_{Z0}^{(1)} \otimes \tau_{Z2}^{(1)} &= 2\mathbf{1}_{T3}^{(3)} \oplus \\
&\quad 2\sigma_{T3}^{(3)} \oplus \\
&\quad 2\tau_{Z0}^{(1)} \oplus 2\tau_{Z2}^{(1)}, \\
\tau_{Z1}^{(1)} \otimes \tau_{Z3}^{(1)} &= 2\mathbf{1}_{T3}^{(3)} \oplus \\
&\quad \sigma_{T0}^{(1)} \oplus \sigma_{T1}^{(1)} \oplus \sigma_{T2}^{(1)} \oplus \sigma_{T3}^{(3)} \oplus \\
&\quad 2\tau_{Z1}^{(1)} \oplus 2\tau_{Z3}^{(1)}.
\end{aligned} \tag{E.2}$$

# Bibliography

- [1] V. L. Berezinskii, JETP **32**, 493 (1971).
- [2] V. L. Berezinskii, JETP **34**, 601 (1972).
- [3] J. M. Kosterlitz and D. J. Thouless, J. Phys. C **5**, L124 (1972).
- [4] J. M. Kosterlitz and D. J. Thouless, J. Phys. C **6**, 1181 (1973).
- [5] J. M. Kosterlitz, Rev. Mod. Phys. **89**, 040501 (2017).
- [6] F. D. M. Haldane, Rev. Mod. Phys. **89**, 040502 (2017).
- [7] D. J. Thouless, M. Kohmoto, M. P. Nightingale, and M. den Nijs, Phys. Rev. Lett. **49**, 405 (1982).
- [8] X.-L. Qi and S.-C. Zhang, Rev. Mod. Phys. **83**, 1057 (2011).
- [9] M. A. Nielsen and I. L. Chuang, *Quantum Computation and Quantum Information: 10th Anniversary Edition* (Cambridge University Press, 2010).
- [10] A. Ekert and R. Jozsa, Rev. Mod. Phys. **68**, 733 (1996).
- [11] I. Kassal, J. D. Whitfield, A. Perdomo-Ortiz, M.-H. Yung, and A. Aspuru-Guzik, Ann. Rev. Phys. Chem. **62**, 185 (2011).
- [12] S. K. Nechaev, *Statistics of Knots and Entangled Random Walks* (World Scientific, 1996).
- [13] P. W. Shor, *Algorithms for quantum computation: discrete logarithms and factoring* (Proceedings 35th Annual Symposium on Foundations of Computer Science, 1994).
- [14] L. DiCarlo *et al.*, Nature **460**, 240 (2009).
- [15] D. Aharonov, V. Jones, and Z. Landau, Algorithmica **55**, 395 (2009).
- [16] L. H. Kauffman, *Knots and Physics*, 3rd ed. (World Scientific, 2001).

- 
- [17] R. Raz and T. Avishay, *ECCC* **107** (2018).
- [18] J. I. Cirac and P. Zoller, *Phys. Rev. Lett.* **74**, 4091 (1995).
- [19] C. Ospelkaus *et al.*, *Nature* **476**, 181 (2011).
- [20] D. Nigg *et al.*, *Science* **345**, 302 (2014).
- [21] F. A. Zwanenburg *et al.*, *Rev. Mod. Phys.* **85**, 961 (2013).
- [22] J. Clarke and F. K. Wilhelm, *Nature* **453**, 1031 (2008).
- [23] H. M. Wiseman and G. J. Milburn, *Quantum Measurement and Control* (Cambridge University Press, 2009).
- [24] W. H. Zurek, arXiv e-prints , quant (2003), quant-ph/0306072.
- [25] C. Nayak, S. H. Simon, A. Stern, M. Freedman, and S. Das Sarma, *Rev. Mod. Phys.* **80**, 1083 (2008).
- [26] J. M. Leinaas and J. Myrheim, *Nuovo Cimento B* **37B**, 1 (1977).
- [27] F. Wilczek, *Phys. Rev. Lett.* **48**, 1144 (1982).
- [28] M. H. Freedman, *PNAS* **95**, 98 (1998).
- [29] A. Y. Kitaev, *Ann. Phys.* **303**, 2 (2003).
- [30] A. Kitaev, *Ann. Phys.* **321**, 2 (2006).
- [31] S. Trebst, M. Troyer, Z. Wang, and A. W. W. Ludwig, *Prog. Theor. Phys. Supp.* **176**, 384 (2008).
- [32] S. Das Sarma, M. Freedman, and C. Nayak, *npj Quantum Inf.* **1**, 15001 (2015).
- [33] B. Field and T. Simula, *Quantum Sci. Technol.* **3**, 045004 (2018).
- [34] V. Mourik *et al.*, *Science* **336**, 1003 (2012).
- [35] S. Nadj-Perge *et al.*, *Science* **346**, 602 (2014).
- [36] Q. L. He *et al.*, *Science* **357**, 294 (2017).
- [37] H. Zhang *et al.*, *Nature* **556**, 74 (2018).
- [38] P. Zhang *et al.*, *Science* (2018).
- [39] I. P. Radu *et al.*, *Science* **320**, 899 (2008).

- 
- [40] M. Dolev, M. Heiblum, V. Umansky, A. Stern, and D. Mahalu, *Nature* **452**, 829 (2008).
- [41] R. L. Willett, L. N. Pfeiffer, and K. W. West, *PNAS* **106**, 8853 (2009).
- [42] N. D. Mermin, *Rev. Mod. Phys.* **51**, 591 (1979).
- [43] F. A. Bais, *Nucl. Phys. B* **170**, 32 (1980).
- [44] L. Brekke, H. Dykstra, A. F. Falk, and T. D. Imbo, *Phys. Lett. B* **304**, 127 (1993).
- [45] H.-K. Lo and J. Preskill, *Phys. Rev. D* **48**, 4821 (1993).
- [46] I. Chuang, R. Durrer, N. Turok, and B. Yurke, *Science* **251**, 1336 (1991).
- [47] M. J. Bowick, L. Chandar, E. A. Schiff, and A. M. Srivastava, *Science* **263**, 943 (1994).
- [48] R. Doll and M. N abauer, *Phys. Rev. Lett.* **7**, 51 (1961).
- [49] G. P. Bewley, M. S. Paoletti, K. R. Sreenivasan, and D. P. Lathrop, *PNAS* **105**, 13707 (2008).
- [50] E. Fonda, D. P. Meichle, N. T. Ouellette, S. Hormoz, and D. P. Lathrop, *PNAS* **111**, 4707 (2014).
- [51] M. R. Dennis, K. O’Holleran, and M. J. Padgett, Chapter 5 singular optics: Optical vortices and polarization singularities, pp. 293 – 363, Elsevier, 2009.
- [52] M. Uchida and A. Tonomura, *Nature* **464**, 737 (2010).
- [53] M. B. Hindmarsh and T. W. B. Kibble, *Rep. Prog. Phys.* **58**, 477 (1995).
- [54] E. J. Copeland and T. W. B. Kibble, *Proc. Royal Soc. A* **466**, 623 (2010).
- [55] L. M. A. Bettencourt, P. Laguna, and R. A. Matzner, *Phys. Rev. Lett.* **78**, 2066 (1997).
- [56] N. V. Priezjev and R. A. Pelcovits, *Phys. Rev. E* **66**, 051705 (2002).
- [57] M. Zapotocky, P. M. Goldbart, and N. Goldenfeld, *Phys. Rev. E* **51**, 1216 (1995).
- [58] K. Masuda and M. Nitta, *Phys. Rev. C* **93**, 035804 (2016).
- [59] H. M. Adachi, Y. Tsutsumi, J. A. M. Huhtam aki, and K. Machida, *J. Phys. Soc. Jpn.* **78**, 113301 (2009).

- 
- [60] M. de Wild Propitius and F. A. Bais, *Particles and Fields* (Springer Verlag, New York, 1998).
- [61] M. de Wild Propitius and F. A. Bais, ArXiv High Energy Physics - Theory e-prints (1995), hep-th/9511201.
- [62] S. N. Bose, Z. phys. **26**, 178 (1924).
- [63] A. Einstein, Sitzungsber. phys.-math. **10**, 261 (1924).
- [64] M. H. Anderson, J. R. Ensher, M. R. Matthews, C. E. Wieman, and E. A. Cornell, Science **269**, 198 (1995).
- [65] K. B. Davis *et al.*, Phys. Rev. Lett. **75**, 3969 (1995).
- [66] C. C. Bradley, C. A. Sackett, and R. G. Hulet, Phys. Rev. Lett. **78**, 985 (1997).
- [67] C. Chin, R. Grimm, P. Julienne, and E. Tiesinga, Rev. Mod. Phys. **82**, 1225 (2010).
- [68] G. Gauthier *et al.*, Optica **3**, 1136 (2016).
- [69] L. Onsager, Nuovo Cimento **6**, 249 (1949).
- [70] R. Feynman, *Chapter II Application of Quantum Mechanics to Liquid Helium*, Progress in Low Temperature Physics Vol. 1 (Elsevier, New York, 1955).
- [71] T.-L. Ho, Phys. Rev. Lett. **81**, 742 (1998).
- [72] T. Ohmi and K. Machida, J. Phys. Soc. Jpn. **67**, 1822 (1998).
- [73] L. S. Leslie, A. Hansen, K. C. Wright, B. M. Deutsch, and N. P. Bigelow, Phys. Rev. Lett. **103**, 250401 (2009).
- [74] J. Y. Choi *et al.*, New J. Phys. **14**, 053013 (2012).
- [75] S. W. Seo, S. Kang, W. J. Kwon, and Y.-i. Shin, Phys. Rev. Lett. **115**, 015301 (2015).
- [76] A. E. Leanhardt, Y. Shin, D. Kielpinski, D. E. Pritchard, and W. Ketterle, Phys. Rev. Lett. **90**, 140403 (2003).
- [77] J. Y. Choi, W. J. Kwon, and Y. I. Shin, Phys. Rev. Lett. **108**, 035301 (2012).
- [78] M. W. Ray, E. Ruokokoski, S. Kandel, M. Möttönen, and D. S. Hall, Nature **505**,

- 657 (2014).
- [79] T. Ollikainen *et al.*, Phys. Rev. X **7**, 021023 (2017).
- [80] M. W. Ray, E. Ruokokoski, K. Tiurev, M. Möttönen, and D. S. Hall, Science **348**, 544 (2015).
- [81] S. Sugawa, F. Salces-Carcoba, A. R. Perry, Y. Yue, and I. B. Spielman, Science **360**, 1429 (2018).
- [82] W. Lee *et al.*, Science Advances **4** (2018).
- [83] D. S. Hall *et al.*, Nat. Phys. **12**, 478 (2016).
- [84] N. Irikura, Y. Eto, T. Hirano, and H. Saito, Phys. Rev. A **97**, 023622 (2018).
- [85] Z. F. Xu, Y. Kawaguchi, L. You, and M. Ueda, Phys. Rev. A **86**, 033628 (2012).
- [86] T. Kawakami, T. Mizushima, and K. Machida, Phys. Rev. A **84**, 011607 (2011).
- [87] G. W. Semenoff and F. Zhou, Phys. Rev. Lett. **98**, 100401 (2007).
- [88] M. Kobayashi, Y. Kawaguchi, M. Nitta, and M. Ueda, Phys. Rev. Lett. **103**, 115301 (2009).
- [89] J. A. M. Huhtamäki, T. P. Simula, M. Kobayashi, and K. Machida, Phys. Rev. A **80**, 051601 (2009).
- [90] C. V. Ciobanu, S.-K. Yip, and T.-L. Ho, Phys. Rev. A **61**, 033607 (2000).
- [91] M. O. Borgh and J. Ruostekoski, Phys. Rev. Lett. **117**, 275302 (2016).
- [92] K. W. Schwarz, Phys. Rev. B **31**, 5782 (1985).
- [93] J. Koplik and H. Levine, Phys. Rev. Lett. **71**, 1375 (1993).
- [94] P. McGraw, Phys. Rev. D **57**, 3317 (1998).
- [95] T. W. Neely, E. C. Samson, A. S. Bradley, M. J. Davis, and B. P. Anderson, Phys. Rev. Lett. **104**, 160401 (2010).
- [96] A. Lucas and P. Surówka, Phys. Rev. A **90**, 053617 (2014).
- [97] G. W. Stagg, A. J. Allen, N. G. Parker, and C. F. Barenghi, Phys. Rev. A **91**, 013612 (2015).

- 
- [98] S. Kobayashi, N. Tarantino, and M. Ueda, *Phys. Rev. A* **89**, 033603 (2014).
- [99] L. F. Richardson, *Weather prediction by numerical process* (Cambridge University Press, 1922).
- [100] M. Leadbeater, T. Winiecki, D. C. Samuels, C. F. Barenghi, and C. S. Adams, *Phys. Rev. Lett.* **86**, 1410 (2001).
- [101] A. N. Kolmogorov, *Proc. Royal Soc. A* **434**, 9 (1991).
- [102] A. N. Kolmogorov, *Proc. Royal Soc. A* **434**, 15 (1991).
- [103] R. H. Kraichnan, *Phys. Fluids* **10**, 1417 (1967).
- [104] G. Gauthier *et al.*, *Science* **364**, 1264 (2019).
- [105] S. P. Johnstone *et al.*, *Science* **364**, 1267 (2019).
- [106] M. Kobayashi and M. Ueda, arXiv e-prints , arXiv:1606.07190 (2016).
- [107] T. Mawson, T. C. Petersen, and T. Simula, *Phys. Rev. A* **96**, 033623 (2017).
- [108] T. Mawson, T. C. Petersen, J. K. Slingerland, and T. P. Simula, *Phys. Rev. Lett.* **123**, 140404 (2019).
- [109] T. Mawson, G. Ruben, and T. Simula, *Phys. Rev. A* **91**, 063630 (2015).
- [110] W. Pauli, *Zeitschrift für Physik* **31**, 765 (1925).
- [111] C. J. Pethick and H. Smith, *Bose–Einstein Condensation in Dilute Gases* (Cambridge University Press, 2008).
- [112] S. Giorgini, L. P. Pitaevskii, and S. Stringari, *Phys. Rev. A* **54**, R4633 (1996).
- [113] A. Griesmaier, J. Werner, S. Hensler, J. Stuhler, and T. Pfau, *Phys. Rev. Lett.* **94**, 160401 (2005).
- [114] K. Aikawa *et al.*, *Phys. Rev. Lett.* **108**, 210401 (2012).
- [115] Y. Takasu *et al.*, *Phys. Rev. Lett.* **91**, 040404 (2003).
- [116] T. Fukuhara, S. Sugawa, and Y. Takahashi, *Phys. Rev. A* **76**, 051604 (2007).
- [117] M. Lu, N. Q. Burdick, S. H. Youn, and B. L. Lev, *Phys. Rev. Lett.* **107**, 190401 (2011).

- 
- [118] E. A. Donley *et al.*, Nature **412**, 295 (2001).
- [119] Y. Kawaguchi and M. Ueda, Phys. Rep. **520**, 253 (2012).
- [120] D. M. Stamper-Kurn and M. Ueda, Rev. Mod. Phys. **85**, 1191 (2013).
- [121] S. Uchino, M. Kobayashi, and M. Ueda, Phys. Rev. A **81**, 063632 (2010).
- [122] H. Saito and M. Ueda, Phys. Rev. A **72**, 053628 (2005).
- [123] M. Koashi and M. Ueda, Phys. Rev. Lett. **84**, 1066 (2000).
- [124] M. Ueda and M. Koashi, Phys. Rev. A **65**, 063602 (2002).
- [125] H. Mäkelä, Y. Zhang, and K.-A. Suominen, J. Phys. A: Math. Gen. **36**, 8555 (2003).
- [126] H. Mäkelä, J. Phys. A **39**, 7423 (2006).
- [127] J. L. Song, G. W. Semenoff, and F. Zhou, Phys. Rev. Lett. **98**, 160408 (2007).
- [128] A. M. Turner, R. Barnett, E. Demler, and A. Vishwanath, Phys. Rev. Lett. **98**, 190404 (2007).
- [129] S. Uchino, M. Kobayashi, M. Nitta, and M. Ueda, Phys. Rev. Lett. **105**, 230406 (2010).
- [130] A. L. Fetter, Rev. Mod. Phys. **81**, 647 (2009).
- [131] A. L. Fetter and A. A. Svidzinsky, J. Phys. Condens. Matt. **13**, R135 (2001).
- [132] A. S. Bradley and B. P. Anderson, Phys. Rev. X **2**, 041001 (2012).
- [133] U. Leonhardt and G. E. Volovik, JETP Letters **72**, 46 (2000).
- [134] A. Schwarz, Nucl. Phys. B **208**, 141 (1982).
- [135] S. W. Seo, W. J. Kwon, S. Kang, and Y. Shin, Phys. Rev. Lett. **116**, 185301 (2016).
- [136] F. Zhou, Phys. Rev. Lett. **87**, 080401 (2001).
- [137] J. Ruostekoski and J. R. Anglin, Phys. Rev. Lett. **91**, 190402 (2003).
- [138] J. Lovegrove, M. O. Borgh, and J. Ruostekoski, Phys. Rev. A **86**, 013613 (2012).
- [139] S. Kobayashi, Y. Kawaguchi, M. Nitta, and M. Ueda, Phys. Rev. A **86**, 023612

- (2012).
- [140] M. Ueda, Rep. Prog. Phys. **77**, 122401 (2014).
- [141] T. Isoshima, K. Machida, and T. Ohmi, J. Phys. Soc. Jpn **70**, 1604 (2001).
- [142] L. E. Sadler, J. M. Higbie, S. R. Leslie, M. Vengalattore, and D. M. Stamper-Kurn, Nature **443**, 312 (2006).
- [143] G. 't Hooft, Nucl. Phys. **B79**, 276 (1974).
- [144] A. M. Polyakov, JETP Lett. **20**, 194 (1974).
- [145] H. T. C. Stoof, E. Vliegen, and U. Al Khawaja, Phys. Rev. Lett. **87**, 120407 (2001).
- [146] C. M. Savage and J. Ruostekoski, Phys. Rev. A **68**, 043604 (2003).
- [147] P. A. M. Dirac, Proc. Royal Soc. Lond. Series A **133**, 60 (1931).
- [148] T. Mizushima, K. Machida, and T. Kita, Phys. Rev. Lett. **89**, 030401 (2002).
- [149] J.-P. Martikainen, A. Collin, and K.-A. Suominen, Phys. Rev. A **66**, 053604 (2002).
- [150] J. W. Reijnders, F. J. M. van Lankvelt, K. Schoutens, and N. Read, Phys. Rev. A **69**, 023612 (2004).
- [151] E. J. Mueller, Phys. Rev. A **69**, 033606 (2004).
- [152] N. D. Mermin and T.-L. Ho, Phys. Rev. Lett. **36**, 594 (1976).
- [153] P. W. Anderson and G. Toulouse, Phys. Rev. Lett. **38**, 508 (1977).
- [154] J. Lovegrove, M. O. Borgh, and J. Ruostekoski, Phys. Rev. A **93**, 033633 (2016).
- [155] K. Tiurev *et al.*, New J. Phys. **20**, 055011 (2018).
- [156] Y. Kawaguchi and M. Ueda, Phys. Rev. A **84**, 053616 (2011).
- [157] R. Barnett, A. Turner, and E. Demler, Phys. Rev. A **76**, 013605 (2007).
- [158] B. Lian, T.-L. Ho, and H. Zhai, Phys. Rev. A **85**, 051606 (2012).
- [159] S.-K. Yip, Phys. Rev. A **75**, 023625 (2007).
- [160] H. Mäkelä and K.-A. Suominen, Phys. Rev. Lett. **99**, 190408 (2007).
- [161] M. Fizia and K. Sacha, J. Phys. A: Math. Theor. **45**, 045103 (2012).

- [162] A. J. Groszek, D. M. Paganin, K. Helmerson, and T. P. Simula, Phys. Rev. A **97**, 023617 (2018).
- [163] W. Thomson, Philos. Mag. **10**, 155 (1880).
- [164] T. P. Simula, T. Mizushima, and K. Machida, Phys. Rev. Lett. **101**, 020402 (2008).
- [165] S. Serafini *et al.*, Phys. Rev. Lett. **115**, 170402 (2015).
- [166] S. Serafini *et al.*, Phys. Rev. X **7**, 021031 (2017).
- [167] P. Laguna and R. A. Matzner, Phys. Rev. Lett. **62**, 1948 (1989).
- [168] S. J. Rooney, P. B. Blakie, B. P. Anderson, and A. S. Bradley, Phys. Rev. A **84**, 023637 (2011).
- [169] N. D. Mermin, J. Math. Phys. **19**, 1457 (1978).
- [170] M. V. P. Volovik, V. P., JETP **45**, 1186 (1977).
- [171] J. K. Pachos, *Computational power of anyons* (Cambridge University Press, 2012), pp. 55–76.
- [172] G. K. Brennen and J. K. Pachos, Proc. Royal Soc. A **464**, 1 (2008).
- [173] J. Preskill, Lecture notes for physics 219: Quantum computation, <http://www.theory.caltech.edu/~preskill/ph219/topological.pdf>, 2004, Accessed: 2018-04-19.
- [174] J. Preskill, arXiv e-prints , arXiv:1203.5813 (2012).
- [175] S. Boixo *et al.*, Nature Physics **14**, 595 (2018).
- [176] C. Neill *et al.*, Science **360**, 195 (2018).
- [177] E. Pednault *et al.*, ArXiv e-prints , arXiv:1710.05867 (2017).
- [178] H. Bernien *et al.*, Nature **551**, 579 (2017).
- [179] J. Zhang *et al.*, Nature **551**, 601 (2017).
- [180] P. W. Shor, Phys. Rev. A **52**, R2493 (1995).
- [181] A. Steane, Proc. Royal Soc. A **452**, 2551 (1996).
- [182] M. H. Freedman, A. Kitaev, M. J. Larsen, and Z. Wang, Bull. Amer. Math. Soc.

- 40, 31 (2003).
- [183] N. E. Bonesteel, L. Hormozi, G. Zikos, and S. H. Simon, Phys. Rev. Lett. **95**, 140503 (2005).
- [184] L. Hormozi, G. Zikos, N. E. Bonesteel, and S. H. Simon, Phys. Rev. B **75**, 165310 (2007).
- [185] L. H. Kauffman and S. J. Lomonaco, New J. Phys. **6**, 134 (2004).
- [186] M. H. Freedman, A. Kitaev, and Z. Wang, Commun. Math. Phys. **227**, 587 (2002).
- [187] M. H. Freedman, M. Larsen, and Z. Wang, Commun. Math. Phys. **227**, 605 (2002).
- [188] N. E. Bonesteel, L. Hormozi, G. Zikos, and S. H. Simon, Int. J. Mod. Phys. B **21**, 1372 (2007).
- [189] H. Xu and X. Wan, Phys. Rev. A **78**, 042325 (2008).
- [190] N. N. Klausen, J. L. Bohn, and C. H. Greene, Phys. Rev. A **64**, 053602 (2001).
- [191] H. Schmaljohann *et al.*, Phys. Rev. Lett. **92**, 040402 (2004).
- [192] A. Widera *et al.*, New J. Phys. **8**, 152 (2006).
- [193] C. V. Ciobanu, S.-K. Yip, and T. L. Ho, Phys. Rev. A **61**, 033607 (2000).
- [194] H. M. Hurst and I. B. Spielman, Phys. Rev. A **99**, 053612 (2019).
- [195] A. L. Gaunt, T. F. Schmidutz, I. Gotlibovych, R. P. Smith, and Z. Hadzibabic, Phys. Rev. Lett. **110**, 200406 (2013).
- [196] J. A. M. Huhtamäki, T. P. Simula, M. Kobayashi, and K. Machida, Phys. Rev. A **80**, 051601 (2009).
- [197] J. R. Abo-Shaer, C. Raman, V. J. M., and W. Ketterle, Science **292**, 476 (2001).
- [198] A. A. Penckwitt, R. J. Ballagh, and C. W. Gardiner, Phys. Rev. Lett. **89**, 260402 (2002).
- [199] T. P. Simula, S. M. M. Virtanen, and M. M. Salomaa, Phys. Rev. A **66**, 035601 (2002).
- [200] K. Kasamatsu, M. Tsubota, and M. Ueda, Phys. Rev. A **67**, 033610 (2003).
- [201] A. E. Leanhardt *et al.*, Phys. Rev. Lett. **89**, 190403 (2002).

- 
- [202] M. R. Matthews *et al.*, Phys. Rev. Lett. **83**, 2498 (1999).
- [203] C. F. Barenghi and N. G. Parker, *A Primer on Quantum Fluids* (Springer International Publishing, 2016).
- [204] G. R. Dennis, J. J. Hope, and M. T. Johnsson, Comp. Phys. Comm. **184**, 201 (2013).
- [205] M. L. Chiofalo, S. Succi, and M. P. Tosi, Phys. Rev. E **62**, 7438 (2000).
- [206] A. J. Groszek, T. P. Simula, D. M. Paganin, and K. Helmerson, Phys. Rev. A **93**, 043614 (2016).
- [207] C. A. Jones and P. H. Roberts, J. Phys. A: Math. Gen. **15**, 2599 (1982).
- [208] W. J. Kwon, G. Moon, J.-y. Choi, S. W. Seo, and Y.-i. Shin, Phys. Rev. A **90**, 063627 (2014).
- [209] L. A. Smirnov and A. I. Smirnov, Phys. Rev. A **92**, 013636 (2015).
- [210] S. Nazarenko and M. Onorato, J. Low Temp. Phys. **146**, 31 (2007).
- [211] J. M. Higbie *et al.*, Phys. Rev. Lett. **95**, 050401 (2005).
- [212] K. Kasamatsu, M. Eto, and M. Nitta, Phys. Rev. A **93**, 013615 (2016).
- [213] S. Gautam, ArXiv e-prints (2016), 1601.06020.
- [214] J. Schwinger, Phys. Rev. **144**, 1087 (1966).
- [215] J. Schwinger, Phys. Rev. **173**, 1536 (1968).
- [216] D. Zwanziger, Phys. Rev. **176**, 1489 (1968).
- [217] E. Witten, Phys. Lett. B **86**, 283 (1979).
- [218] L. Carroll and S. M. Wiggins, *Alice's adventures in wonderland / Lewis Carroll ; illustrated by S. Michelle Wiggins* (Collins Sydney, 1983).
- [219] M. G. Alford, K. Benson, S. Coleman, J. March-Russell, and F. Wilczek, Phys. Rev. Lett. **64**, 1632 (1990).
- [220] J. Preskill and L. M. Krauss, Nucl. Phys. B **341**, 50 (1990).
- [221] K. O. Roberts *et al.*, Opt. Lett. **39**, 2012 (2014).

- [222] E. C. Samson, K. E. Wilson, Z. L. Newman, and B. P. Anderson, Phys. Rev. A **93**, 023603 (2016).
- [223] T. P. Simula *et al.*, Phys. Rev. Lett. **94**, 080404 (2005).
- [224] The thistlethwaite link table l2a1-l11n459, [http://katlas.org/wiki/The\\_Thistlethwaite\\_Link\\_Table\\_L2a1-L11n459](http://katlas.org/wiki/The_Thistlethwaite_Link_Table_L2a1-L11n459), 2006, Accessed: 2018-10-30.
- [225] T. H. Koornwinder, B. J. Schroers, J. K. Slingerland, and F. A. Bais, J. Phys. A: Math. Gen. **32**, 8539 (1999).
- [226] J. Ruostekoski and J. R. Anglin, Phys. Rev. Lett. **86**, 3934 (2001).
- [227] M. O. Borgh and J. Ruostekoski, Phys. Rev. A **87**, 033617 (2013).
- [228] D. Naidu and E. C. Rowell, Algebras and Representation Theory **14**, 837 (2011).
- [229] S. Das Sarma, M. Freedman, and C. Nayak, Phys. Rev. Lett. **94**, 166802 (2005).
- [230] S. Bravyi, Phys. Rev. A **73**, 042313 (2006).
- [231] C. Mochon, Phys. Rev. A **67**, 022315 (2003).
- [232] C. Mochon, Phys. Rev. A **69**, 032306 (2004).
- [233] R. Rouse, S. Han, and J. E. Lukens, Phys. Rev. Lett. **75**, 1614 (1995).
- [234] J. R. Friedman, V. Patel, W. Chen, S. K. Tolpygo, and J. E. Lukens, Nature **406**, 43 (2000).
- [235] C. H. van der Wal *et al.*, Science **290**, 773 (2000).
- [236] J. I. Cirac, M. Lewenstein, K. Mølmer, and P. Zoller, Phys. Rev. A **57**, 1208 (1998).
- [237] D. Gordon and C. M. Savage, Phys. Rev. A **59**, 4623 (1999).
- [238] J. Ruostekoski, M. J. Collett, R. Graham, and D. F. Walls, Phys. Rev. A **57**, 511 (1998).
- [239] J. A. Dunningham, K. Burnett, R. Roth, and W. D. Phillips, New J. Phys. **8**, 182 (2006).
- [240] C. Ryu *et al.*, Phys. Rev. Lett. **99**, 260401 (2007).
- [241] A. Ramanathan *et al.*, Phys. Rev. Lett. **106**, 130401 (2011).

- 
- [242] K. Helmerson *et al.*, Nucl. Phys. A **790**, 705c (2007).
- [243] J. Dunningham and D. Hallwood, Phys. Rev. A **74**, 023601 (2006).
- [244] D. W. Hallwood, K. Burnett, and J. Dunningham, New J. Phys. **8**, 180 (2006).
- [245] T. Simula, Phys. Rev. A **97**, 023609 (2018).
- [246] S. M. M. Virtanen, T. P. Simula, and M. M. Salomaa, Phys. Rev. Lett. **87**, 230403 (2001).
- [247] N. Goldman, G. Juzeliūnas, P. Öhberg, and I. B. Spielman, Rep. Prog. Phys. **77**, 126401 (2014).
- [248] J. Dalibard, F. Gerbier, G. Juzeliūnas, and P. Öhberg, Rev. Mod. Phys. **83**, 1523 (2011).
- [249] S. Sugawa, F. Salces-Carcoba, A. R. Perry, Y. Yue, and I. B. Spielman, Science **360**, 1429 (2018).
- [250] M. Bucher, K.-M. Lee, and J. Preskill, Nucl. Phys. B **386**, 27 (1992).
- [251] T. Araki, M. Tsubota, and S. K. Nemirovskii, Phys. Rev. Lett. **89**, 145301 (2002).
- [252] E. A. L. Henn, J. A. Seman, G. Roati, K. M. F. Magalhães, and V. S. Bagnato, Phys. Rev. Lett. **103**, 045301 (2009).
- [253] P. M. Walmsley and A. I. Golov, Phys. Rev. Lett. **100**, 245301 (2008).
- [254] Maurer, J. and Tabeling, P., Europhys. Lett. **43**, 29 (1998).
- [255] S. R. Stalp, L. Skrbek, and R. J. Donnelly, Phys. Rev. Lett. **82**, 4831 (1999).
- [256] M. Kobayashi and M. Tsubota, Phys. Rev. Lett. **94**, 065302 (2005).
- [257] W. F. Vinen, Phys. Rev. B **61**, 1410 (2000).
- [258] E. Kozik and B. Svistunov, Phys. Rev. B **77**, 060502 (2008).
- [259] G. Krstulovic, Phys. Rev. E **86**, 055301 (2012).
- [260] W. F. Vinen, M. Tsubota, and A. Mitani, Phys. Rev. Lett. **91**, 135301 (2003).
- [261] T. Simula, M. J. Davis, and K. Helmerson, Phys. Rev. Lett. **113**, 165302 (2014).
- [262] A. J. Groszek, M. J. Davis, D. M. Paganin, K. Helmerson, and T. P. Simula, Phys.

- Rev. Lett. **120**, 034504 (2018).
- [263] T. P. Billam, M. T. Reeves, B. P. Anderson, and A. S. Bradley, Phys. Rev. Lett. **112**, 145301 (2014).
- [264] T. P. Billam, M. T. Reeves, and A. S. Bradley, Phys. Rev. A **91**, 023615 (2015).
- [265] R. Numasato, M. Tsubota, and V. S. L'vov, Phys. Rev. A **81**, 063630 (2010).
- [266] M. T. Reeves, T. P. Billam, B. P. Anderson, and A. S. Bradley, Phys. Rev. Lett. **110**, 104501 (2013).
- [267] T. W. Neely *et al.*, Phys. Rev. Lett. **111**, 235301 (2013).
- [268] S. Kang, S. W. Seo, J. H. Kim, and Y. Shin, Phys. Rev. A **95**, 053638 (2017).
- [269] J. H. Kim, S. W. Seo, and Y. Shin, Phys. Rev. Lett. **119**, 185302 (2017).
- [270] K. Fujimoto and M. Tsubota, Phys. Rev. A **85**, 033642 (2012).
- [271] K. Fujimoto and M. Tsubota, Phys. Rev. A **88**, 063628 (2013).
- [272] K. Fujimoto and M. Tsubota, Phys. Rev. A **90**, 013629 (2014).
- [273] M. Tsubota, Y. Aoki, and K. Fujimoto, Phys. Rev. A **88**, 061601 (2013).
- [274] W. J. Kwon, G. Moon, S. W. Seo, and Y. Shin, Phys. Rev. A **91**, 053615 (2015).
- [275] C. N. Weiler *et al.*, Nature **455**, 948 (2008).
- [276] S. Burger *et al.*, Phys. Rev. Lett. **83**, 5198 (1999).
- [277] J. Denschlag *et al.*, Science **287**, 97 (2000).
- [278] Z. Dutton, M. Budde, C. Slowe, and L. V. Hau, Science **293**, 663 (2001).
- [279] A. Cetoli, J. Brand, R. G. Scott, F. Dalfovo, and L. P. Pitaevskii, Phys. Rev. A **88**, 043639 (2013).
- [280] K. W. Nicholls and J. F. Nye, J. Phys. A: Math. Gen. **20**, 4673 (1987).
- [281] G. Ruben and D. M. Paganin, Phys. Rev. E **75**, 066613 (2007).
- [282] G. Ruben, D. M. Paganin, and M. J. Morgan, Phys. Rev. A **78**, 013631 (2008).
- [283] G. Ruben, M. J. Morgan, and D. M. Paganin, Phys. Rev. Lett. **105**, 220402 (2010).
- [284] T. P. Simula, J. A. M. Huhtamäki, M. Takahashi, T. Mizushima, and K. Machida,

- J. Phys. Soc. Jpn. **80**, 013001 (2011).
- [285] D. R. Scherer, C. N. Weiler, T. W. Neely, and B. P. Anderson, Phys. Rev. Lett. **98**, 110402 (2007).
- [286] R. Carretero-González, B. P. Anderson, P. G. Kevrekidis, D. J. Frantzeskakis, and C. N. Weiler, Phys. Rev. A **77**, 033625 (2008).
- [287] K. Henderson, C. Ryu, C. MacCormick, and M. G. Boshier, New J. Phys. **11**, 043030 (2009).
- [288] T. C. Petersen *et al.*, Phys. Rev. Lett. **110**, 033901 (2013).
- [289] T. P. Simula, T. C. Petersen, and D. M. Paganin, Phys. Rev. A **88**, 043626 (2013).
- [290] B. H. Bransden and C. C. J. Joachain, *Quantum Mechanics*, Second ed. (Prentice Hall PTR, 2000).
- [291] M. Koshino, New J. Phys. **15**, 015010 (2013).
- [292] J. Javanainen and S. M. Yoo, Phys. Rev. Lett. **76**, 161 (1996).
- [293] M. F. Andersen *et al.*, Phys. Rev. Lett. **97**, 170406 (2006).
- [294] S. W. Seo, B. Ko, J. H. Kim, and Y. Shin, Sci. Rep. **7**, 4587 (2017).
- [295] A. T. Powis, S. J. Sammut, and T. P. Simula, Phys. Rev. Lett. **113**, 165303 (2014).
- [296] N. G. Berloff and P. H. Roberts, J. Phys. A: Math. Gen. **34**, 10057 (2001).
- [297] T. P. Simula, Phys. Rev. A **84**, 021603 (2011).
- [298] L. A. Williamson and P. B. Blakie, Phys. Rev. Lett. **116**, 025301 (2016).
- [299] B. Nowak, D. Sexty, and T. Gasenzer, Phys. Rev. B **84**, 020506 (2011).
- [300] H. Georgi, *Lie Algebras In Particle Physics: from Isospin To Unified Theories* (Avalon Publishing, 1999).
- [301] T. Dokchitser, Finite group  $sl(2,3)$ , [https://people.maths.bris.ac.uk/~matyd/GroupNames/1/SL\(2,3\).html](https://people.maths.bris.ac.uk/~matyd/GroupNames/1/SL(2,3).html), Accessed: 2018-12-03.
- [302] J. Montaldi, Representations dicyclic, <http://www.maths.manchester.ac.uk/~jm/wiki/Representations/Dicyclic>, 2008, Accessed: 2018-12-03.